# Nanoscale Tip-enhanced Raman Scattering (TERS) for Biomolecular Analyses

Dissertation zur Erlangung des akademischen Grades des Doktors der Naturwissenschaften (Dr. rer. nat.)

eingereicht in der Fakultät für Chemie der Technischen Universität Dortmund

vorgelegt von

Dipl.-Chem. Elena Bailo
aus Barcelona

Februar 2009

# Danksagung

Ich möchte mich an dieser Stelle ganz herzlich bei allen bedanken, die mich bei meiner Doktorarbeit mit ihrem Wissen und ihrer Erfahrung unterstützt haben.

Ein ganz besonderer Dank gilt meinem Chef und Betreuer, PD Dr. Volker Deckert, für die Chance an dieser Nano-Welt teilzunehmen, für seine tägliche Motivation, Geduld, wertvollen Ratschläge für den Erfolg der Doktorarbeit und für die Durchsicht des Manuskripts und die aufmunternden Kommentare, danke!

Bei Herrn Prof. Dr. Rehage möchte ich mich für die Übernahme der Zweitbegutachtung und für seine Hilfe bei allen bürokratischen Vorgängen im Zusammenhang mit dieser Arbeit bedanken.

Bei Carmen, Christian, Katherine, Kosta, Melissa, Regina und Tanja möchte ich mich ganz herzlich dafür bedanken, dass sie meine Doktorarbeit mit großem Interesse gelesen und korrigiert haben.

Ein „großer“ Dank geht an Dr. Christian Budich, der mich während meiner gesamten Zeit als Doktorandin mit großer fachlicher Kompetenz beraten und unterstützt hat. Ich danke ihm für seine Geduld, mit der er mir das AFM und biologische Themen verständlich gemacht hat.

Bei Herrn Gosciniak, Herrn Herzog, Frau Pulvermacher, Marc Richter, Tanja Deckert-Gaudig und Kosta Nalpantidis möchte ich mich für die Vorbereitung der Spitzen, REM-aufnahmen, Intrumental- und Methodenberatung und immer interessanten Unterhaltungen während der Kaffee- und nicht Kaffeepausen bedanken.

I would like to express my thanks to my “Australian boss”, Dr. Bayden Wood, for letting me take part in his project and process the PCA data, but especially for his great humor while working together in the Lab. And also my thanks to Medhi Ashghari Khiavi for the band assignments at chapter 5.

I would like to thank Dr. Ljiljana Fruk for teaching me many things about enzyme catalysis and SERS, and working together on her project.

Mein Dank an Carmen García, Ola Polatajko, Alex Pajak, Marta Garijo, Sven Tombrink, Ali Zein Al-Din und Magnus Eickmeyer für ihre Freundschaft und immer gute Laune während dieser drei Jahre bei der Arbeit und/oder nach der Arbeit.

Auch an alle Doktoranden und Kollegen am ISAS, die Zusammenarbeit hat immer sehr viel Spaß gemacht. Auch ihnen ein großes Dankeschön.

Der wichtigste Dank aber gilt meinen Eltern, Freunden und Verwandten in Spanien, die mir mit viel Verständnis und Geduld die ganze Zeit zur Seite gestanden und mich unterstützt haben.

# Zusammenfassung und Ausblick

In der vorliegenden Doktorarbeit wurde die spitzenverstärkte Raman-Spektroskopie (englisch: tip-enhanced Raman scattering, TERS) und ihr Vorgänger, die oberflächenverstärkte Raman Spektroskopie (englisch: surface-enhanced Raman scattering, SERS), zu Studien geringster Mengen von Biomolekülen mit schnellen Messzeiten verwendet.

Vielen Einschränkungen von SERS und anderen spektroskopischen Methoden konnten dabei durch TERS aufgehoben werden. So wurde beispielsweise bei der Detektion von Biomolekülen eine räumliche Auflösung im Nanometerbereich erzielt, bei gleichzeitig höchster Nachweisstärke.

**SERS an katalytischen Prozessen**

Zur Untersuchung der Wechselwirkungen von Fettsäuren mit dem Enzym $P450_{BSß}$ wurden SERS-Messungen auf Silberkolloiden durchgeführt. Die charakteristischen Banden für $P450_{BSß}$ wurden identifiziert, sowie signifikante Änderungen in den SERS-Spektren in Gegenwart von Myristinsäure bestimmt. Die spektralen Verschiebungen konnten entsprechend auf die strukturellen Änderungen in der Häm-Umgebung zurückgeführt werden. Die Ergebnisse zeigen deutlich das Potenzial von SERS zur spektroskopischen Bestimmung neuer Häm-Enzymsubstrat Wechselwirkungen auf.

**TERS in Malaria infizierten menschlichen Zellen**

Im Rahmen dieser Arbeit konnten zum erstem Mal rasterkraftmikroskopische (englisch: atomic force microscopy, AFM) Aufnahmen zusammen mit ersten TERS-Spektren von Makromolekülen an einzelnen Malaria infizierten roten Blutzellen aufgenommen werden. Die detektierten Raman Signale wurden kristallinem Hämozoin zugeordnet und belegen eindeutig, dass die gleiche Strucktur wie beim sythetisch herstellten ß-Hämatin vorgeliegt.. Unter Verwendung der Modelsubstanz Hämoglobin konnte die selektive Verstärkung von Häm- und Proteinmoden demonstriert werden. Darüber hinaus wurden die spektralen Fluktuationen, die aufgrund der Empfindlichkeit der TERS-Methode im Nanometerbereich auftreten, mittels Hauptkomponentenanalyse (englisch: Principal Component Analysis, PCA) bestätigt. Diese Ergebnisse eröffnen einen völlig neuen Weg, die Bindung eines Wirkstoffs an die Hämozoinkristalloberfläche innerhalb der Verdauungsvakuole des Parasiten mittels TERS zu untersuchen.

**TERS auf einem DNA und RNA Strang**

In Rahmen dieser Doktorarbeit wurde die ersten TERS-Messungen entlang eines synthetisch hergestellten RNA Einzelstrangs des Homopolymers Cytosin erfolgreich durchgeführt. In diesem Experiment konnte eine räumliche Auflösung von weniger als 60 Nukleobasen erreicht werden. Unter Berücksichtigung des Signal-Rausch-Verhältnisses wurde Einzelbasenempfindlichkeit nachgewiesen. Die beobachteten spektralen Fluktuationen in den TERS-Messungen ließen sich auf besondere Effekte der sehr hohen lateralen Auflösung und Verstärkungsfaktoren zurückführen.

Weitere Experimente über einen Homopolymerstrang von Adenin lieferten Informationen über den Verstärkungsbereich der TERS Spitze, der demnach deutlich unter 20 nm angesetzt werden kann. Wiederholte TERS Messungen an ein und demselben Punkt bestätigten, dass die beobachteten Fluktuationen in den TERS Spektren an verschiedenen Punkten auf Nanoskala-Effekten, wie der relativen Poisition zwischen Spitze und Probe sowie Feldgradienteffecten herrühren. An dieser

Stelle soll darauf hingewiesen werden, dass sich die Effekte von denen in der Raman- und SERS Spektroskopie unterscheiden. Diese Ergebnisse zeigen deutlich das Potential von TERS bei der Identifizierung von Einzelstrang Dann auf. Es sollte daher möglich sein, eine direkte markerfreie Sequenzierung von DNA mit dieser Methode zu erzielen.

Abschließend lässt sich sagen, dass die vorgestellten Ergebnisse zeigen, dass TERS eine äußerst leistungsfähige Technik ist, mit dem Potential eine direkte and markerfreie Sequenzierung von DNA und RNA und weiterer kettenförmiger Biomoleküle wie z.B. Peptiden oder Proteinen zu erreichen. Außerdem ermöglicht die nachgewiesene räumliche Auflösung und hohe Sensitivität von TERS, die Klärung einer großen Anzahl an weiteren Fragestellungen wie z.B. die Anbindung von Wirkstoffen an Zellen oder biomolekulare Wechselwirkungen mit der Zellmembran.

Ein wichtiges Ziel ist die breitere Anwendbarkeit der Technologie. Da viele Faktoren, wie die Form, die Orientierung und die Lage des Nanopartikels auf der Spitze, die Verstärkung beeinflussen, ist eine detaillierte Untersuchung dieser Faktoren zukünftig notwendig, um empfindlichere, kleinere, und reproduzierbarere Spitzen zu erhalten.

# Contents

**Chapter 1: Introduction……1**

**Chapter 2: From Raman Spectroscopy to TERS……3**

2.1 Raman effect……5

2.2 Instrumentation……10

2.2.1 Excitation source……11

2.2.2 Sample illumination system and collection optics (optical microscope)……13

2.2.3 Wavelength selector (Filter or spectrophotometer)……14

2.2.4 Detector……16

2.3 Surface-enhanced Raman scattering (SERS)……18

2.4 Tip-enhanced Raman Scattering (TERS)……20

2.4.1 Theoretical background……21

2.4.2 Experimental aspects in TERS……32

2.5 References……40

**Chapter 3: Experimental Part……45**

3.1 TERS Setup……45

3.2 Tip preparation……47

3.3 Sample preparation……48

3.4 Challenges……48

3.5 References……50

**Chapter 4: SERS as a Tool to Probe Cytochrome P450-Catalysed Substrate Oxidation .....51**

4.1 Heme proteins & SERS .....52

4.2 SERS on Cytochrome $P450_{BS\beta}$ interactions .....54

4.3 Materials and Methods .....60

4.4 Conclusion & Outlook .....61

4.5 References .....62

**Chapter 5: TERS inside a Malaria Infected Human Red Blood Cell .....65**

5.1 Sectioned malaria infected human red blood cells .....67

5.2 TERS fingerprint of malaria infected red blood cells (RBCs) .....69

5.3 Materials and Methods .....79

5.4 Conclusions and outlook .....81

5.5 References .....83

**Chapter 6: TERS on DNA & RNA strands: Towards a Novel Direct-Sequencing Method .....87**

6.1 Structure of DNA and RNA .....88

6.2 DNA sequencing .....89

6.2.1 Chain-terminator or Sanger dideoxynucleotide method .....89

6.2.2 Pyrosequencing .....92

6.2.3 Nanopore methods .....94

6.2.4 Scanning tunneling microscopy (STM) method .....97

6.3 Tip-Enhanced Raman Spectroscopy of Single RNA Strands: Towards a Novel Direct-Sequencing Method .....98

6.4 Reproducibility and enhancement region of TERS on DNA strands .....111

6.5 Sample preparation .....118

6.6 Challenges and Outlook .....120

6.7 References .....125

**Chapter 7: Summary and Conclusions .....129**

# Chapter 1

# Introduction

In the last decades, vibrational spectroscopy techniques such as infrared and Raman spectroscopy have demonstrated to be a key tool in surface analysis of biomolecular samples. Although these techniques provide sufficient sensitivity and spatial resolution for numerous applications, the detection and analysis of biosamples at very low concentration and high spatial resolution requires more powerful techniques.

Silver and gold nanoparticles are used to overcome very low Raman cross section, creating a surface plasmon polariton (SPP) on the surface of the metal nanoparticles. When the sample is located close to metal surface, the plasmon couples to the absorbed photon enhancing the probability of Raman scattering. A common technique that uses this phenomenon is surface-enhanced Raman scattering (SERS). SERS provides large signal enhancement by a factor of $10^{10}$-$10^{12}$ necessary to detect biomolecular samples at very low concentration. The enhancement factor varies with the size, shape and roughness of the different particles at the SERS substrate; this means that variations of the intensity of the Raman signal are observed along the inhomogeneity of the SERS substrate, making the technique very challenging for quantitative analysis. Tip-enhanced Raman scattering has overcome the inhomogeneity problem taking just one of the metal nanoparticle and placed it at the end of an atomic force microscope (AFM) tip. The AFM tip moves the particle to a desired position on the sample, a TERS spectrum is then achieved and afterward a new position can be measured with the same nanoparticle just by simply moving the tip, thus providing a constant enhancement for each measurement. TERS provides not

only large constant enhancement of the Raman signal but also measurements at high lateral resolution.

The first part of this thesis (Chapter 2) reviews the fundamentals and instrumentation of Raman spectroscopy and its evolution to TERS. The principle of TERS and the variety of experimental setups employed by different groups will be described in this chapter.

Taking advantages of the large enhancement, sensitivity and nanoscale resolution provided by TERS, many open questions in biomolecular sciences could be investigated.

In Chapter 5 the first TERS experiment performed inside a malaria infected human cell is described and discussed. Using hemoglobin as a model compound, the selective enhancement of heme and protein modes is shown.

In Chapter 6 the first TERS experiment on a synthetic RNA homopolymer (cytosine) single strand at lateral resolution down to a few tens of nucleobases is presented. Additionally further TERS experiments on synthetic DNA homopolymer (adenine) were performed to estimate experimental enhancement region and reproducibility of TERS is shown.

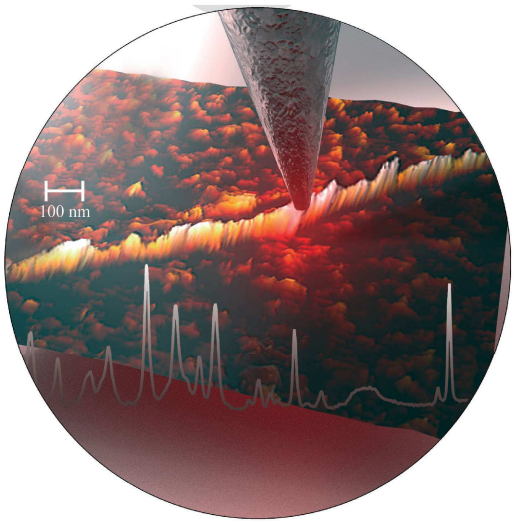


**Figure 1.1:** *Schematic of a TERS experiment on a single RNA strand.*

*(Illustration designed by J. Hinrichs)*

# Chapter 2

## From Raman spectroscopy to TERS

When light passes through a transparent medium, by nature a part of this radiation is scattered in all directions. Furthermore, in a fraction of this scattered light a shift in frequency is observable compared to the incident radiation. This phenomenon is known as the Raman effect and is specific for each chemical compound. Currently Raman scattering is widely applied to identify and analyze chemical and condensed physical materials in research and industry.

Raman spectroscopy is based on the inelastic scattering of light radiation. Inelastic scattering is characterized by a frequency shift of photons by interactig with the sample when subsequently reemitted (scattered) (Figure 2.1)

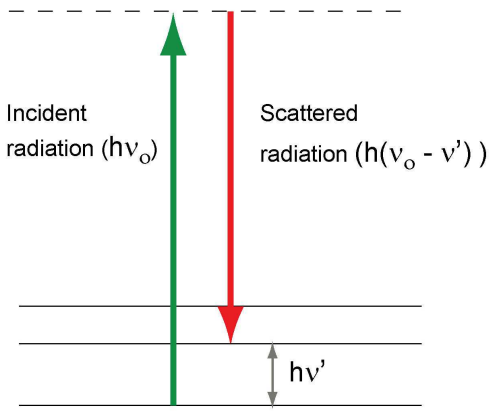


**Figure 2.1:** *Energy level diagram of the inelastic Raman process for Stokes scattering.*

The frequency of scattered photons is shifted to higher or lower frequencies in comparison to that of the incident radiation. The variations in frequency observed in this phenomenon are equivalent to variations in energy. Atoms and ions are bound to each other to form molecules and crystal systems and constantly perform vibrational and

rotational motions. These oscillations are performed at exact frequencies as a function of the involved particle mass and the dynamic behaviors of the existent bonds, the force constants (Figure 2.2). Each vibrational and rotational mode has a corresponding energy level. Another characteristic of Raman spectroscopy is its straight forward application for the study of liquid, solid and gaseous samples.

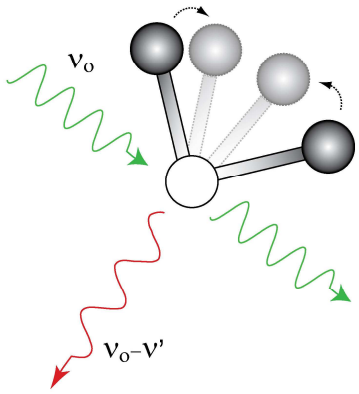


**Figure 2.2:** *Photons with frequency ($\nu_o$) interact with a molecule and induce a molecular motion, knwon as a vibrational mode on the radiated molecule and immediately a photon with a different frequency ($\nu_o \pm \nu$') is reemitted.*

## 2.1 Raman effect

In 1928, the Indian physicist C.V. Raman was the first to observe the inelastic scattering.[1] To illustrate this, sunlight was used as a radiation source to demonstrate the evidence of this phenomenom, as shown in Figure 2.3. Sunlight, the most intense light available at that time, was collected by a telescope and focused on an organic solution. To observe changes in frequency, he filtered the white light through a green filter to obtain a monochromatic green light. The green light then passed through the sample and C.V. Raman was able to observe a weak yellow scattered radiation was observed after placing a yellow filter behind the sample. This proofed existence of inelastic scattering, now well-known as the Raman effect, which C.V. Raman reported as a new secondary radiation in Nature.

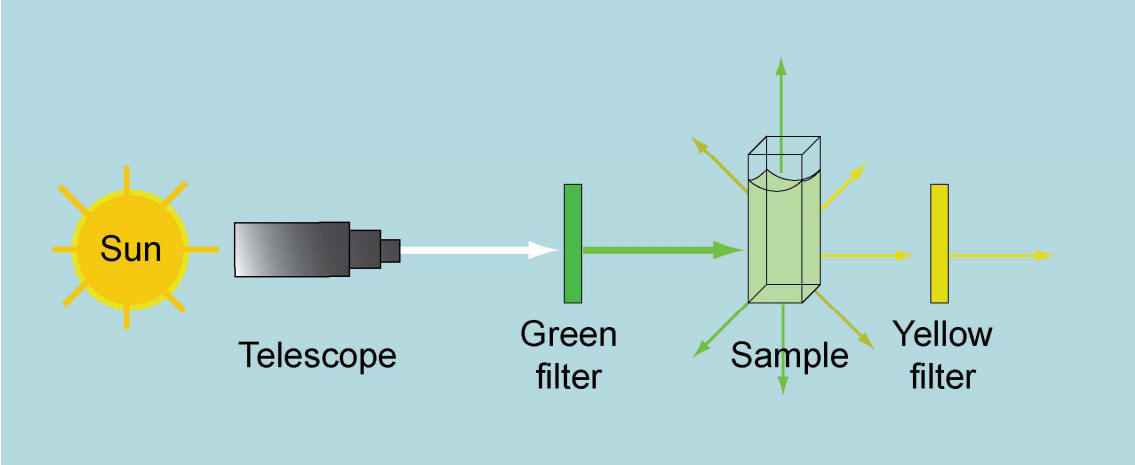


**Figure 2.3:** *Schematic diagram of the discovery of the Raman effect by C.V. Raman in 1928.*

A laser is commonly used today as a radiation source in Raman spectroscopy. It is much more intense than the sun light and operated at defined frequency (monochromaticity). A laser beam can be considered as a plane electromagnetic wave with an electric field, E, perpendicular to a magnetic component, H (see Figure 2.4).

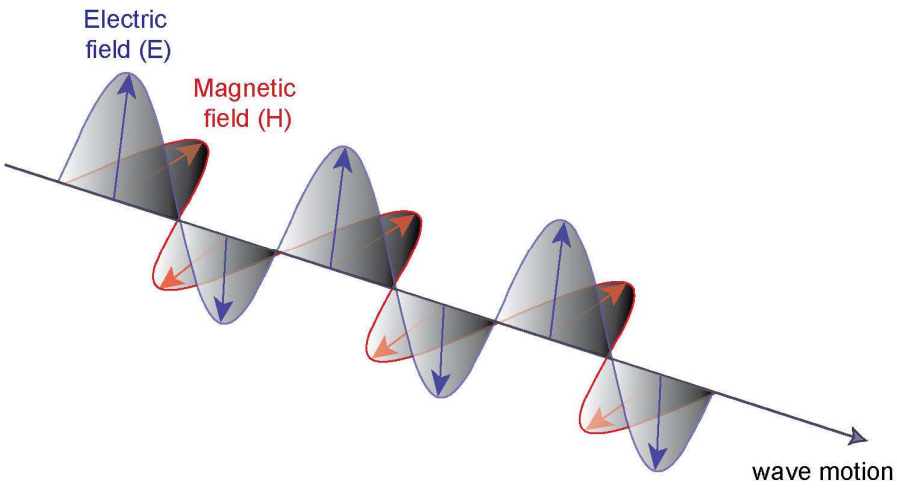


**Figure 2.4:** *Diagram of a self-propagating linear polarized electromagnetic wave.*

The interaction of the laser beam with the molecule occurs through the electron cloud of the molecule. The ability of the electronic cloud of the molecule to change in space by the interaction with an electric field is determined by its molecular polarizability, $\alpha$.

A molecule has a certain number of vibrational modes, which can be calculated in case of a linear molecule by 3N-5 and for a non-linear molecule by 3N-6, where N is the number of atoms. Not all vibrational modes of a molecule are Raman active. For a vibrational mode to be Raman active, the molecular motion induced by the electric field must involve a change in the molecular polarizability. Figure 2.5.b shows how the morecular polaribility changes from the equilibrium to the extended and compressed motions. A vibrational frequency is characteristic for each molecular deformation and the amplitude of this vibrational mode is related to the nuclear displacement. For the same vibrational mode to be IR active, must be involved a change in the dipole moment. In Figure 2.5.a is shown that for the same molecular motion, the dipole moment of the molecule does not change from the equilibrium to the extended and

compressed motions. Therefore, the symmetric vibrational mode of a $CO_2$ molecule is observed in Raman spectroscopy but not in IR spectroscopy.

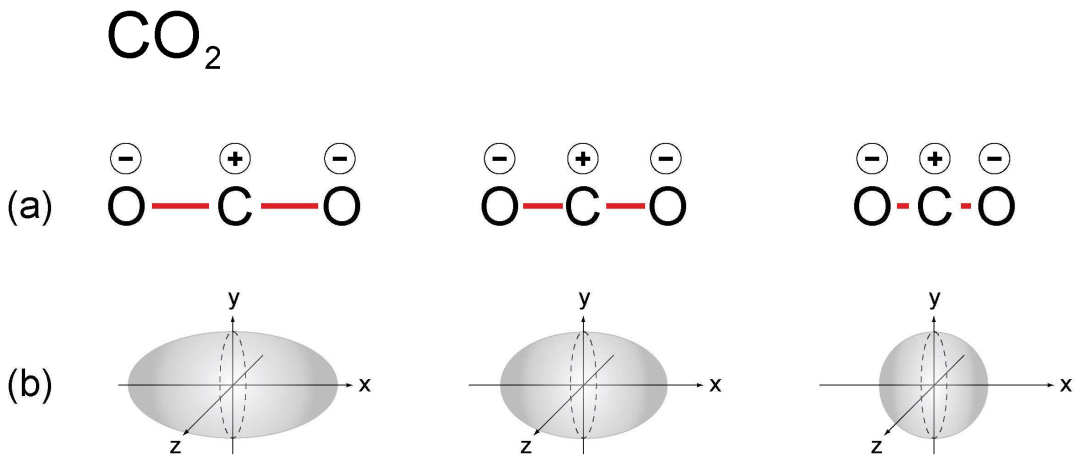


**Figure 2.5:** *The symmetric stretching of a $CO_2$ molecule (a) does not produce any changes in the dipole moment (not IR active) but does (b) in the polarizability of the molecule (Raman active).*

In conclusion, the oscillating electric field, E, of the photons of a monochromatic source with frequency, $\nu_o$, varying with the time, *t*, is represented by:

$$E = E_O \cos 2\pi\nu_O t \qquad \textbf{(2.1)}$$

where $E_o$ is the maximum amplitude.

The oscillating electric field is responsible for the excitation and conversion of molecules into an oscillating dipole, $\mu$, which varies as:

$$\mu = \alpha E = \alpha E_O \cos 2\pi\nu_O t \qquad \textbf{(2.2)}$$

where $\alpha$ is the polarizability of the molecule, which varies also with the time is represented by:

$$\alpha = \alpha_O + \alpha' \cos 2\pi\nu' t \qquad \textbf{(2.3)}$$

where $\alpha_o$ is the polarizability of the equilibrium conformation of the molecule,$\alpha'$ is the polarizability change with molecular vibration, and $\nu'$ is the vibrational frequency of the molecule.

Combining both equations *(2.2)* and *(2.3)* the dipole is resulted as:

$$\mu = [\alpha_O + \alpha' \cos 2\pi\nu' t\,] \cdot E_O \cos 2\pi\nu_O t \qquad \textbf{(2.4)}$$

Equation *(2.4)* can be developed into three terms as:

$$\mu = \alpha_O \cdot E_O \cos 2\pi\nu_O t + 0.5\alpha' \cdot E_O [\cos 2\pi (\nu_O + \nu')t + \cos 2\pi (\nu_O - \nu')t\,] \qquad \textbf{(2.5)}$$

Theses three terms represent that the oscillating dipole reemits the photons in three characteristic frequencies: the first term is Rayleigh scattering with the same frequency as the radiation source ($\nu_o$) does not provide any spectroscopic information. The second and third terms are Stokes scattering with frequency $\nu_o$-$\nu'$ and anti-Stokes scattering with frequency $\nu_o$+$\nu'$. Their energy level diagram of the three different types of radiation is illustrated in Figure 2.6. In the Raman process an electron in the ground state is excited into a virtual state for a short time, and then reemitted to the ground state which lies in higher or lower energy than the initial state. It is important to note that if the molecular vibration does not cause a change in polarizability, $\nu'$ is zero, and therefore, there is no Raman scattering.

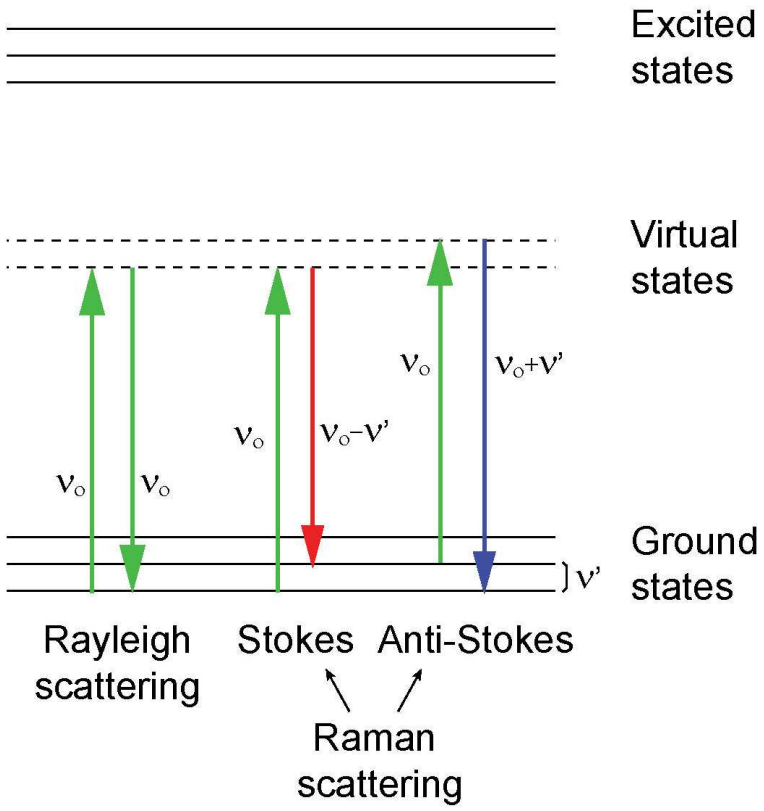


**Figure 2.6:** *Energy level diagram of the Rayleigh, Stokes and anti-Stokes scattering.*

Each vibrational or rotational mode corresponds to a relative frequency shift, which is independent of the wavelength of the laser source. The collection of the different frequencies or Raman shifts undergone by a molecule is known as Raman spectrum and provides an individual fingerprint (composition of Raman shifts) characteristic for each molecule, which allows its identification and structural analysis.

## 2.2 Instrumentation

Only one in ten million photons of incident radiation source undergo spontaneous Raman scattering with frequencies $\nu_o \pm \nu_m$. Therefore, Raman systems are designed to collect as many Raman scattered photons as possible. Additionally, since Rayleigh scattering is more prevalent than Raman scattering its radiation must be blocked. To do this Raman instruments are equipped with filters, pinholes, and/or double/triple monochromators to block the elastic scattering present which does not provide any useful vibrational information.

A Raman system typically consists of four major components (Figure 2.7):

a) Excitation source

b) Sample illumination system and collection optics

c) Wavelength selector

d) Detector

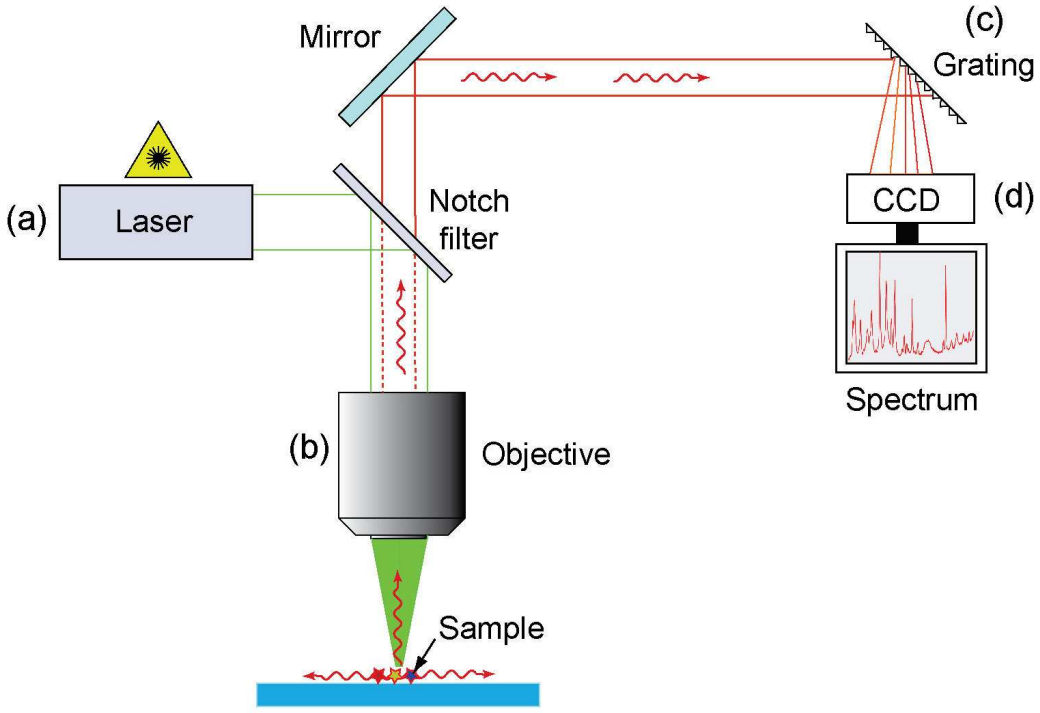


**Figure 2.7:** *Schematic diagram of a conventional Raman setup composed of (a) a Laser as excitation source, (b) objective as sample illumination and collection optics, (c) grating as wavelength selector and (d) CCD camera as detector.*

### 2.2.1 Excitation source

The word “laser” is an acronym for Light Amplification by Stimulated Emission of Radiation. The laser produces quasi-monochromatic light that focuses a very narrow band of frequencies. Laser sources are spatially coherent (waves have the same phase and direction), are highly collimated (the beam is parallel) and the light is concentrated in a very intense and small beam.

In 1917, Albert Einstein published a theoretical report with the basics of the laser process known as “Stimulated Emission”[2] and in 1960, the first operative laser

was developed by Theodore Maiman.[3] The laser was an important technological advance and facilitated a resurgence of interest in Raman spectroscopy.

Lasers are can be wavelength-tunable radiation sources and the sample is usually radiated with wavelengths spanning from ultraviolet (UV) or visible to Infrared (IR) (Figure 2.8).

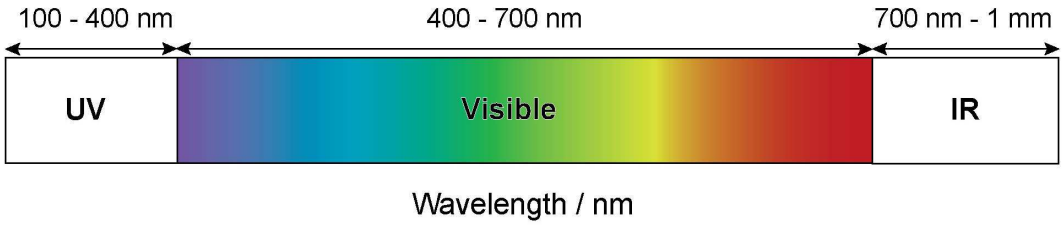


**Figure 2.8:** *Optical wavelength range from UV to IR.*

The laser process can be understood as follows. First, an inversion of population is created through at least a three-level energy system, described in Figure 2.9. The unexcited atoms of an element in the ground state, $E_1$, are excited by external forces (pumping energy) to level 3, $E_3$, and quickly decay to $E_2$. Afterward, some of the atoms relaxe to the ground state, $E_1$, as a result a photon is released (spontaneous emission, shown in Figure 2.10.a). Second, when a photon interacts with an excited atom which then decays to the ground state two final photons are produced with identical frequency, phase and direction as the original incoming photon (Figure 2.10.b). This phenomenon is called stimulated emission and is repeated through a chain reaction with the rest of excited atoms and the new two photons.

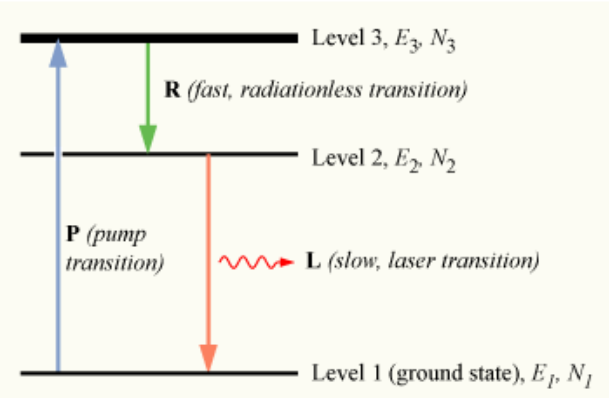


***Figure 2.9:*** *Schematic diagram of three-level system laser. From Ref.*[4]

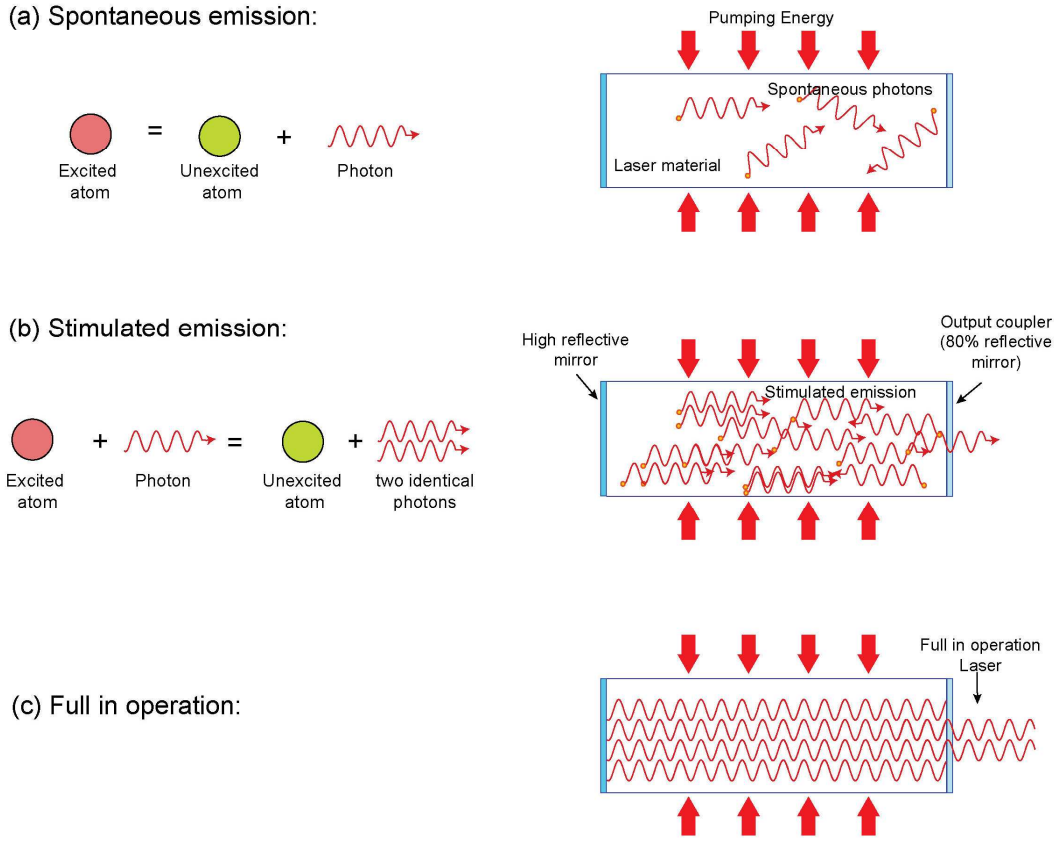


**Figure 2.10:** *Diagram of the generation of Laser radiation.*

### 2.2.2 Sample illumination system and collection optics (optical microscope)

An important advantage of Raman over IR is the use of standard optical components, much cheaper than IR equiment. Glass can be used in the optical system of the setup for windows, lenses or other optical components because it does not provide strong signal as with IR, which interferes in the spectrum.

An optical microscope is usually employed in Raman microscopy to irradiate the sample with the laser source and collect the Raman signal produced in the interaction.

Raman microscopy provides a satisfactory lateral resolution, which depends on the wavelength (λ) of the radiation source and the numerical aperture (NA) of the microscope objective.

Numerical aperture is defined by: NA=n(sinα), where n is the refraction index of the medium between the objective and the sample and α defining the aperture angle of the objective (see Figure 2.11).

For measurements where high lateral resolution is required, the use of objectives with high numerical aperture is quite common. They are usually designed to work in a medium with high refraction index such as oil, water or glycerin and in combination with the use of a source with a short wavelength, lateral resolution up to 200 nm can be reached.

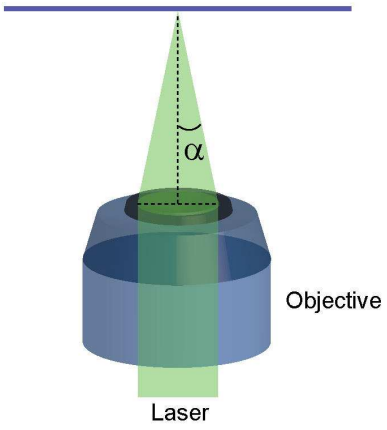


**Figure 2.11:** *The numerical aperture depends on the half-angle (α) of the laser cone.*

## 2.2.3 Wavelength selector (Filter or spectrophotometer)

The collected Raman scattering is led to the spectrometer and because Raman scattering takes place at frequencies very close to the laser frequency and shows a very weak intensity, one of the major challenges of Raman spectroscopy is to eliminate the laser line and the Rayleigh scattering radiation. This problem is easily solved by cutting off the laser spectral range with laser-blocking filters. These Raman filters are specially designed to “block off” specific wavelengths. There are two main types which can be employed: edge filters and notch filters (see Figure 2.12).

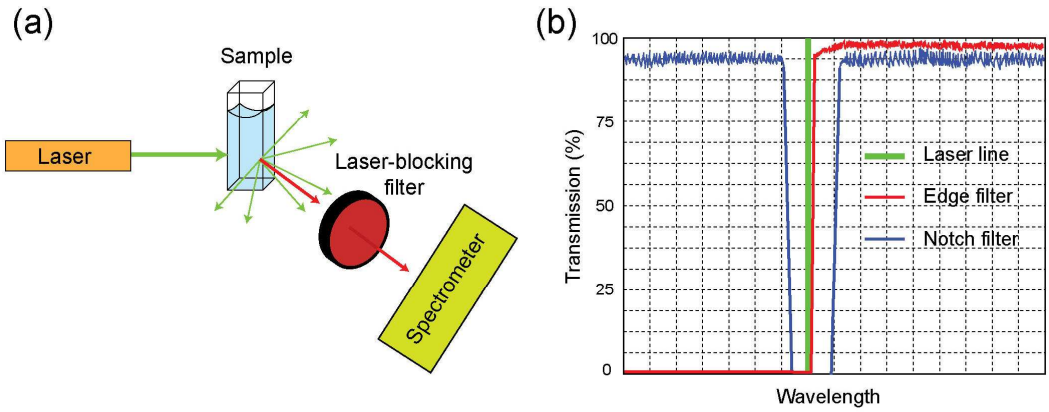


**Figure 2.12:** *Blocking laser line filters.(a) Simple schematic diagram of a Raman system, where the laser line is filtered before the spectrometer. (b) Transmittance vs. wavelength dependence for edge and notch filters in respect to a laser line.*

In the case of notch filters a narrow spectral range of approximately 200 $cm^{-1}$ is cut off and above and below this range maximum transmittance is given. For this reason, notch filters are used when both Stokes and anti-Stokes scattering should be simultaneously investigated.

Furthermore, there are two types of edge filters: longpass and shortpass. The longpass edge filters block off all wavelengths below a given wavelength and therefore it's only employed to measure Stokes-Raman scattering. Shortpass edge filters block off all wavelengths above a given wavelength and are suitable for Anti-Stokes Raman scattering studies. Recent developments, edge filters, provide several advantages compared with notch filters. Edge filters offer a higher transmittance and the cutting edge is closer to the laser frequency, permitting the detection of Raman bands at short wavenumbers extremely close to the laser line.

The Raman scattered light is then filtered by the Raman filter, and can be dispersed using a diffraction grating. This separates the light into the different wavelengths for the identification of the specific vibration modes (see Figure 2.13).

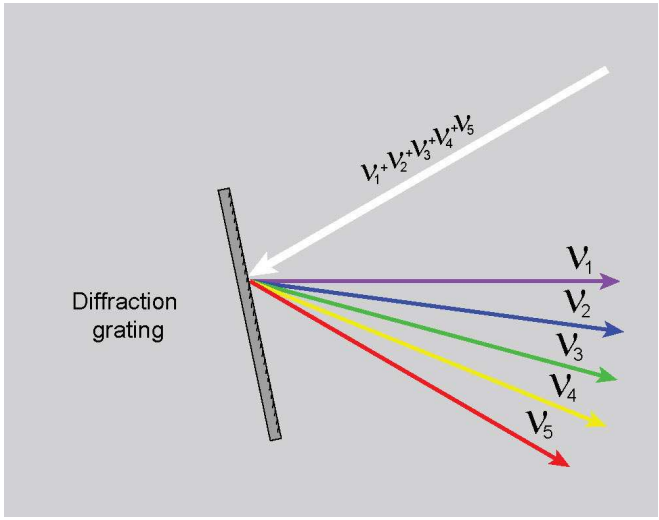


**Figure 2.13:** *Diffraction gratings separate the Raman scattered light into its different wavelengths.*

### 2.2.4 Detector

Light can be converted into electrical signals by using photoelectric devices such as photodiodes (PD), photomultipliers (PMT) or charge coupled devices (CCD).

All these three detectors are employed in Raman spectroscopy, but nowadays the most popular detectors are charge coupled devices (CCD) because they are the most sensitive and require shorter acquisition times for a complete spectrum.

A CCD array is composed of thousands of pixels, which generate electron-hole pairs when a photon enters through. The electrons are collected and for reading out shifted to a horizontal register, as shown in Figure 2.14. The photons with different wavelengths separated by the diffraction grating are collected a different horizontal position on the CCD array.

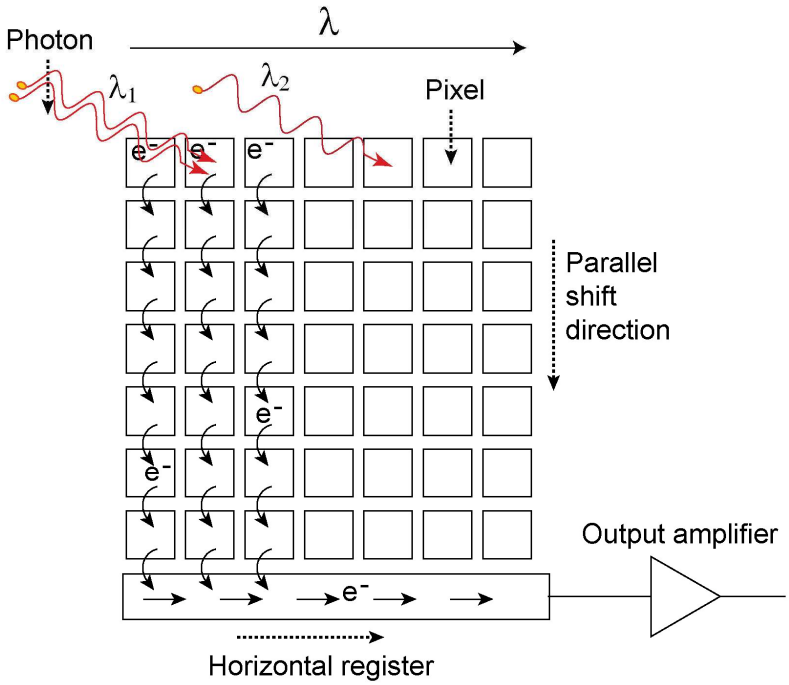


**Figure 2.14:** *Operation mode of charge coupled devices (CCD). Photons enter through the pixels generating electron-hole pairs, which are collected and led to the horizontal register for the following reading out.*

## 2.3 Surface-enhanced Raman scattering (SERS)

In 1974, Fleischmann *et al.*[5] observed unusual strong Raman signals of pyridine molecules adsorbed onto a roughened silver electrode. Firstly, this phenomenon was attributed to the increase of the number of adsorbed molecules. But in 1977, Creighton[6] and Van Duyne[7] publicised that the enhancement originated from the roughened silver surface, and they called it Surface-enhanced Raman scattering (SERS). The discovery of SERS overcame one of the major challenges of normal Raman spectroscopy, the weak signal. Typical enhancement factors of SERS are $10^{10}$-$10^{12}$, which allows the studies of samples at very low concentration.[5, 7]

The most critical aspect is the design of the SERS substrates Examples are shown in Figure 2.15. The SERS enhancement (optical properties) directly depends on the noble-metal material (Ag or Au), size, shape, and interparticle spacing of the aggregated nanoparticles. Depending on these parameters, the Plasmon resonance shifts to a specific wavelength. Excitation at this excitation wavelength provides the largest Raman signal enhancement.

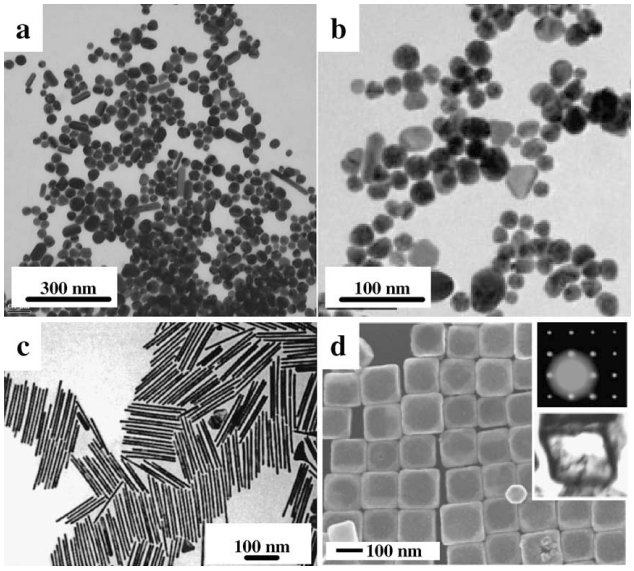


**Figure 2.15:** *Transmission electron microscopy (TEM) images of typical SERS substrates, (a) silver citrate,[8] (b) gold borohydride[9, 10] colloids, and (c) gold nanorods,[10] (d) Au nanosquares[11] and their diffraction pattern.*

Figure 2.16 shows aqueous suspensions of silver nanoparticles which vary in their resonance frequency in the visible range depending on their aspect ratio.[12]

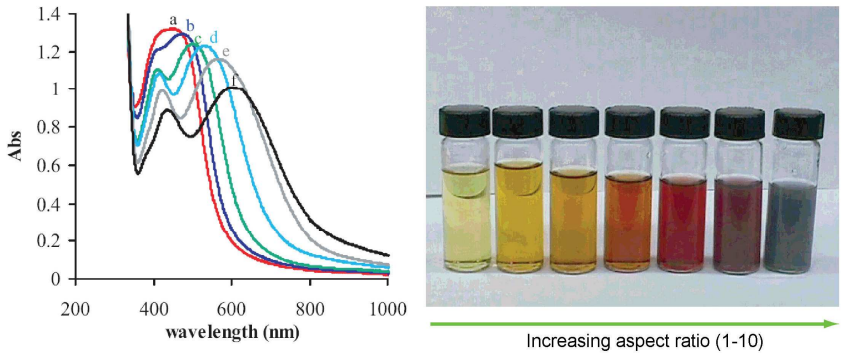


**Figure 2.16:** *(right) seven aqueous suspensions of silver nanoparticles with aspect ratio 1-10 and (left) absorption spectra of each suspensions which show the variation in the visible wavelength range of their resonance frequency depending on the aspect ratio. From Ref.*[12]

A classic procedure for the preparation SERS substrates with colloidal nanoparticles is shown in Figure 2.17. Single metal nanoparticles are initially suspended in aqueous solution. The largest enhancements are expected on rough surfaces and in interpaticle junctions. Therefore, the single nanoparticles are "activated" or aggregated by special aggregation agents, such as NaCl, $MgCl_2$ or ascorbic acid, to create junctions. After this step the sample is added to the solution.

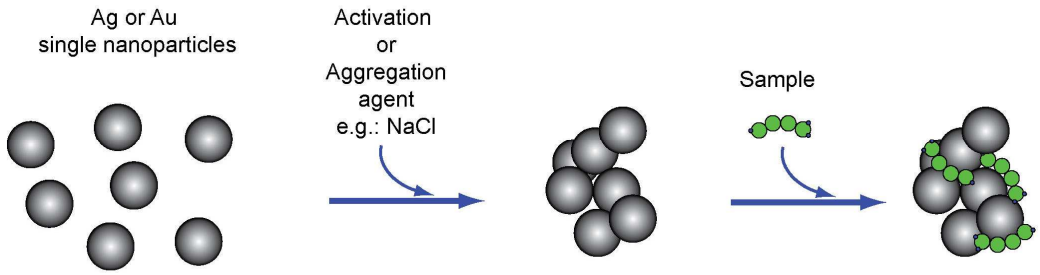


**Figure 2.17:** *Sample preparation for SERS measurements.*

The main obstacle associated with SERS is the inhomogeneity of the field enhancement across the sample. The different shapes, sizes and roughness of single

particles and clusters result in strong variations of the field enhancement and consequently the Raman signal. Furthermore, these physical parameters also depend critically on the substrate preparation. A quantitative analysis of interfaces using SERS is therefore almost impossible.

It is well known that the large field enhancement at metal particles occurs in regions of high curvature and maximum enhancement occurs for elongated particles with dimensions of about 10-100 nm. While clusters are considered to yield a better overall enhancement, also a single isolated metal nanoparticle can enhance the field considerably.[13-17]

## 2.4 Tip-enhanced Raman Scattering (TERS)[18]

In 1985 Wessel[15] theoretically proposed a scheme to ensure a constant field enhancement using just one single metal nanoparticle for the investigation of a surface.[15] For the first time, this introduced the potential of quantitative SERS surface analysis. In this design, the rough metal film was replaced by a sharp metal tip that whould act as an exclusive active site, and also represents the limit for any SERS experiment: at least one particle is required. In Figure 2.18 illustrated the idea proposed by Wessel[15] for the construction of a single-particle surface-enhanced microscope. The metal tip should be scanned over the sample surface using scanning probe microscopy (SPM) techniques. The later experimental verification of this now called Tip-enhanced Raman spectroscopy (TERS) and only 15 year later experimental verification was successfully proved.[19-21] In addition to the field enhancement the lateral resolution of this method was improved down to the nanometer level on single-walled carbon nanotubes (SWNTs) due to the small size of the probe[22] and applied on sample at very low concentration, such as on a monolayer of $CN^-$.[23]

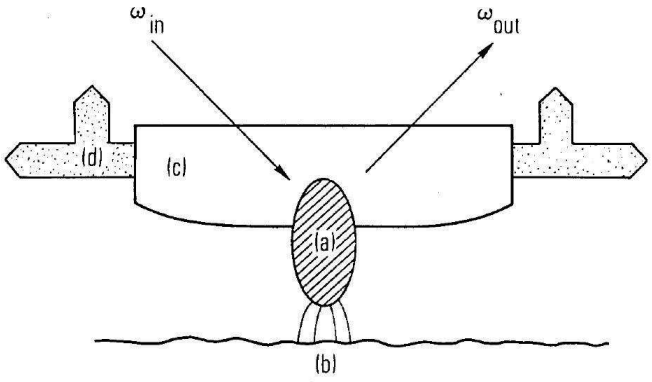


**Figure 2.18:** *Single metal nanopaticle working as optical probe particle designed by Wessel Ref.* [15]

At present this combination of SPM techniques and Raman spectroscopy is successfully applied to many questions in the nano-sciences, because of its unique possibility to obtain chemical and structural information of a sample surface with high lateral resolution and sensitivity. [18, 24, 25]

## 2.4.1 Theoretical background

### 2.4.1.1 Raman enhancement at single metal particles

The large enhancement of Raman scattering from single metal probe used in TERS can be discussed on the same basis as the SERS effect. In general two mechanisms are responsible for the Raman enhancement: the electromagnetic effect and the chemical or charge transfer effect, which applies only to the first layer of adsorbates.

On the surface of spherical and elongated metal nanoparticles, surface plasmons are excited by light. The involved electromagnetic field can be strongly enhanced in the presence of surface plasmons if certain resonance conditions are fulfilled. The product of the enhancement of the incident laser field and the scattered

Raman signal lead to the overall SERS effect.[13, 14] When the electromagnetic field of laser radiation is incident upon a metallic nanoparticle, the electric field of the radiation drives the free electrons of the metal nanoparticle into collective oscillation. As a result, the overall electromagnetic field is enhanced (Figure 2.19).

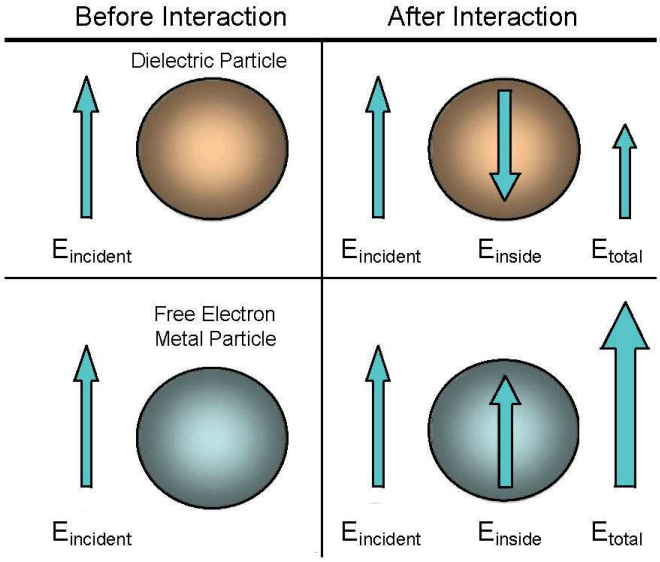


**Figure 2.19:** *Effect of electromagnetic field on metallic and dielectric nanoparticles. Adapted from Ref.[26]*

The second enhancement mechanism, the chemical effect, corresponds to an amplification of the polarizability of the molecule due to a charge transfer between the metal and the adsorbed molecule.[27, 28] Considerable band shifts are associated with this effect and can be used to distinguish whether the metal particle is in direct contact with the sample. Experimental evidence for a chemical effect exists also for TERS experiments on nucleobases and $C_{60}$ done by the groups of Kawata[29, 30] and Deckert[21], respectively. Band shifts on adenine were observed, which strongly indicate a direct involvement of a silver-nucleobase interaction, as shown in Figure 2.20.a, and consequently a chemical enhancement. In contrast, no band shifts are detected for a different TERS experiment on cytosine and thymine nanocrystals.[31] This has been

attributed to a special distribution of silver nanoparticles on the specific AFM tip used in this TERS experiment. In this case, as shown in Figure 2.20.b, the silver particle was placed slightly behind the actual apex of the probe but still close enough to the substrate to cause an electromagnetic enhancement. Consequently, no evidence for a direct interaction between tip and specimen in this particular experiment was observed and the spectra therefore resemble essentially the bulk spectra of the nucleobases and not the SERS spectra.[31]

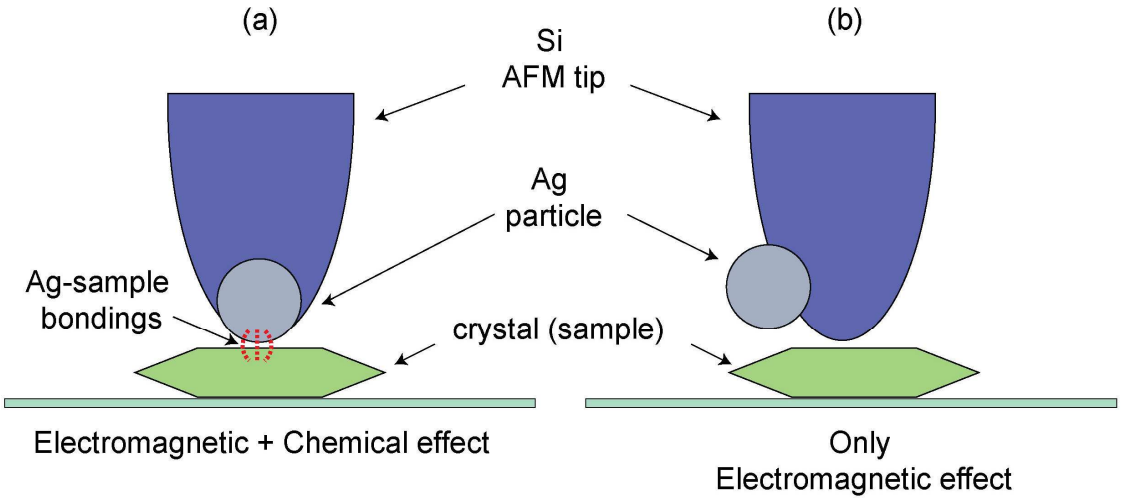


***Figure 2.20:*** *Schematic representation of two TERS experiments: (a) where the silver particle is at the apex of the AFM tip which involves both effect electromagnetic and chemical effect, due to the formation of a Ag-sample complex, and (b) where the silver particle is placed slightly behind the apex, causing only electromagnetic enhancement.*

One of the most important features of TERS is the ability to highly confine the electromagnetic field at the apex of a sharp metal tip. This is due to an electrostatic lightning rod effect as a result of the shape of the particle at the tip apex. This results in the high spatial resolution of the technique.

### 2.4.1.2 Near-field optics

The basic explanation of the high-resolution capabilities of TERS is based on near-field optics and, in particular, in evanescent waves that occur close to small objects. An evanescent wave is a standing wave that exponentially decays in space. It can be probed using a nano-antenna, which converts the standing wave into a propagating wave detectable in the far-field.

The enhancement associated with a TERS tip varies with respect to the specific position on the particle. The electric properties of the material, the size and shape of the metal tip and the illumination geometry play an important role for the enhancement factor and its distribution around the tip.

Different models have been developed to theoretically investigate the field enhancement of single particles.[22]

In order to calculate the electromagnetic fields involved when a metallic nanoparticle or tip is irradiated with light, one has to solve either Maxwell's or Helmholtz's equations. For this purpose, several numerical methods are available. They can be classified by:

- An analytical extension that describes the geometry and solve the field equations as well as the boundary condition exactly. Neither area nor time should be discretized.

- *Semi-analytical methods*, where only the field equations are solved exactly within certain domains. The adjustment of the boundary conditions takes place through approximated solutions by discretization of boundary points and minimization of the errors. The Multiple Multipole method (MMP) is one of those techniques.[32, 33]

- *Semi-numerical methods*. Here, the boundary conditions are exactly determined and field equations within a domain are solved approximately. In this way, the area is discretized. Two examples of this method are the Finite Difference Time Domain Method (FDTD)[34, 35] and the Finite Element Method (FEM)[36, 37].

- *Full numerical methods*. Here, both the boundary conditions and the solutions within the domain are numerically approximated. As a result, the area and the domain boundary are discretized. [38]

FEM, MMP and FDTD are most frequently applied to model the field distribution of single metal nanoparticles and will be discussed in more detail.

By the FDTD method,[34, 35] Maxwell's equations are discretized directly in time and space. The domain area is discretized in this case by rectangles (see Figure 2.21). The boundary conditions between the elements are exactly adjusted and each block in the interior of the domain is interpolated.

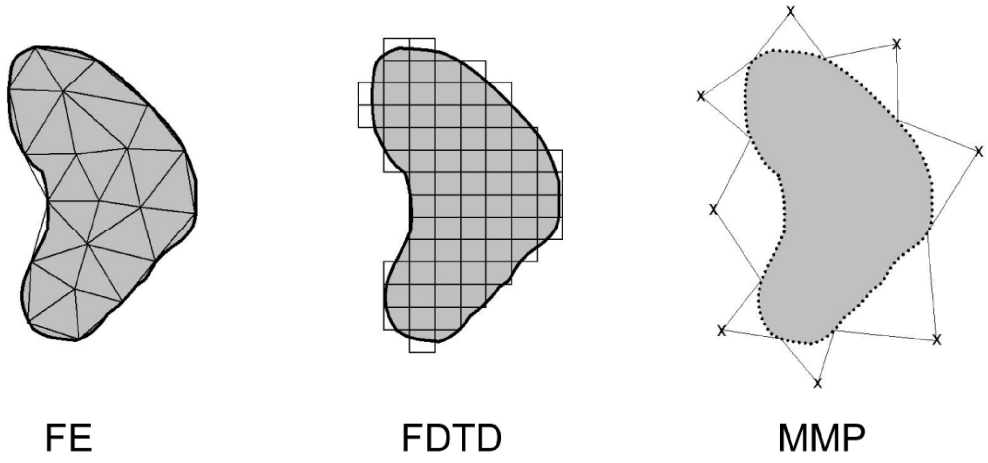


**Figure 2.21:** *Different discretization methods used in the theoretical modeling of electromagnetic fields of particles. From Ref.[38]*

The FE method[37, 39] operates in the frequency domain and unlike FDTD, Helmoltz's equations are discretized in the space domain. It uses a continuous domain which is divided into simple polygons called subdomains (see Figure 2.21).

In MMP[32, 33] the unknown E- and H-fields within individual homogeneous domains are expanded by a series of expansion in the spherical wavelength vectors, called multipoles, with known analytical solutions of Maxwell's equations. The amplitude of these fields are then solved by a Generalized Point Matching Method (GPMM). In general, the scattering problem is described as a set of linear differential equations.

As example of the MMP method applied in optical problems, in Figure 2.22 the electric field distribution of a silver ellipsoid with glass core when it is excited at its resonance frequency at 605 nm is shown.[18, 38] The studies can be extended to more complex/realistic objects, as shown in Figure 2.23. Here the influence of different core shapes on the resonance frequency of a coated silver particle shown.[38] Even small changes can cause quite large shifts in the resonance. With respect to the practical experiment this has two aspects. Tips should be carefully checked with respect to the excitation laser wavelength, as the plasmon resonances can be far from the desired spectral range. Concerning the tip production, it can provide a nice way of tuning TERS tips towards the desired resonances, if proper conditions are used.

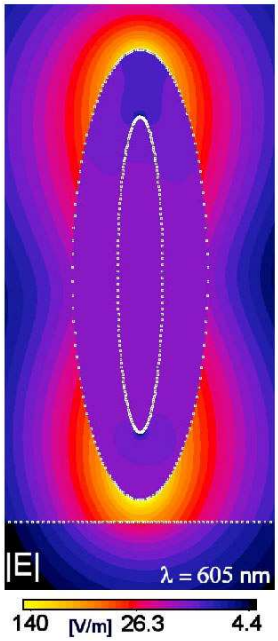


**Figure 2.22:** *MMP of the field distribution of an evanescently excited ellipsoidal particle with a glass core. From Ref.[18, 38].*

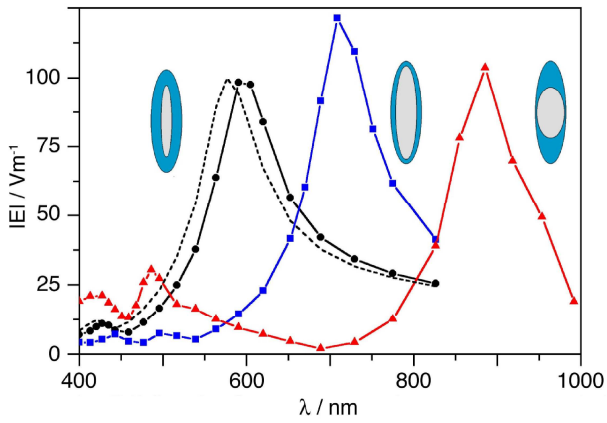


**Figure 2.23:** *Wavelength dependency of the field enhancement of ellipsoidal silver particle core sizes (calculated using MMP). From Ref.*[18, 38]

### 2.4.1.3 Polarization

As previously mentioned, a surface plasmon resonance (SPR) is induced by the electric field of an excitation source (usually a laser). The field enhancement depends critically on the laser beam polarization, which can be also deduced from theoretical modeling as mentioned earlier. If the electric field vector of the incident light is perpendicular (s-polarized) to the metal tip axis, the free electrons are driven to the sides lateral of the tip. As a result the tip apex remains uncharged. But if the electric field vector of the incident light is parallel (p-polarized) to the tip axis, the free electrons on the surface of the metal are confined to the end of the apex of tip (see Figure 2.24). As a consequence, the field enhancement is increasing. [32]

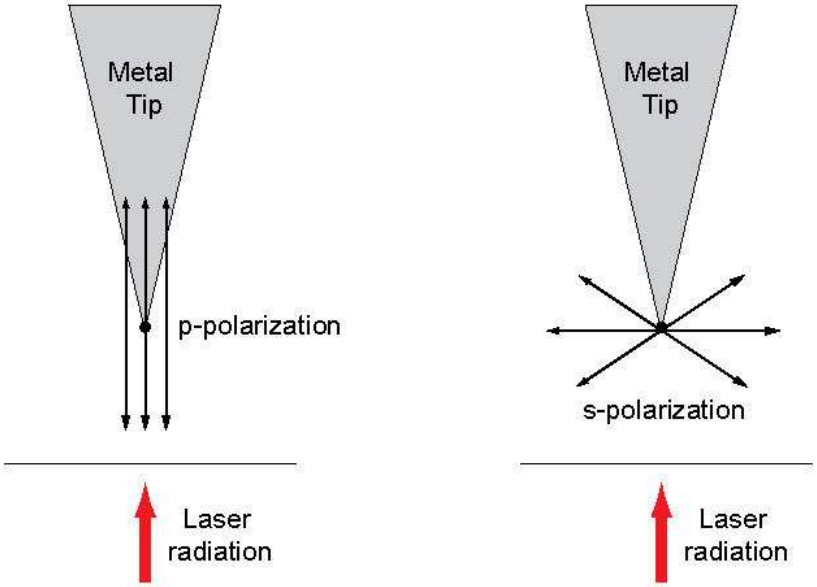


**Figure 2.24:** *Schematic diagram of s- and p-polarization at the tip.*

In a laser beam, the electric field, E, and the magnetic field, H, oscillate perpendicular to the propagation direction. By focusing with low numerical aperture (NA) lenses, the laser can be approximated as a Gaussian beam and the electric and magnetic fields remain transversal to the axis of the propagation in the focal region. On the other hand, we have to consider that a widely used illumination configuration in TERS at present is the back-reflection mode, which is illuminating the tip from the bottom (other illumination configurations will be discussed in the following sections). This configuration incorporates objective lenses with a high numerical aperture (NA) to improve the efficiency of both illumination and collection. In this case, the focus is very confined and the fields are not necessarily perpendicular to the general propagation direction.[40] In the tightly focused region orthogonal field vectors appear, in particular E-vector components that are almost parallel to the main propagation direction of the beam. These longitudinal fields are confined to the focal region.[41] When using high NA objective lenses, linearly polarized light is not the best choice because at the center of the focused spot the Z-components of the E-field cancel out. For a back-reflection set-up, the radial polarization mode shows an improvement in the Z-components of the E-

field providing a better tip-enhancement effect and the background signal decreases because these fields in general match the shape of the tip much better.[42]

For reflection modes with side illumination configuration, the largest enhancement is achieved when the E-fields of the incident radiation are parallel to the tip axis. That is because the near field (close to the vicinity of the tip apex) and far field (from unenhanced Raman, which could be considered as background) contributions show a different polarization, so the far-field component will be minimized using a parallel polarization with respect to the tip axis, which furthermore improves the near-field signal.[43, 44] For this geometry the proper illumination conditions are easier to fulfill, the problem is the poorer collection efficiency (NA) of such optical arrangements.

#### 2.4.1.4 Higher order optical effects

Tip-enhanced near-field optical microscopy is a technique that is mainly applied in combination with linear optical processes like Raman, IR or fluorescence , but the strong field enhancements involved can also be used to induce non-linear optical processes, such as second-harmonic generation (SHG), coherent anti-Stokes Raman spectroscopy (CARS), and Hyper-Raman.

Strong parallel E-field components can drive the dipole oscillating at the apex of the tip with a frequency ($2\omega$), twice the frequency of the excitation source ($\omega$). Then, a signal with the same frequency ($2\omega$) as the oscillating dipole is emitted from the tip with an angle ($\theta$) (see Figure 2.25). This is known as second-harmonic (SH) radiation.[45, 46]

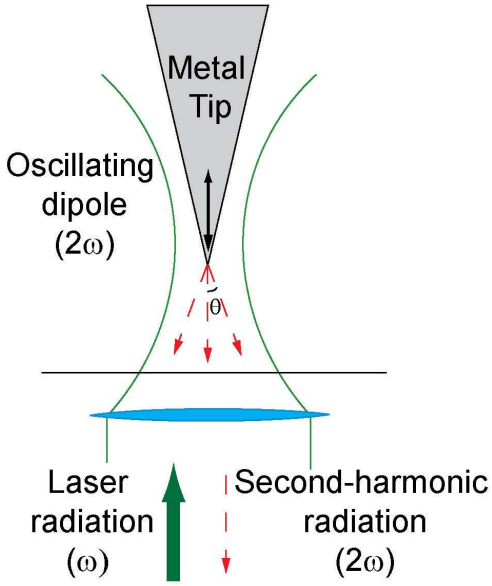


**Figure 2.25:** *Schematic diagram of a sharp metal tip which emits second-harmonic (SH) radiation at the critical angle of total internal reflection.*

Coherent anti-Stokes Raman scattering (CARS) is even a third-order nonlinear optical process that, in combination with tip-enhancement, provides a high spatial resolution and similar information content as Raman spectroscopy. DNA molecules and single walled carbon nanotubes (SWNTs) have been investigated by tip-enhanced coherent anti-Stokes spectroscopy (TE-CARS) at specific frequencies.[47, 48]

Another example for a non-linear method that it is applied together with plasmonic metal tips is hyper-Raman scattering (HRS). The observation of IR active bands of SWNTs using hyper-Raman TERS has been clearly demonstrated by Kawata *et al.*[49]

#### 2.4.1.5 Special effects in TERS

In a conventional Raman experiment, the change of polarizability caused by the electric field of the excitation source is the basis for the spontaneous Raman effect. However, when the applied high electric fields vary along a vibrational mode, the generated Raman signal which depends directly on the proportional polarizability changes. In this case, a polarizability gradient is present and the induced dipole is asymmetric. Therefore, new selection rules have to be considered and vibrations that are usually not Raman active can be observed. Such high field gradients can be induced on the surface of metal nanoparticles. If a sample is close to such a particle, the gradient field Raman (GFR) effect might be achieved. For bonds with a large polarizibility, the GFR should be very important. That means that vibrational infrared active modes should be detectable under large field gradient conditions, complementing the Raman spectra.[50]

Working with a single nanoparticle and sample features which are even smaller, additional effects can induce changes in band intensities and also in band positions.[51] In normal Raman scattering such changes can be explained by varying concentrations or different sample composition. The relationship between the distance dependency for the enhancement between tip and sample is a crucial issue.[33, 52, 53]

If the field enhancing capabilities of a TERS probe come close to a single molecule detection limit, it is important where the tip comes closest to the molecule. The usual averaging arguments do not hold in this case, because of the limited numbers of scatterers. Furthermore, the normal composition of sample versus Ag-tip does not necessarily resemble the computed minimized energy configurations. Tip and sample are ‘‘forced’’ into a certain arrangement. With respect to the measured TERS spectra, it is expected that they will closely resemble normal Raman or SERS spectra. But because of the limited number of molecules, it will be similar to single crystal Raman experiments with an unknown orientation of the sample. Last but not least, the measured spectra do not necessarily reflect the bulk properties of the specimen. This is because the TERS interaction region is confined to only a few nanometres and also the interaction with the substrate must be always considered as well. These small changes can provide additional information for the investigation of surfaces.

## 2.4.2 Experimental aspects in TERS

### 2.4.2.1 Instrumentation

The crucial attribute of a TERS experiment is a field enhancing metal feature or particle which is raster scanned across a sample surface.

An essential pre-requisite for any TERS experiment is a scanning probe microscope of some sort to provide a scanning stage that controls precisely the distance between particle and surface. Either atomic force microscopies (AFMs) or scanning tunneling microscopies (STMs) are presently used for this purpose. While the latter can control the distance more easily, STMs are restricted to either conductive samples or very thin layers of non-conductive samples on a conductive support. This restricts the generality of the method quite severely. For normal AFMs to be general tools, in particular for soft samples, they have to be operated in a non-contact mode of some sort to avoid sample damage. This always induces fluctuations in the optical signal due to the oscillation of the probe necessary to maintain feedback. Therefore a careful balance is required to optimize the TERS setup for a specific experiment.

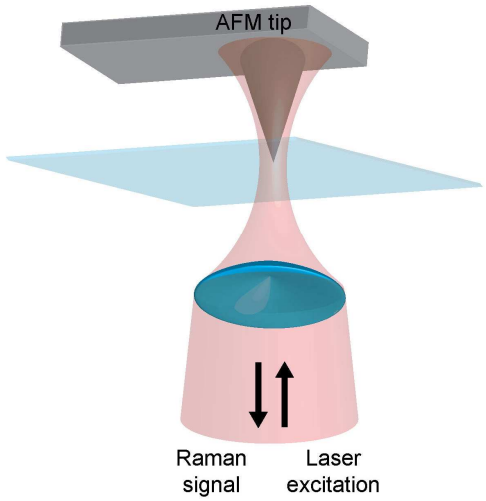


**Figure 2.26:** *Schematic diagram of a Tip-enhanced Raman scattering setup working in back-reflection mode.*

#### 2.4.2.2 TERS experiment

Figure 2.26 shows a schematic diagram of a tip-enhanced Raman scattering setup working in back-reflection mode. An inverted Raman microscope is coupled with an AFM for synchronized use. The microscope is required to illuminate the metal coated AFM tip.

The back scattered Raman signal is collected through the same objective and notch or edge filters are used to block the laser line. After this filter stage, the signal is coupled to a spectrometer equipped with a cooled charge coupled device (CCD) for spectrally resolved measurements.

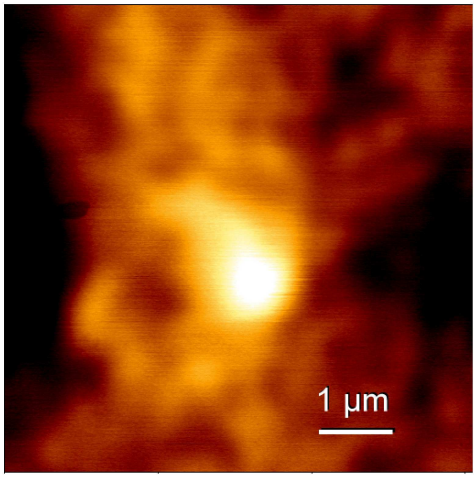


**Figure 2.27:** *Optical response of a TERS tip scanned through the laser focus. The bright spot corresponds to the convolution of the response functions of the optical microscope and the tip.*

The AFM is placed on the microscope so that the cantilever is roughly aligned with respect to the laser. The final alignment of the cantilever is done by scanning the tip through the laser focus, and collecting the reflected light using a simple photodiode. In Figure 2.27, the typical optical response image of a silver coated non-contact AFM tip is shown. This reflectivity image helps to finally position the tip at the position of highest signal intensity and then fix the tip in the x and y directions. At this point the second piezo-stage (sample stage) is activated and only the sample is moved. A piezo actuator synchronizes the microscope objective with the height feedback of the AFM tip to keep the tip always in focus. At this point usually several topographic images of the sample are recorded to find sites of interest on the surface for the actual TERS experiment.

### 2.4.2.3 Probe preparation

At present, there are several techniques which generate TERS probes with acceptable optical quality, but the reproducibility and yield of good tips are still a challenge. The two techniques most frequently used for TERS probe fabrication are electrochemical etching methods of solid metal probes and the metal evaporation deposition on AFM tips. Both methods will be discussed hereafter.

#### Pure metal tips

To enhance the Raman signal, mainly metals like gold, silver or copper are used. Thus far, the best TERS enhancement factors have been demonstrated with gold and silver. Compared to normal SERS experiments, gold is used more frequently because gold tips are easy to manufacture. To produce the desired sharp edges required for the TERS experiments, metal wires can be sharpened using electrochemical etching procedures. Many methods have been developed for STM probes, but the overall geometry of the tip is usually less critical in this case. In TERS, a good quality refers to a larger part of the tip because naturally the interaction with the optical fields extends further than the tunnel effect involved in STM.

In the case of gold tips, the electrochemical etching procedures are well established and involve mainly a voltage between a gold wire and a metal ring electrode, both dipped in concentrated hydrochloric acid solution.[54] Between the ring and the gold wire a large surface tension is formed and the etching proceeds more quickly in the meniscus region. During the reaction, the wire becomes thinner until it breaks and falls down. At this moment the electrical circuit is switched off.

Silver in general has better optical properties with respect to the surface enhancement than gold. However, a different electrochemical etching procedure to prepare sharp silver tips for TERS is required. Mainly two methods are being used. In the first, a silver wire is dipped in a solution of ammonia 10-35%. A stainless steel plate acts as electrode. In this case, no ring is employed and there is no meniscus effect (Figure 2.28).[55] The second procedure uses an aqueous solution of 60% perchloric

acid and ethanol (1:2) to form a lamella with an Ag ring that acts as a cathode. A silver wire (anode) is then dipped into the lamella and the voltage is applied.[56]

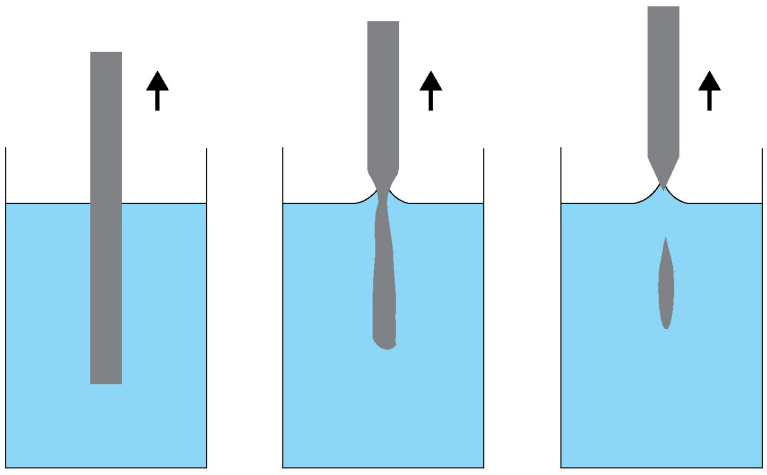

**Figure 2.28:** *Schematic diagram of the electrochemical cell for the Ag etching procedure.*

**AFM tip as templates**

Another route to prepare metal tips with a very small radius is to employ a sharp commercial AFM tip (diameter < 10 nm) as a template and coat it with the desired metal. Again different methods can be applied.

The most simple method to place nanoparticles at the edge of an AFM tip is by evaporation of thin metal films similar to procedures known to provide silver island films[31] (see Figure 2.29).

Another interesting approach is the generation of colloidal nanoparticles at the tip. A suitable example is shown in Wang *et al*.[57] Here, the AFM tip is immersed in a colloid solution produced by Tollen's reaction.

Not only AFM tips can be used as templates. Normal optical fibers can also be etched similarly to the production of aperture near-field probes to obtain the desired tip shape.[58] Also melt drawing of glass rods provides satisfactory TERS templates.

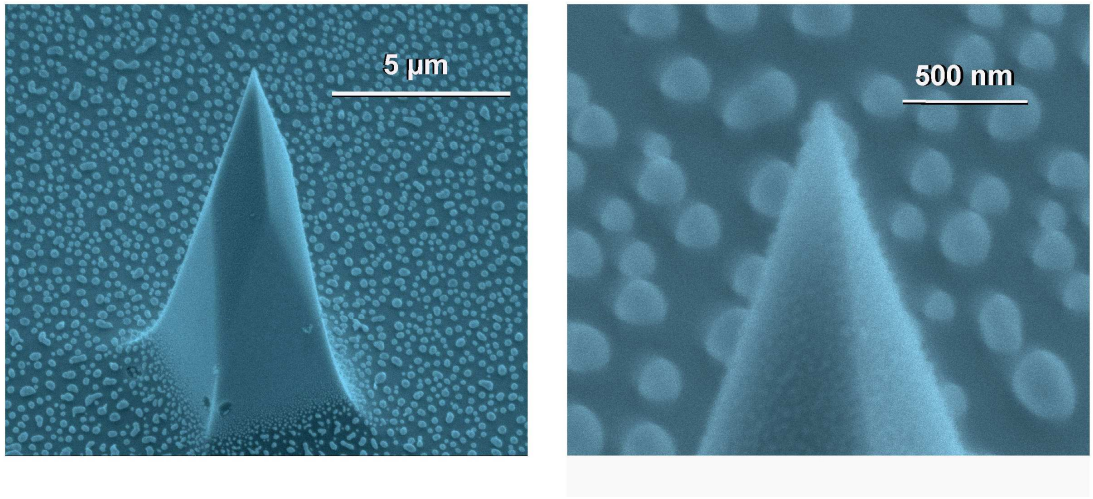


**Figure 2.29:** *SEM image of a silver-coated AFM tip.*

**Post-treatment by Focused Ion Beam (FIB) Milling**

FIB milling can be used as post-treatment to shape tips, e.g. after electrochemical etching. However this procedure is very expensive. FIB is applied as a technique to produce rational nanostructures that are required for specific design of optical nano-antennas. More sophisticated methods employs a bow-tie antenna with a nano-gap at the very end of a metal coated AFM tip is shown in

Figure 2.30.[59] The high precision of FIB allows the control of the length and width of the nano-particles as antenna structures and in the case of the bow-tie, also the gap. By manipulating these parameters tips for specific wavelength excitation can be fabricated.

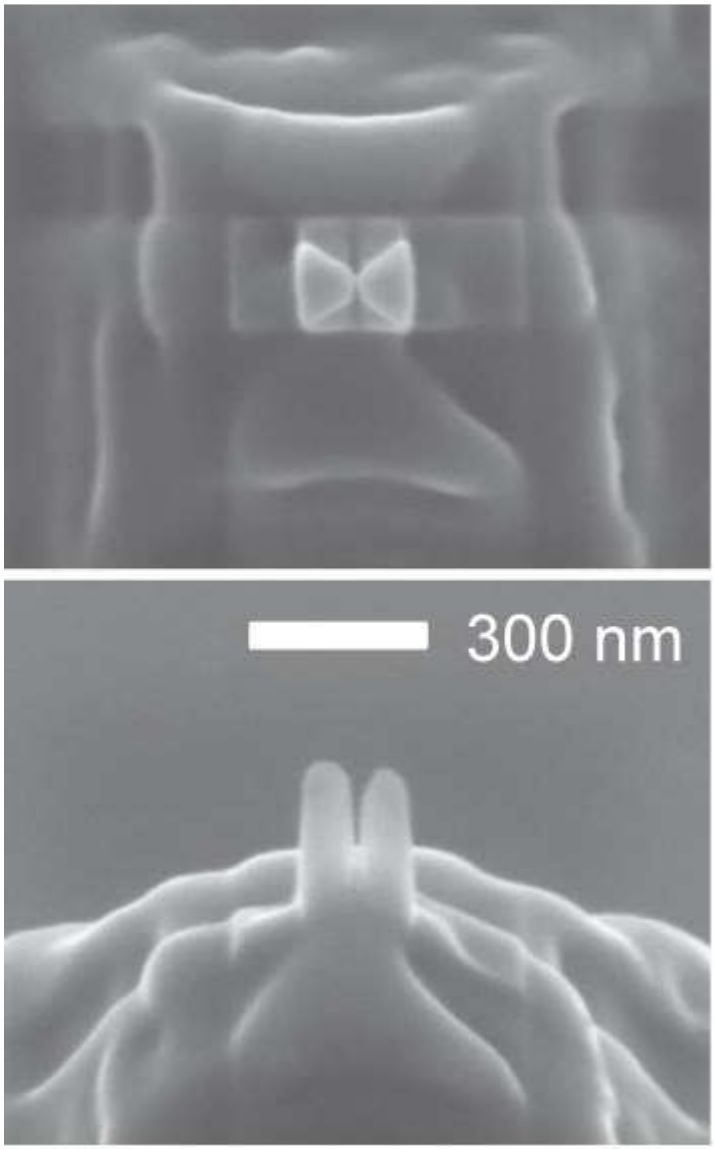


**Figure 2.30:** *SEM image of a bow-tie of a metal-coated AFM-tip after FIB milling. From Ref.*[59]

### 2.4.2.4 Configurations

One of the main challenges in TERS is the low contrast between the near-field and the far-field signal. As demonstrated by Sun *et al.*[60] the Raman signal produced from the near-field (enhanced Raman from the tip apex) was estimated to be only 35%, while the remaining signal (65%, unenhanced Raman) was collected from the far-field. This low contrast can be improved by the illumination configuration, which has a major influence on the enhancement properties of the electromagnetic field at the apex of the tip.

#### Reflection setup

Several modes such as side-illumination and top-illumination could be realized in a reflection setup (see Figure 2.31). The major advantage of the reflection mode is that the sample can be opaque. A disadvantage is the low contrast between the near-field and far-field signals because of the unfavorable ratio between the illuminated and enhanced areas. This problem can be partly solved by applying a suitable polarized configuration.[43, 44]

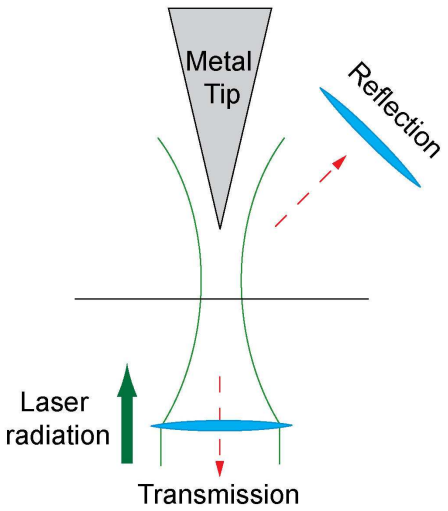


**Figure 2.31:** *Schematic diagram of reflection and transmission illumination configuration of TERS experiments.*

**Back-reflection setup**

The TERS setup with in back reflection mode, has been discussed[21, 22, 31] already in Section 2.4.2.2. Here, the tip is illuminated from below using an immersion oil objective with a high numerical aperture. The Raman signal is collected by the same objective. This configuration ensures a high efficiency and avoids a large contribution of enhanced signal compared to the standard reflection mode. The major shortcoming for this configuration is the restriction to transparent samples.

In conclusion, the choice for the optimal TERS configuration critically depends on the specific requirements of the samples involved. The appropriate illumination mode configuration for a TERS experiment will depend on the transparency of the sample. The choice of the proper tip depends on the spectral absorption characteristics of the sample and therefore which excitation wavelength is desirable. Finally, the feedback system required depends either on the conductivity properties or the thickness of the sample.

## 2.5 References


[1] C. V. Raman, K. S. Krishnan. A new type of Secondary Radiation. *Nature* **1928**, *121*, 501.

[2] A. Einstein. Zur Quantentheorie der Strahlung. *Phys. Z.* **1917**, *18*, 121.

[3] T. H. Maiman. Stimulated Optical Radiation in Ruby. *Nature* **1960**, *187*, 493

[4] http://en.wikipedia.org/wiki/Population_inversion#Three-level_lasers.

[5] M. Fleischmann, P. J. Hendra, J. McQuillan. Raman spectra of pyridine adsorbed at a silver electrode *Chem. Phys. Lett.* **1974**, *26*, 163.

[6] M. G. Albrecht, J. A. Creighton. Anomalously intense Raman spectra of pyridine at a silver electrode. *J. Am. Chem. Soc.* **1977**, *99*, 5215.

[7] D. L. Jeanmaire, R. P. Van Duyne, A. P. Sloan. Surface raman spectroelectrochemistry: Part I. Heterocyclic, aromatic, and aliphatic amines adsorbed on the anodized silver electrode *J. Electroanal. Chem.* **1977**, *84*, 1.

[8] K. Faulds, R. E. Littleford, D. Graham, G. Dent, W. E. Smith. Comparison of Surface-Enhanced Resonance Raman Scattering from Unaggregated and Aggregated Nanoparticles. *Anal. Chem.* **2004**, *76*, 592.

[9] K. K. Sang-Woo Joo. Adsorption of phenylacetylene on gold nanoparticle surfaces investigated by surface-enhanced Raman scattering. *J. Raman Spectrosc.* **2004**, *35*, 549.

[10] N. R. Jana, L. Gearheart, C. J. Murphy. Wet Chemical Synthesis of High Aspect Ratio Cylindrical Gold Nanorods. *J. Phys. Chem. B* **2001**, *105*, 4065.

[11] Y. Sun, Y. Xia. Mechanistic Study on the Replacement Reaction between Silver Nanostructures and Chloroauric Acid in Aqueous Medium. *J. Am. Chem. Soc.* **2004**, *126*, 3892.

[12] C. J. Murphy, N. R. Jana. Controlling the Aspect Ratio of Inorganic Nanorods and Nanowires. *Adv. Mat.* **2002**, *14*, 80.

[13] A. Wokaun, J. P. Gordon, P. F. Liao. Radiation damping in surface-enhanced Raman scattering. *Phys. Rev. Lett.* **1982**, *48*, 957.

[14] P. W. Barker, R. K. Chang, H. Massoudi. *Phys. Rev. Lett.* **1983**, *50*, 997.

[15] J. Wessel. Surface-enhanced optical microscopy. *J. Opt. Soc. Am.* **1985**, *2*, 1538.

[16] S. Nie, S. R. Emory. Probing single molecules and single nanoparticles by surface-enhanced Raman scattering. *Science* **1997**, *275*, 1102.

[17] S. R. Emory, S. Nie. Near-field surface-enhanced Raman spectroscopy on single silver nanoparticles. *Anal. Chem.* **1997**, *69*, 2631.

[18] E. Bailo, V. Deckert. Tip-enhanced Raman scattering. *Chem. Soc. Rev.* **2008**, *37*, 921.

[19] M. S. Anderson. Locally enhanced Raman spectroscopy with an atomic force microscope. *Appl. Phys. Lett.* **2000**, *76*, 3130.

[20] N. Hayazawa, Y. Inouye, Z. Sekkat, S. Kawata. Metallized tip. amplification of near-field Raman scattering. *Opt. Commun.* **2000**, *183*, 333.

[21] R. M. Stöckle, Y. D. Suh, V. Deckert, R. Zenobi. Nanoscale chemical analysis by tip-enhanced Raman spectroscopy. *Chem. Phys. Lett.* **2000**, *318*, 131.

[22] A. Hartschuh, E. J. Sánchez, X. S. Xie, L. Novotny. High-Resolution Near-Field Raman Microscopy of Single-Walled Carbon Nanotubes. *Phys. Rev. Lett.* **2003**, *90*, 095503.

[23] B. Pettinger, G. Picardi, R. Schuster, G. Ertl. Surface-enhanced and STM-tip-enhanced Raman Spectroscopy at Metal Surfaces. *Single Mol.* **2002**, *3*, 285.

[24] A. Hartschuh. Tip-Enhanced Near-Field Optical Microscopy. *Angew. Chem.* **2008**, *47*, 8178.

[25] D. Richards. Near-field microscopy: throwing light on the nanoworld. *Phil. Trans. R. Soc. Lond. A* **2003** 2843.

[26] I. Notingher, C. Mellor. *http://www.nottingham.ac.uk/physics/research-/nano/lipidmembranes.htm* **2007**.

[27] A. Campion, P. Kambhampati. Surface Enhanced Raman Scattering. *Chem. Soc. Rev.* **1998**, *27*, 241.

[28] M. Moskovits. Surface-enhanced spectroscopy *Rev. Mod. Phys.* **1985**, *57*, 783.

[29] P. Verma, K. Yamada, H. Watanabe, Y. Inouye, S. Kawata. Near-field Raman scattering investigation of tip effects on C60 molecules. *Phys. Rev. B.* **2006**, *73*, 045416.

[30] H. Watanabe, Y. Ishida, N. Hayazawa, Y. Inouye, S. Kawata. Tip-enhanced near-field Raman analysis of tip-pressurized adenine molecule. *Phys. Rev. B* **2004**, *69*, 155418.

[31] A. Rasmussen, V. Deckert. Surface- and tip-enhanced Raman scattering of DNA components. *J. Raman Spectrosc.* **2006**, *37*, 311.

[32] L. Novotny, R. X. Bian, X. S. Xie. Theory of Nanometric Optical Tweezers. *Phys. Rev. Lett.* **1997**, *79*, 645.

[33] J. Renger, S. Grafström, L. M. Eng, V. Deckert. Evanescent wave scattering and local electric field enhancement at ellipsoidal silver particles in the vicinity of a glass surface. *J. Opt. Soc. Am. A* **2004**, *21*, 1362.

[34] F. Festy, A. Demming, D. Richards. Resonant excitation of tip plasmons for tip-enhanced Raman SNOM. *Ultramicroscopy* **2004**, *100*, 437.

[35] J. T. Krug, E. J. Sanchez, X. S. Xie. Design of near-field optical probes with optimal field enhancement by finite difference time domain electromagnetic simulation. *J. Chem. Phys.* **2002**, *116*, 10895.

[36] Y. C. Martin, H. F. Hamann, H. K. Wickramasinghe. Strength of the electric field in apertureless near-field optical microscopy. *J. Appl. Phys.* **2001** *89* 5774.

[37] M. Micic, N. Klymyshyn, Y. D. Suh, H. P. Lu. Finite Element Method Simulation of the Field Distribution for AFM Tip-Enhanced Surface-Enhanced Raman Scanning Microscopy. *J. phys. Chem. B* **2003**, *107*, 1574.

[38] I. Hellmann, Diploma Thesis, Technischen Universität Dresden (Dresden), **2003**.

[39] Y. C. Martin, H. F. Hamann, H. K. Wickramasinghe. Strength of the electric field in apertureless near-field optical microscopy. *J. Appl. Phys.* **2001** *89* 5774.

[40] B. Hecht, B. Sick, U. P. Wild, V. Deckert, R. Zenobi, O. J. F. Martin, D. W. Pohl. Scanning near-field optical microscopy with aperture probes: Fundamentals and applications. *J. Chem. Phys.* **2000**, *112*, 7761.

[41] L. Novotny, M. R. Beversluis, K. S. Youngworth, T. G. Brown. Longitudinal Field Modes Probed by Single Molecules. *Phys. Rev. Lett.* **2001**, *86*, 5251.

[42] Y. Saito, N. Hayazawa, H. Kataura, T. Murakami, K. Tsukagoshi, Y. Inouye, S. Kawata. Polarization measurements in tip-enhanced Raman spectroscopy applied to single-walled carbon nanotubes. *Chem. Phys. Lett.* **2005**, *410*, 136.

[43] D. Mehtani, N. Lee, R. D. Hartschuh, A. Kisliuk, M. D. Foster, A. P. Sokolov, J. F. Maguire. Nano-Raman spectroscopy with side-illumination optics. *J. Raman Spectrosc.* **2005**, *36*, 1068.

[44] Q. Nguyen, R. Ossikovski, J. Schreiber. Contrast enhancement on crystalline silicon in polarized reflection mode tip-enhanced Raman spectroscopy. *Opt. Commun.* **2007**, *274*, 231.

[45] A. Bouhelier, M. Beversluis, A. Hartschuh, L. Novotny. Near-Field Second-Harmonic Generation Induced by Local Field Enhancement. *Phys. Rev. Lett.* **2003**, *90*, 013903.

[46] A. V. Zayats, T. Kalkbrenner, V. Sandoghdar, J. Mlynek. Second-harmonic generation from individual surface defects under local excitation. *Phys. Rev. B* **2000**, *61*, 4545.

[47] T. Ichimura, N. Hayazawa, M. Hashimoto, Y. Inouye, S. Kawata. Tip-Enhanced Coherent Anti-Stokes Raman Scattering for Vibrational Nanoimaging. *Phys. Rev. Lett.* **2004**, *92*, 220801.

[48] S. Kawata, P. Verma. Optical Nano-Imaging of Materials: Peeping Through Tip-Enhanced Raman Scattering. *CHIMIA Int. J. Chem.* **2006**, *60*, 770.

[49] K. Ikeda, Y. Saito, N. Hayazawa, S. Kawata, K. Uosaki. Resonant hyper-Raman scattering from carbon nanotubes. *Chem. Phys. Lett.* **2007**, *438*, 109.

[50] E. J. Ayars, H. D. Hallen, C. L. Jahncke. Electric Field Gradient Effects in Raman Spectroscopy. *Phys. Rev. Lett.* **2000**, *85*, 4180.

[51] E. Bailo, V. Deckert. Tip-enhanced Raman spectroscopy of single RNA strands: Towards a novel direct sequencing method. *Angew. Chem. Int. Ed.* **2008**, *47*, 1658.

[52] A. Downes, D. Salter, A. Elfick. Finite Element Simulations of Tip-Enhanced Raman and Fluorescence Spectroscopy. *J. Phys. Chem. B* **2006**, *110*, 6692.

[53] D. Richards, R. G. Milner, F. Huang, F. Festy. Tip-enhanced Raman microscopy: practicalities and limitations. *J. Raman Spectrosc.* **2003**, *34*, 663.

[54] B. Ren, G. Picardi, B. Pettinger. Preparation of gold tips suitable for tip-enhanced Raman spectroscopy and light emission by electrochemical etching. *Rev. Sci. Instrum.* **2004**, *75*, 837.

[55] K. Dickmann, F. Demming, J. Jersch. New etching procedure for silver scanning tunneling microscopy tips. *Rev. Sci. Instrum.* **1996**, *67*, 845.

[56] L. Zhu, J. Atesang, P. Dudek, M. Hecker, J. Rinderknecht, Y. Ritz, H. Geisler, U. Herr, R. Geer, E. Zschech. Experimental challenges for approaching local strain determination in silicon by nano-Raman spectroscopy. *Mater. Sci.-Poland* **2007**, *25*.

[57] J. J. Wang, Y. Saito, D. N. Batchelder, J. Kirkham, C. Robinson, D. A. Smith. Controllable method for the preparation of metalized probes for efficient scanning near-field optical Raman microscopy. *Appl. Phys. Lett.* **2005**, *86*, 263111.

[58] R. Stöckle, C. Fokas, V. Deckert, R. Zenobi, B. Sick, B. Hecht, U. P. Wild. High-quality near-field optical probes by tube etching. *Appl. Phys. Lett.* **1999**, *75*, 160.

[59] J. N. Farahani, H.-J. Eisler, D. W. Pohl, M. Pavius, P. Flückiger, P. Gasser, B. Hecht. Bow-tie optical antenna probes for single-emitter scanning near-field optical microscopy. *Nanotechnology* **2007**, *18*, 125506.

[60] W. X. Sun, Z. X. Shen. A practical nanoscopic Raman imaging technique realized by near-field enhancement. *Mater.Phys.Mech* **2001**, *4*, 17.

# Chapter 3

# Experimental Part

## 3.1 TERS Setup

The general setup of the TERS instrument has been described in section 1.5.2 and elsewhere.[1] A schematic diagram of the TERS set-up employed in this work is shown in Figure 3.1.TERS spectra were recorded with an inverted Raman microscope (Jobin Yvon-Horiba LabRam invers HR, France) coupled to an AFM (NanoWizard atomic force microscope, JPK Instrument AG, Germany) working in non-contact mode (intermittent mode). The laser beam (@ 530 nm, Coherent Innova I302C Krypton ion laser, USA) is reflected from a holographic notch filter and focused on the tip from below using an oil immersion objective (x60, N.A. 1.45, Olympus, Japan). Laser light can be directed to the photodiode so the tip can be aligned and the power carefully monitored. The Raman light is back scattered from the tip through the notch filter, where the Rayleigh line is removed, and then onto the grating (600 groove/mm) in the spectrometer. The read out is recorded on a CCD and the spectrum displayed on the monitor. For all TERS measurements the laser intensity at the sample was set between 200 µW to 1 mW resulting in acquisition times between 1 to 15 s, depending on the nature of the sample and the efficiency of the tip. All experiments were performed at room temperature and ambient pressure. All the spectra shown are raw data, no baseline-correction or smoothing procedures were applied and all the spectral data analyses were carried out with Igor Pro 4.07 software (WaveMetrics, Inc.).

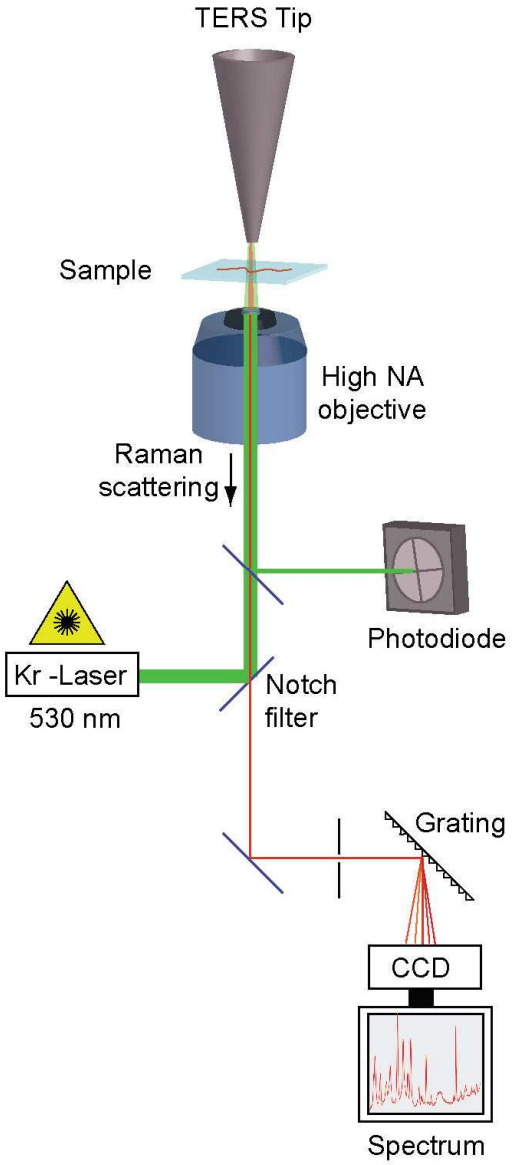


**Figure 3.1:** *Schematic of the back-reflection TERS set-up used in this work.*

## 3.2 Tip preparation

For the TERS experiment a non-contact mode silicon cantilever AFM tip (NSG10, NT-MDT) was coated with 20 nm of silver (99.99% pure, Balzers Materials) by thermal evaporation (BAL-TEC MDS 020 BAL-TEC GmbH) at an evaporation rate of 0.06 nm/s. Figure 3.2 shows a commercial silicon AFM tip before (a, b) and after (c, d) the silver deposition. The average diameter of the apex of the coated tips is estimated to be approximately 20 nm. The tips were then stored under argon and were used within two days. [1-6]

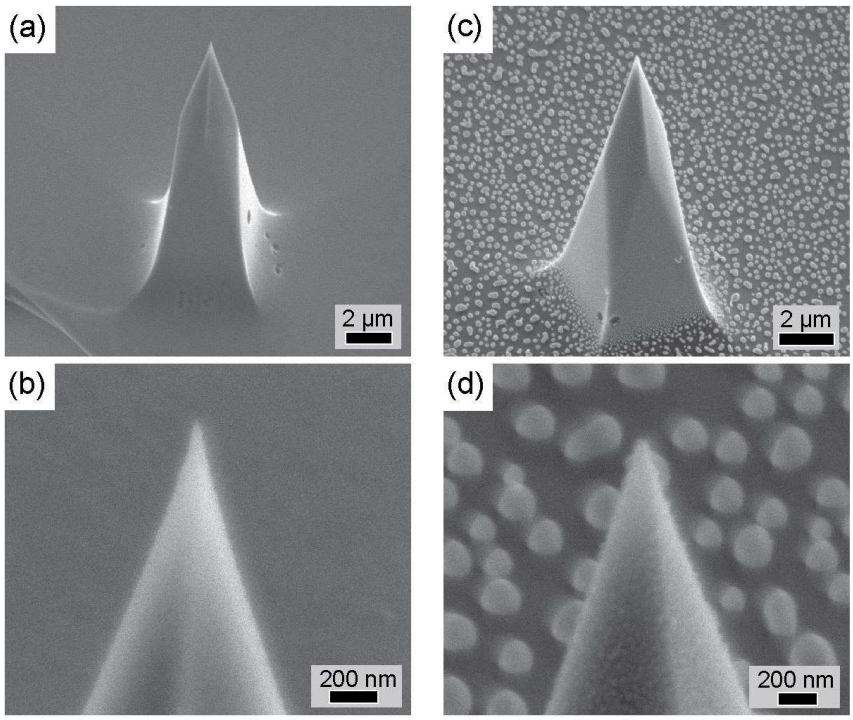


**Figure 3.2:** *SEM images of a silicon AFM tip (a,b) and after 20 nm Ag vapor-deposition (c,d). (TERS tip was prepared by B. Gosciniak and SEM pictures were recorded by E. Pulvermacher.)*

## 3.3 Sample preparation

In order to perform satisfactory TERS measurements with a back-reflection set-up, it is important to take into account level of transparency and thickness of the sample and sample substrate. To avoid losses of the back scattered Raman signal and power of the excitation laser source, the sample and sample substrate should be transparent. The objective used has a low working distance (0.17 mm), for that reason the thickness of the sample substrate is limited. For this work, thin glass cover slips (0.15 mm thickness, Marienfeld GmbH, Germany) or mica substrates (<0.1 mm thickness, Bal-Tec GmbH, Liechtenstein) have been used as sample substrates.

The glass cover slips were previously cleaned in a digestion mixture of concentrated $HNO_3$: 30% $H_2O_2$ (3:1) for 2 hours, subsequently rinsing with bidistilled water five times and dried under vacuum. The mica substrate was freshly cleaved prior to use, by making a small cut between to layers with a razor blade and taking both apart.

For each sample, any special sample preparation procedure will be described in the corresponding chapter.

## 3.4 Challenges

One of the major difficulties of TERS is the low reproducibility of the Ag-vapor coated tip. The silver nanoparticles are randomly positioned at the apex of the tip, leading to only 20% on average of excellent TERS tips which provide high Raman signal enhancements at the excitation wavelength.

Additionally, even if the Ag-coated AFM tip is working in non-contact mode (intermittent mode), the tip can be damaged during the measurement and crash into the sample. As a result, the Ag particle deposited at the end of the tip can removed, or get damaged (Figure 3.3.a) and/or contaminated with sample material (Figure 3.3.b). To avoid this, tips were constantly controlled during the running experiment by measuring at substrate sites without sample.

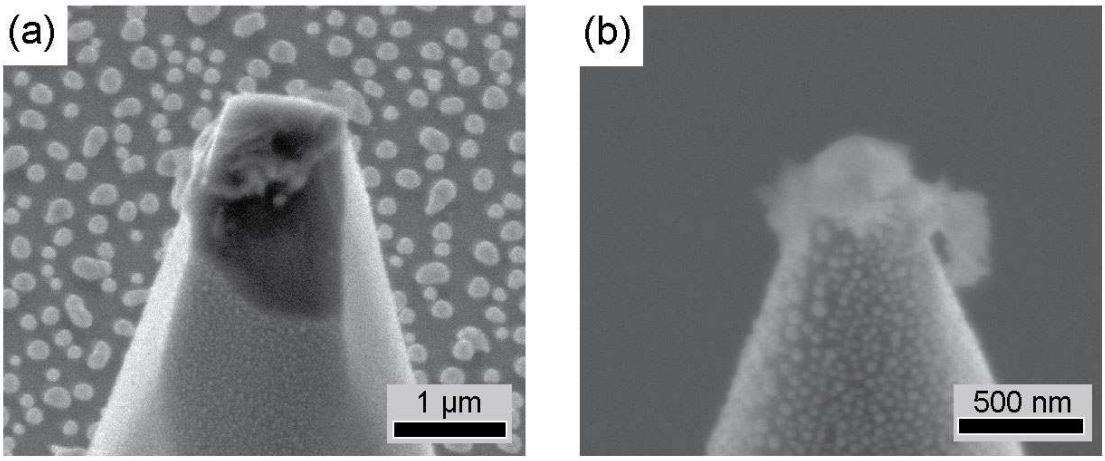


**Figure 3.3:** *SEM images of (a) a crashed and (b) sample-contaminated Ag-coated AFM tip.*

## 3.5 References

[1] A. Rasmussen, V. Deckert. Surface- and tip-enhanced Raman scattering of DNA components. *J. Raman Spectrosc.* **2006**, *37*, 311.

[2] E. Bailo, V. Deckert. Tip-enhanced Raman spectroscopy of single RNA strands: Towards a novel direct sequencing method. *Angew. Chem. Int. Ed.* **2008**, *47*, 1658.

[3] E. Bailo, V. Deckert. Tip-enhanced Raman scattering. *Chem. Soc. Rev.* **2008**, *37*, 921.

[4] C. Budich, U. Neugebauer, J. Popp, V. Deckert. Cell wall investigations Utilizing Tip-enhanced Raman Scattering. *J. Microsc.* **2008**, *229*, 533.

[5] U. Neugebauer, P. Rösch, M. Schmitt, J. Popp, C. Julien, A. Rasmussen, C. Budich, V. Deckert. On the Way to Nanometer-Sized Information of the Bacterial Surface by Tip-Enhanced Raman Spectroscopy. *ChemPhysChem* **2006**, *7*, 1395.

[6] U. Neugebauer, U. Schmid, K. Baumann, W. Ziebuhr, S. Kozitskaya, V. Deckert, M. Schmitt, J. Popp. Towards a Detailed Understanding of Bacterial Metabolism - Spectroscopic Characterization of Staphylococcus Epidermidis. *ChemPhysChem* **2007**, *8*, 124.

# Chapter 4

# SERS as a Tool to Probe Cytochrome P450-Catalysed Substrate Oxidation[1]

Spectroscopic methods are irreplaceable tools in analytical chemistry particularly for the analysis of biomolecules. Although X-ray analysis provides an unmatched precision and data quality concerning proteins, it is often very difficult to obtain suitable crystals for analysis in particular to study protein-ligand binding. On the other hand, vibrational spectroscopy, particularly the Raman-based spectroscopy methods, such as surface-enhanced Raman scattering (SERS), can provide insight into the internal configuration, structure and dynamics of proteins including substrate binding and protein interactions in solution or on their poly crystalline form. SERS and its resonance counterpart, SERRS, have emerged as powerful tools for biomolecule detection with reported single molecule sensitivity.[2-6] Based on the enhancement of vibrational modes in the presence of strong localized surface plasmons induced by the interaction of light with rough noble metal surfaces, SERS has been recently used in the detection of a large range of biomolecules and for the study of biomolecular events.[7-10] A variety of metal surfaces can be used to generate SERS spectra, however, the reproducibility of generating solid substrates for SERS measurements largely depends on the target biomolecule.[11] Suitable SERS surfaces include gold and silver colloids,[12-14] nanoparticles deposited on surfaces,[15] such as silica spheres, designed metal nanostructures[16, 17] and metal island films produced by laser deposition.[18] In many SERS-based studies of protein analytes, this method is employed to determine protein-ligand interactions, often realised by using Raman dye

labelled gold or silver nanoparticle probes, which enable selective and sensitive spectroscopic detection. Recently the strong interaction between proteins and silver nanoparticles was employed to achieve silver staining of human immunoglobulin G (IgG) antibodies after their interaction with dye-labelled anti-human IgG.[19] Using this technique, spectra of dye labelled immunocomplexes were obtained with detection limits even lower than 1 pg/mL. This and other studies, such as the SERS detection of enzyme reaction products or SERS sensitive substrates based on masked azo benzotriazol dyes for studies of lipase and protease activity, clearly indicate the potential of SERS for applications in ultrasensitive protein detection assays.[20-22]

## 4.1 Heme proteins & SERS

Many important proteins for biomedical research and biotechnological applications contain a non-diffusible cofactor, often termed as a prosthetic group. Among these proteins, heme proteins, which contain the heme (iron protoporphyrin IX) moiety as the prosthetic group, play a prominent role. Heme proteins maintain three general biological functions, in particular, the transport of electrons (e.g. cytochrome b5), the transport of oxygen (e.g. hemoglobin) and the catalysis of various metabolitic reactions. The latter are conducted, for instance, by peroxidases and monooxygenases belonging to the large family of cytochrome P450 enzymes.[23, 24] P450 enzymes are also of particular importance for in vitro applications in biosensing and biocatalysis, because they catalyse a broad range of reactions, such as the oxidation of non-activated C-C bonds, which are very difficult to achieve in synthetic organic chemistry (see Figure 4.1).[25-28]

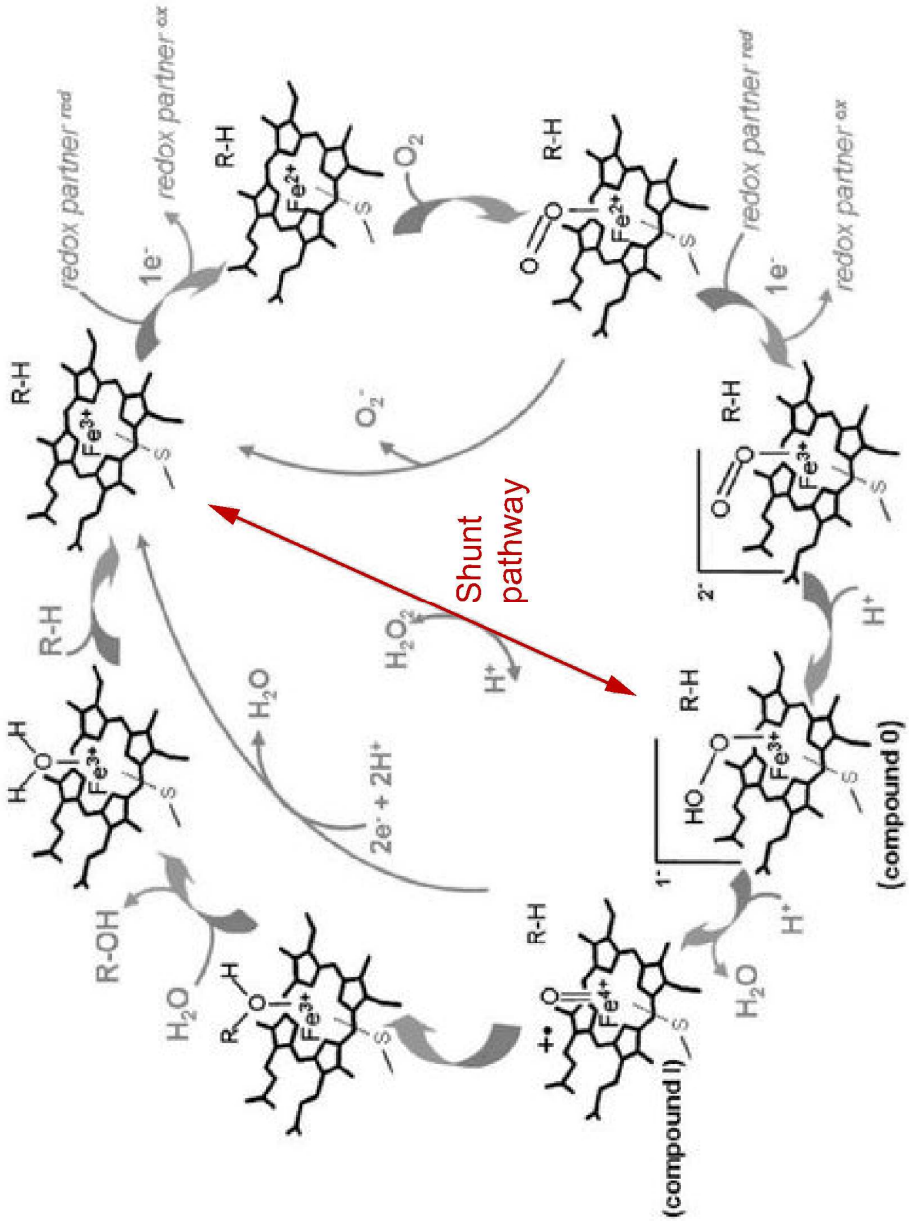


**Figure 4.1:** *The catalytic cycle of cytochrome P450. From Ref.*[28]

Despite the variety of known heme proteins, their structural analogy in terms of the iron protoporphyrin IX moiety (heme, Figure 4.2) as their active site, enables an universal approach to the spectroscopic analysis. In particular, the π-π* transitions occurring in the heme induce rich spectral changes, which can also be utilised for SERS detection. For instance, SERS has been used for studying the redox processes and interfacial electron transfer reactions of cytochrome c, the detection of hemoglobin on the single molecule level, the investigation of ligand binding in myoglobin and horseradish peroxidase, and to asses structural changes in P450 BM3 upon substrate binding.[29-32] In the context of our ongoing studies on the development of novel cytochrome P450 enzymes[33] we report on the application of SERS to investigate the interactions of fatty acid substrates with the enzyme cytochrome $P450_{BS\beta}$ and demonstrate the detection of binding events by SERS.

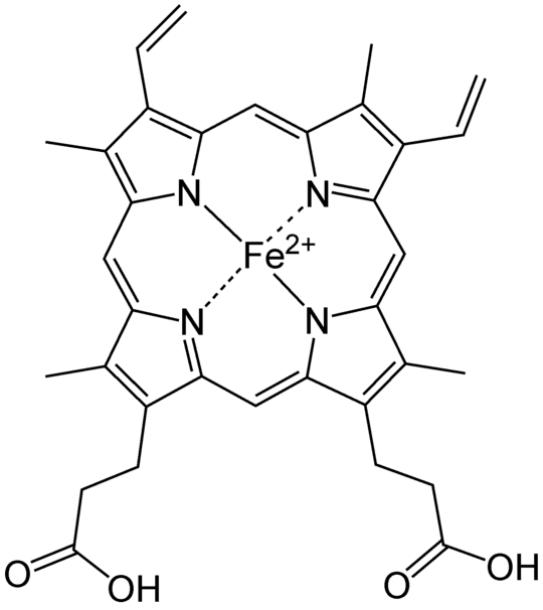


**Figure 4.2:** *Molecular structure of heme.*

## 4.2 SERS on Cytochrome $P450_{BS\beta}$ interactions

Bacterial cytochrome $P450_{BS\beta}$ catalyses the hydroxylation reaction of long chain fatty acids, such as myristic acid.[34] The oxygen atom required for the hydroxylation reaction of P450s is usually derived from molecular oxygen through mediation of the NADH reductase system and flavoproteins. However, $P450_{BS\beta}$ can be activated by the simple addition of hydrogen peroxide ($H_2O_2$), taking advantage of the so-called “shunt pathway” and unlike other monooxygenases such as P450 BM3, it binds the fatty acid substrate in close proximity to the heme active site.[35-37] We therefore reason that SERS analysis of a heme cofactor should provide an insight into the substrate binding and thus may eventually enable screening assays to identify potential enzymatic

substrates. Macdonald *et al*.[31] have previously carried out structural studies of substrate binding for P450 BM3 using SERRS. They demonstrated the feasibility of this approach to probe substrate/prosthetic group interactions within the active site, even at low protein concentrations.[31, 38, 39] Following this approach, here we report our proof of concept study, to employ SERS for the distinction of interactions occurring between binding and non-binding substrates of $P450_{BS\beta}$. For this purpose, we use two fatty acid substrates, myristic acid (MA) and hydroxylauric acid (HLA) which are known to be the substrate and the product, respectively, of the oxidation reaction in presence of $P450_{BS\beta}$.[34]

Silver colloids were used as a SERS active substrate in all of the experiments and NaCl as an aggregating agent (see Figure 4.3). We observed that the aggregation of the colloid does not occur or, in some cases, proceeds very slowly, if the enzyme is added to the colloid prior to aggregation agent. This is most probably due to the strong interaction of the positively charged protein and the negatively charged Ag surface (covered with citrate moieties), which prevents the aggregation and therefore formation of metal clusters with the high field enhancement necessary for SER scattering. Hence, all experiments were preformed with pre-aggregated Ag colloid. To investigate optimal conditions several other aggregating agents such as $MgCl_2$, spermine and ascorbic acid were tested, but NaCl was found to be the most suitable for the described experiments. It is known that due to the orientation of the protein on the surface, a certain degree of protein unfolding occurs at submonolayer coverage.[5, 31, 39] To avoid such an unwanted effect, the protein/surface coverage in our case was maintained above monolayer coverage using a higher protein concentration (5 µM). The spectra of substrate-free enzyme (Figure 4.4.a), enzyme mixed with $H_2O_2$ (Figure 4.4.c), myristic acid (substrate, MA) (Figure 4.4.b), hydroxylauric acid (Figure 4.5.b) (not binding substrate, HLA) were all recorded separately. No spectra of free fatty acids were obtained because the negatively charged matrix of citrate moieties on the Ag surface prevents binding of negatively charged fatty acids. Therefore, peaks obtained in the SERS spectra originate exclusively from vibrational modes of the enzyme. In Figure 4.4.a the spectrum of free enzyme is shown. The signals are dominated by the in-plane porphyrin ring modes of the heme groups covering the frequency range of 1100-1700 $cm^{-1}$. The peaks at 1594, 1578, 1450 (shoulder at 1430 $cm^{-1}$), 1327 and 1263 $cm^{-1}$ can

be used as “marker” modes and are known to be sensitive to oxidation, coordination and spin states of the heme iron. Additionally, spin state marker bands between 1630-1578 $cm^{-1}$ indicate the presence of both low and high spin species for heme protein on the colloidal surfaces which is in a good agreement with the literature.[31]

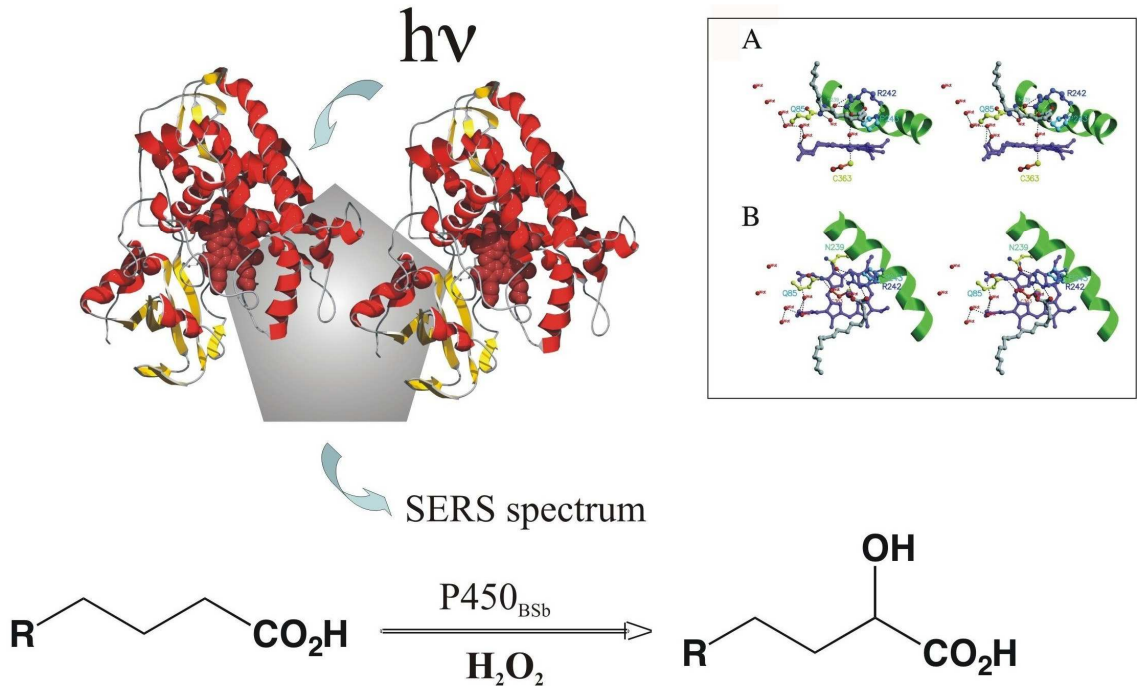


**Figure 4.3:** *The principle of SERS measurements using $P450_{BS\beta}$ adsorbed on silver colloid and the $P450_{BS\beta}$ catalysed hydroxylation of fatty acid in the presence of $H_2O_2$. The inset shows A) side and B) top view of $P450_{BS\beta}$ heme pocket and the binding of fatty acids (shown in grey). Adapted from Ref.*[35-37]

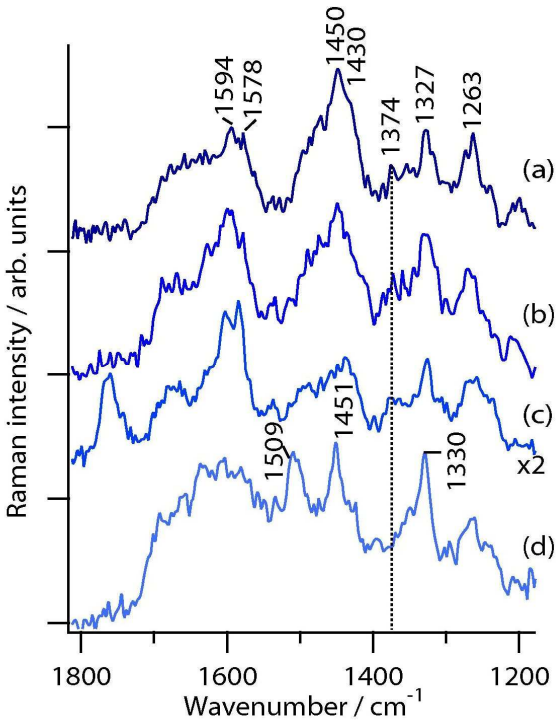


**Figure 4.4:** *SERS spectra of a) substrate-free P450$_{BS\beta}$, b) with myristic acid (MA), c) with $H_2O_2$ and d) with $H_2O_2$ + MA. SERS spectra were obtained at 530.9 nm excitation and 20s acquisition time.*

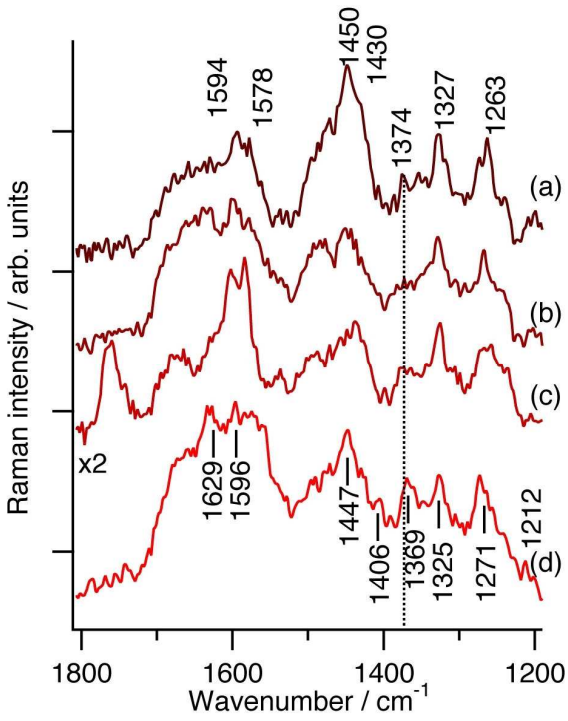


**Figure 4.5:** *SERS spectra of a) substrate-free P450BSβ, b) with hydroxylauric acid (HLA), c) with $H_2O_2$ and d) with $H_2O_2$ + HLA. SERS spectra were obtained at 530.9 nm excitation and 20s acquisition time.*

**Table 4-1:** *Selected peaks (in $cm^{-1}$) from SERS spectra of free and treated $P450_{BS\beta}$. Spectra were taken using silver colloid as a SERS surface. The concentration of the enzyme was 5 μM.*

| Substrate-free $P450_{BS\beta}$ (4.4a,4.5a) | $P450_{BS\beta}$ + $H_2O_2$ (4.4c,4.5c) | $P450_{BS\beta}$ + MA (4.4b) | $P450_{BS\beta}$ + MA + $H_2O_2$ (4.4d) | $P450_{BS\beta}$ + HLA (4.5b) | $P450_{BS\beta}$ + HLA + $H_2O_2$ (4.5d) |
|---|---|---|---|---|---|
| No* | 1760 (s) | no | no | no | no |
| No | no | 1626 (w) | 1632 (w) | 1629 (vw) | 1629 (s) |
| 1594 (s)** | 1602 (vs) | 1599 (s) | 1604 (w) | 1600 (w) | 1596 (s) |
| 1578 (w) | 1584 (s) | 1578 (w) | 1582 (w) | no | 1578 (w) |
| No | no | no | 1509 (s)*** | no | no |
| 1450 (vs) | 1450 (vw) | 1450 (s) | 1450 (vs) | 1450 (w) | 1448 (vs) |
| 1430 (sh) | 1436 (w) | 1436 (sh,w) | no | no | no |
| 1374 | 1375 (w) | 1374 (w) | 1374 | no | 1369 |
| 1327 (s) | 1327 (s) | 1327 (s) | 1330 (vs) | 1328 (w) | 1326 (s) |
| 1274 (vw) | no | 1271 (s) | no | no | 1271 (s) |
| 1263 (s) | 1261 (w) | 1263 (sh) | 1261 (w) | 1266 (w) | 1265 (sh) |
| 1209 (vw) | no | 1209 (w) | no | 1212 (vw) | 1212 (w) |
| 1165 (w) | no | 1170 (w) | 1169 (w) | no | 1175 (vw) |
| 1005 (w) | 1007 (w) | 1007 (w) | 1104 (w) | no | 1107 (w) |

*no (not observed,) vs (very strong), s (strong), w (weak), vw (very weak), sh (shoulder)

**marker modes are shown in bold

*** underlined is the new band formed due to binding of the fatty acid substrate

When myristic acid only is added to the enzyme, no significant changes in the enzyme spectrum can be observed. In contrast, when $H_2O_2$ is added to the solution a new band at 1509 $cm^{-1}$ appears and the band at 1330 $cm^{-1}$ increases indicating changes in heme coordination. This reveals that the hydroxylation reaction of myristic acid takes place in the presence of $H_2O_2$. In addition, the changes in the spectrum of the $H_2O_2$ treated enzyme (new band appears at 1760 $cm^{-1}$ and others at 1584 and 1602 $cm^{-1}$ are enhanced) can be related to changes in heme environment. Although, it has been discussed in literature[29] that the properties of Ag colloids change in the presence of peroxide due to the reduction of $Ag^+$ ions to Ag, we have added already activated enzyme to the colloid solution, avoiding a directed addition of excess peroxide. This strongly indicates that the changes originate from the coordination of peroxide to the heme moiety.

Further SERS measurements were perfomed with hydroxylauric acid (HLA), a fatty acid which is not an enzymatic substrate but rather a product of fatty acid oxidation. If HLA is added to the enzyme, without $H_2O_2$ no spectral differences in comparison to the substrate-free $P450_{BS\beta}$ can be observed. However, spectral changes, mainly the better defined appearance of a peak at 1369 $cm^{-1}$, can be detected when both $H_2O_2$ and HLA are added. In the literature the peak at 1369 $cm^{-1}$ is discussed as a marker of the heme oxidation state, indicating its ferric nature suggesting that the enzyme is present in its native (non activated) form.[31] But without better evidence this could be also attributed to variations of the enhancing substrate. Compared to the MA results the spectral changes are much less evident, suggesting that no reaction took place.

## 4.3 Materials and Methods

a) Materials

Myristic acid (MA), Hydroxylauric acid (HLA), $MgCl_2$, spermine and ascorbic acid were all obtained from Sigma-Aldrich Chemie GmbH, Germany. $H_2O_2$ was purchased from Fluka. Silver colloid was also purchased (UniSil, UK) and used as obtained. Recombinant $P450_{BS\beta}$ (CYP152A1) was expressed from E. coli M15 (pREP4) by use of plasmid pQE-30tBSb kindly donated by Dr. Isamu Matsunaga.[40] The enzyme containing a C-terminal hexahistidine tail was overexpressed in E. coli M15 and purified by affinity chromatography as reported earlier. Enzyme stock solutions of 20 μM were prepared in phosphate buffer pH 7. Prior to all measurements, the enzyme was mixed with myristic acid, hydroxylauric acid, $H_2O_2$ or the combination of both so that the final concentrations in the solution were 5 μM enzyme, 10 μM substrate (MA or HLA) and 25 μM $H_2O_2$.

b) Sample preparation

For SERS experiments, the silver colloid was firstly aggregated with NaCl (0.1 M). The sample solutions were prepared by adding the pre-aggregated silver colloid (160 μL of 200 μL final volume) to the enzyme solution. Then 20μL of the mixed liquid was placed on a glass cover slip, previously cleaned as described in section 3.3, in the sample holder and Raman spectra were recorded subsequently.

c) Instrumentation

The SERS experiments were performed using an inverted confocal Raman microscope (Jobin Yvon-Horiba LabRam invers HR) equipped with an oil immersion (N.A 1.45) objective.

All SERS spectra were excited with 530.9 nm radiation from a Krypton Ion laser (Coherent Innova I302C). The laser power at the sample was 80 μW and the acquisition time was 20 s for each measurement. All spectra shown are raw data, no further baseline-correction or smoothing procedures were applied

## 4.4 Conclusion & Outlook

We have used SERS measurements on silver colloid substrate to investigate the changes brought by fatty acid substrates interaction with $P450_{BS\beta}$ enzyme. Marker signals for $P450_{BS\beta}$ were identified and the significant changes in SERS spectra observed in the presence of myristic acid, inherent enzymatic substrate. More studies are underway using this proof of concept procedure to identify unknown enzymatic substrates and eventually enable fast screening of enzymatic activity.

## 4.5 References


[1] E. Bailo, L. Fruk, C. M. Niemeyer, V. Deckert. Surface Enhanced Raman Scattering as a Tool to Probe Cytochrome P450-Catalysed Substrate Oxidation. *Anal. Bioanal. Chem.* **2009**, *(Submitted)*.

[2] J. A. Dieringer, A. D. McFarland, N. C. Shah, D. A. Stuart, A. V. Whitney, C. R. Yonzon, M. A. Young, X. Zhang, R. P. Van Duyne. Surface enhanced Raman spectroscopy: new materials, concepts, characterization tools, and applications. *Faraday Discuss.* **2006**, *132*, 9.

[3] D. Graham, K. Faulds, W. E. Smith. Biosensing using silver nanoparticles and surface enhanced resonance Raman scattering. *Chem. Commun. (Camb)* **2006**, 4363.

[4] K. Hering, D. Cialla, K. Ackermann, T. Dorfer, R. Moller, H. Schneidewind, R. Mattheis, W. Fritzsche, P. Rosch, J. Popp. SERS: a versatile tool in chemical and biochemical diagnostics. *Anal. Bioanal. Chem.* **2008**, *390*, 113.

[5] W. E. Smith. Practical understanding and use of surface enhanced Raman scattering/surface enhanced resonance Raman scattering in chemical and biological analysis. *Chem. Soc. Rev.* **2008**, *37*, 955.

[6] D. A. Stuart, A. J. Haes, C. R. Yonzon, E. M. Hicks, R. P. Van Duyne. Biological applications of localised surface plasmonic phenomenae. *IEE Proc. Nanobiotechnol.* **2005**, *152*, 13.

[7] K. K. Hering, R. Moller, W. Fritzsche, J. Popp. Microarray-based detection of dye-labeled DNA by SERRS using particles formed by enzymatic silver deposition. *Chemphyschem* **2008**, *9*, 867.

[8] L. Fruk, A. Grondin, W. E. Smith, D. Graham. A new approach to oligonucleotide labelling using Diels-Alder cycloadditions and detection by SERRS. *Chem. Commun. (Camb)* **2002**, 2100.

[9] K. Faulds, L. Fruk, D. C. Robson, D. G. Thompson, A. Enright, W. E. Smith, D. Graham. A new approach for DNA detection by SERRS. *Faraday Discuss.* **2006**, *132*, 261.

[10] I. Chourpa, F. H. Lei, P. Dubois, M. Manfait, G. D. Sockalingum. Intracellular applications of analytical SERS spectroscopy and multispectral imaging. *Chem. Soc. Rev.* **2008**, *37*, 993.

[11] M. Y. Sha, H. Xu, S. G. Penn, R. Cromer. SERS nanoparticles: a new optical detection modality for cancer diagnosis. *Nanomed* **2007**, *2*, 725.

[12] R. F. Aroca, R. A. Alvarez-Puebla, N. Pieczonka, S. Sanchez-Cortez, J. V. Garcia-Ramos. Surface-enhanced Raman scattering on colloidal nanostructures. *Adv. Colloid Interface Sci.* **2005**, *116*, 45.

[13] P. Hildebrandt, M. Stockburger. Surface-enhanced resonance Raman spectroscopy of Rhodamine 6G adsorbed on colloidal silver. *J. Phys. Chem.* **1984**, *88*, 5935.

[14] P. C. Lee, D. Meisel. Adsorption and surface-enhanced Raman of dyes on silver and gold sols. *J. Phys. Chem.* **1982**, *86*, 3391.

[15] R. M. Stöckle, V. Deckert, C. Fokas, R. Zenobi. Controlled Formation of Isolated Silver Islands for Surface-Enhanced Raman Scattering. *Appl. Spectrosc.* **2000**, *54*, 1577.

[16] Q. Yu, P. Guan, D. Qin, G. Golden, P. M. Wallace. Inverted Size-Dependence of Surface-Enhanced Raman Scattering on Gold Nanohole and Nanodisk Arrays. *Nano Lett.* **2008**, *8*, 1923.

[17] L. Lu, I. Randjelovic, R. Capek, N. Gaponik, J. Yang, H. Zhang, A. Eychmuller. Controlled Fabrication of Gold-Coated 3D Ordered Colloidal Crystal Films and Their Application in Surface-Enhanced Raman Spectroscopy. *Chem. Mater.* **2005**, *17*, 5731.

[18] E. Vogel, W. Kiefer, V. Deckert , D. Zeisel. Laser-deposited silver island films: an investigation of their structure, optical properties and SERS activity. *J. Raman Spectrosc* **1998**, *29*, 693.

[19] X. X. Han, Y. Kitahama, Y. Tanaka, J. Guo, W. Q. Xu, B. Zhao, Y. Ozaki. Simplified Protocol for Detection of Protein-Ligand Interactions via Surface-Enhanced Resonance Raman Scattering and Surface-Enhanced Fluorescence. *Anal. Chem.* **2008**, *80*, 6567.

[20] A. Ingram, L. Byers, K. Faulds, B. D. Moore, D. Graham. SERRS-based enzymatic probes for the detection of protease activity. *J. Am. Chem. Soc.* **2008**, *130*, 11846.

[21] A. M. Ingram, K. Stirling, K. Faulds, B. D. Moore, D. Graham. Investigation of enzyme activity by SERRS using poly-functionalised benzotriazole derivatives as enzyme substrates. *Org. Biomol. Chem.* **2006**, *4*, 2869.

[22] B. D. Moore, L. Stevenson, A. Watt, S. Flitsch, N. J. Turner, C. Cassidy, D. Graham. Rapid and ultra-sensitive determination of enzyme activities using surface-enhanced resonance Raman scattering. *Nat. Biotechnol.* **2004**, *22*, 1133.

[23] H. B. Dunford, *Heme Peroxidases*, Wiley, New York, **1999**.

[24] B. Meunier, S. P. de Visser, S. Shaik. Mechanism of oxidation reactions catalyzed by cytochrome p450 enzymes. *Chem. Rev.* **2004**, *104*, 3947.

[25] R. Bernhardt. Cytochromes P450 as versatile biocatalysts. . *J Biotechnol* **2006**, *124*.

[26] K. S. Rabe, Gandubert, V. J., Spengler, M., Erkelenz, M., Niemeyer, C. M. . Engineering and assaying of cytochrome P450 biocatalysts. . *Anal. Bioanal. Chem.* **2008**, *392*.

[27] F. P. Guengerich. Cytochrome P450 enzymes in the generation of commercial products. . *Nat. Rev. Drug. Discov.* **2002**, *1*, 359.

[28] A. W. Munro, H. M. Girvan, K. J. McLean. Variations on a (t)heme—novel mechanisms, redox partners and catalytic functions in the cytochrome P450 superfamily. *Nat. Prod. Rep.* **2007**, *24*, 585

[29] E. J. Bjerneld, K. V. Murty, J. Prikulis, M. Kall. Laser-induced growth of Ag nanoparticles from aqueous solutions. *Chemphyschem* **2002**, *3*, 116.

[30] A. Feis, M. P. Marzocchi, M. Paoli, G. Smulevich. Spin state and axial ligand bonding in the hydroxide complexes of metmyoglobin, methemoglobin, and horseradish peroxidase at room and low temperatures. *Biochemistry* **1994**, *33*, 4577.

[31] I. D. G. Macdonald, A. W. Munro, W. E. Smith. FAtty Acid Indused Alteration of the Porphyrin Macrocycle of Cytochrome p450BM3. *Biophys. J.* **1998**, *74*, 3241.

[32] D. H. Murgida, P. Hildebrandt. Electron-transfer processes of cytochrome C at interfaces. New insights by surface-enhanced resonance Raman spectroscopy. *Acc. Chem. Res.* **2004**, *37*, 854.

[33] V. J. Gandubert, Torres, E., Niemeyer, C. M. . Investigation of cytochrome P450-modified cadmium sulfide quantum dots as photocatalysts. . *J. Mater. Chem.* **2008**, *18*, 3824.

[34] I. Matsunaga, T. Sumimoto, A. Ueda, E. Kusunose, K. Ichihara. Fatty acid-specific, regiospecific, and stereospecific hydroxylation by cytochrome P450 (CYP152B1) from Sphingomonas paucimobilis: Substrate structure required for α-hydroxylation. *Lipids* **2000**, *35*, 365.

[35] D. C. Haines, D. R. Tomchick, M. Machius, J. A. Peterson. Pivotal Role of Water in the Mechanism of P450BM-3. *Biochemistry* **2001**, *40*, 13456.

[36] D.-S. Lee, A. Yamada, H. Sugimoto, I. Matsunaga, H. Ogura, K. Ichihara, S.-i. Adachi, S.-Y. Park, Y. Shiro. Substrate Recognition and Molecular Mechanism of Fatty Acid Hydroxylation by Cytochrome P450 from Bacillus subtilis. CRYSTALLOGRAPHIC, SPECTROSCOPIC, AND MUTATIONAL STUDIES. *J. Biol. Chem.* **2003**, *278*, 9761.

[37] B. Meunier. *Chem. Rev.* **1992** *92* 1411.

[38] D. G. M. Iain, W. E. Smith, W. M. Andrew. Inhibitor/fatty acid interactions with cytochrome P-450 BM3. *FEBS letters* **1996**, *396*, 196.

[39] I. D. G. Macdonald, W. E. Smith. Orientation of Cytochrome c Adsorbed on a Citrate-Reduced Silver Colloid Surface. *Langmuir* **1996**, *12*, 706.

[40] I. Matsunaga, A. Ueda, T. Sumimoto, K. Ichihara, M. Ayata, H. Ogura. Site-Directed Mutagenesis of the Putative Distal Helix of Peroxygenase Cytochrome P450*1. *Arch. Biochem. Biophys.* **2001**, *394*, 45.

# Chapter 5

# TERS inside a Malaria Infected Human Red Blood Cell[1]

After the eradication of malaria from North America and from most of Europe during the first half of the 20th century, only 3 of 1.223 new drugs developed between 1975-1996 were antimalarial.[2] Industry also lost its interest in the development of insecticides for public health use and overall support for research on malaria declined.[3] During this time, Malaria became a disease of poverty and underdeveloped countries. Nowadays, there are approximately 515 million cases of malaria, in parts of the Americas, Asia, and Africa, killing between one and three million people *every year*, with the majority being young children in Sub-Saharan Africa.[4]

Malaria is caused in humans by infection of two species of parasites: *Plasmodium falciparum* and *Plasmodium vivax*, better known as malaria parasites. Malaria parasites (sporozoites) are injected into the human body by female Anopheles mosquitoes and travel to the liver (see Figure 5.1, Life cycle of the malaria parasite).[5] Inside the liver cells, each sporozoite develops into tens of thousands of mezoites. Then, the rupture of the liver cell releases the merozoites which can each penetrate and invade a red blood cell (RBC), leading to disease.[6] During the erythrocytic stage

of the Plasmodium falciparum life cycle the parasite catabolizes hemoglobin, breaking it down into free heme, which is normally toxic to the parasite organism.[7-10] The malaria parasite has evolved a detoxification pathway to remove toxic free heme. This process first involves an oxidation of ferrous-protoporphyrin IX (Fe(II)PPIX) to ferric-protoporphyrin IX hydroxide (Fe(III)PPIX-OH), known as hematin, followed by aggregation into the insoluble pigment known as hemozoin. Hemozoin is spectroscopically identical to its synthetic analogue ß-hematin, which is known to be an array of dimers linked through reciprocal iron-carboxylate bonds to one of the propionate side chains of adjacent heme moieties. This detoxification pathway is the primary target of many anti-malarial drugs on the market. For socio-economic reasons, the main treatment of malaria has been with derivatives of quinine (such as chloroquine) and sulfadoxine-pyrimethamine. Recently, resistance to some of these most-potent drugs has been climbing, increasing the dire need for effective ways to screen for potential antimalarials. In this chapter, we show the developing of a TERS approach to determine drug binding sites on hemozoin crystals. Hitherto, there are no spectroscopic methods to detect drug-binding to the hemozoin surface because nanoscale lateral resolution cannot be achieved with conventional spectroscopic technologies.

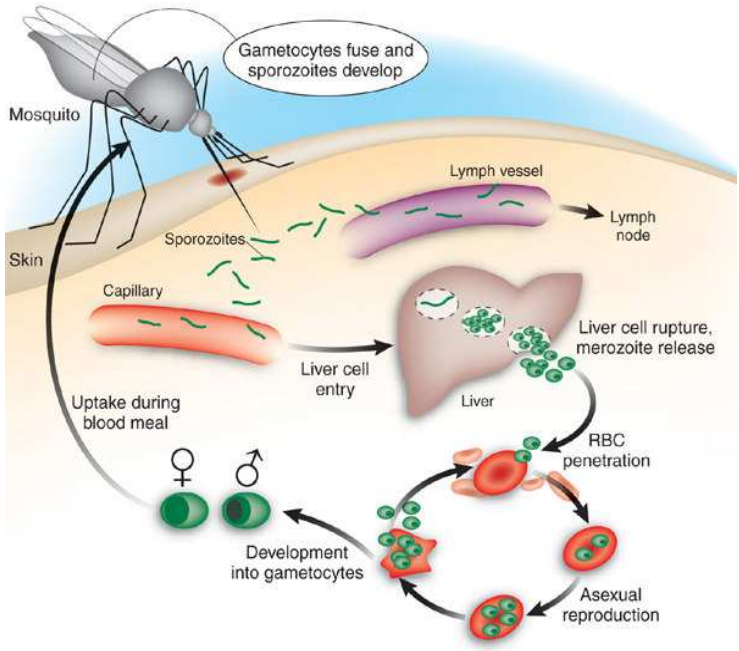


**Figure 5.1:** *Life cycle of the malaria parasite. From Ref.*[5]

## 5.1 Sectioned malaria infected human red blood cells

To perform an intracellular TERS experiment, the red blood cells should be fixed and sectioned with a special procedure that preserved the structural integrity of the cells internal matrix, minimizes intrinsic fluorescence from the sample, and is thin enough to enable laser light to pass through the cell and interact with the tip (see sample preparation in section **Fehler! Verweisquelle konnte nicht gefunden werden.**).

Figure 5.2 (a-c) depicts a series of AFM images recorded of sectioned malaria infected erythrocytes. The AFM images show an expanded progression of increasing spatial resolution from a population of cells (a), then to a single infected cell (b), and finally resolving single crystals of hemozoin in the food vacuole of the parasite (c). These are the first AFM images recorded inside the food vacuole of a malaria infected cell and appear to resolve single crystals of hemozoin.

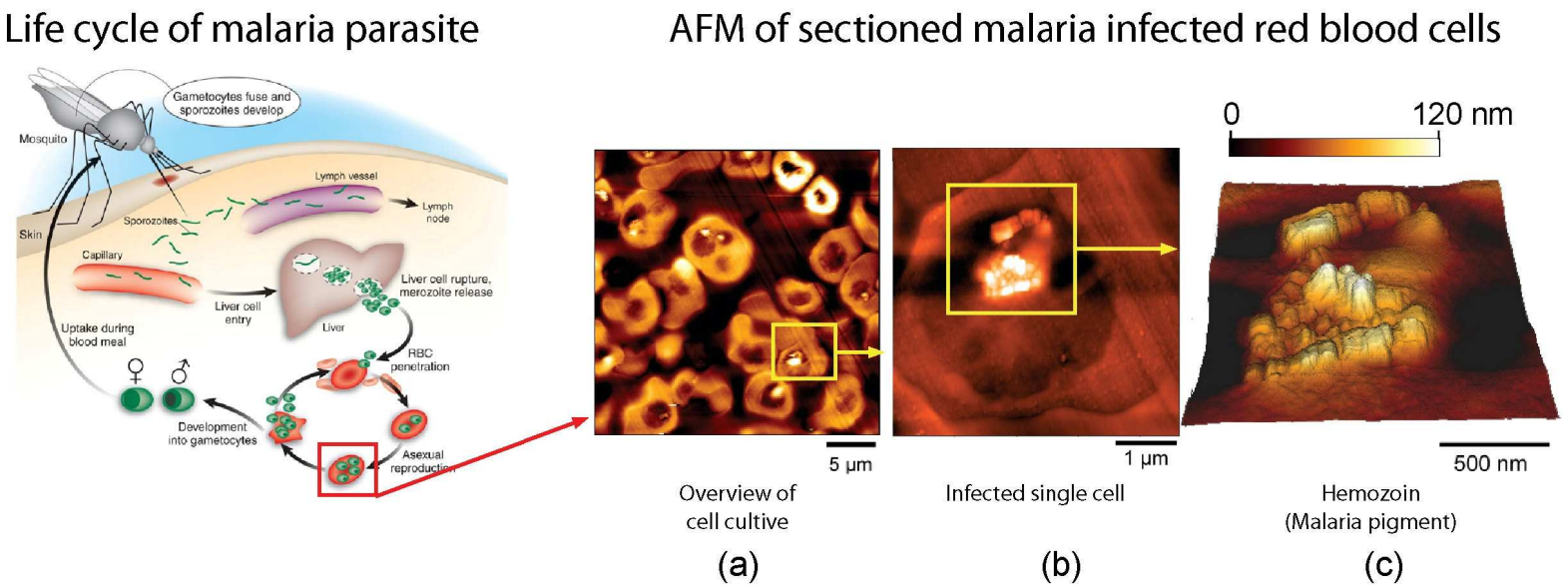


**Figure 5.2:** *(a, b, c) AFM images recorded of sectioned cells prior to TERS acquisition. (a) 30 × 30 µm AFM image recorded of a population of infected red blood cells showing a potential cell target highlighted by the blue square. (b) A high-resolution image of the cell highlighted in (a) showing hemozoin crystals aligned in the digestive vacuole. (c) An even higher resolution AFM image of the digestive vacuole of the parasite showing single crystals of hemozoin that can be selectively targeted with the TERS active tip. From Ref.* [1]

## 5.2 TERS fingerprint of malaria infected red blood cells (RBCs)

The edge of a single hemozoin crystal was selectively targeted with the nano-tip and a spectrum was recorded with the tip in the near field (Figure 5.3.a) and then retracted 7 microns from the sample (Figure 5.3.b). The spectrum shows a number of characteristic bands that are enhanced in the 1600-1500 $cm^{-1}$ region and another strong band enhanced at 1373 $cm^{-1}$. Bands in the 1650-1500 $cm^{-1}$ region are from porphyrin skeletal vibrations of the heme macrocycle, while the band at 1373 $cm^{-1}$ is assigned, in Table 5-1, to a totally symmetric pyrrole-ring breathing vibration ($\nu_4$) known as the "oxidation state marker band" because of its sensitivity to oxidation state of the central iron atom within the heme.[11-13] The position of this band is consistent with the Fe atom being in the ferric high spin state.[12, 13] These bands also appear enhanced in the corresponding SERS spectrum of β-hematin (Figure 5.3.c), which is a synthetic spectroscopically identical analogue to hemozoin.[14, 15] Synchrotron powder diffraction analysis found it to be composed of a hydrogen bonded array of heme dimers linked through reciprocal carboxylate groups.[16] Because of its structural similarity, it makes an ideal model to investigate and compare the spectral properties of hemozoin. The resonance Raman spectrum of hemozoin recorded at 532 nm is presented in Figure 5.3.d. The spectrum further corroborates the TERS spectrum, showing a similar spectral profile in terms of band position, although the relative enhancement of the bands is somewhat different and some band shifts are observed. This is frequently observed when comparing TERS spectra with conventional resonant Raman spectra because the vibrational selection rules between the techniques are different. Interestingly the TERS and SERS spectra of hemozoin and β-hematin have a spectral profile similar to measurements performed on the same compounds using near-IR excitation wavelengths (780 and 830 nm) all showing the dramatic enhancement of $\nu_4$.[15] The enhancement of $\nu_4$ when applying near-infrared excitation was explained by excitonic interactions between dimeric heme groups in the extended hydrogen bonded array.[15]

**Table 5-1:** *Assignments of TERS spectrum of a Hemozoin crystal (in $cm^{-1}$). From Ref. [1]*

| β-Hm | Hz TERS | enh | β-Hm SERS | enh | Assignment | Symmetry | Local coordinates |
|---|---|---|---|---|---|---|---|
| 1629 | 1627 | 1 | 1616 | 9 | $\nu_{10}$ | $B_{1g}$ | $\nu$ $(C_\alpha Cm)_{as}$ |
| 1619 | | | " | | | | $\nu$ (C=C)vinyl |
| 1589 | 1608 | 3 | 1581 | 2 | $\nu_{37}$ | $E_u$ | $\nu$ $(C_\alpha C_m)_{as}$ |
| 1570 | 1564 | 6 | 1564 | 6 | $\nu_{19}$ | $A_{2g}$ | $\nu$ $(C_\alpha C_m)_{as}$ |
| " | " | | " | | $\nu_2$ | $A_{1g}$ | $\nu$ $(C_\beta C_\beta)$ |
| 1549 | | | | | $\nu_{11}$ | $B_{1g}$ | $\nu$ $(C_\beta C_\beta)$ |
| 1526 | 1523 | 2 | | | $\nu_{38}$ | $E_u$ | $\nu$ $(C_\beta C_\beta)$ |
| 1492 | | | 1489 | 1 | $\nu_3$ | $A_{1g}$ | $\nu$ $(C_\alpha C_m)_{sym}$ |
| 1460 | 1457 | 2 | 1452 | 1 | $\nu_{28}$ | $B_{2g}$ | $\nu$ $(C_\alpha C_m)_{sym}$ |
| 1431 | 1431 | | 1430 | 1 | | | $\delta$ $(=C_bH_2)_{sym}$ (1) |
| | | | | | | | $COO^-$ ? |
| 1401 | | | 1394 | 2 | $\nu_{29}$ | $B_{2g}$ | $\nu$ (pyr quarter-ring) |
| " | | | " | | $\nu_{20}$ | $A_{2g}$ | $\nu$ (pyr quarter-ring) |
| 1373 | 1373 | 10 | 1369 | 10 | $\nu_4$ | $A_{1g}$ | $\nu$ $(\text{pyr half-ring})_{sym}$ |
| 1342 | | | | | $\nu_{41}$ | $E_u$ | $\nu$ $(\text{pyr half-ring})_{sym}$ |
| " | | | | | | | $\delta$ $(=C_bH_2)_{sym}$ (2) |
| 1306 | 1310 | 2 | 1311 | 1 | $\nu_{21}$ | $A_{2g}$ | $\delta$ $(C_mH)$ |
| " | | | | | | | $\delta$ $(C_aH=)$ |
| 1279 | | | 1277 | | | | prop $\delta$ $(CH_2)$ wag |
| - | 1248 | 1 | 1236 | 1 | ? | | Amide III? |
| 1237 | | | | | $\nu_{13}$ | $B_{1g}$ | $\delta$ $(C_mH)$ |
| 1222 | 1198 | 1 | | | | | prop $\delta$ $(CH_2)$ twisting |
| 1169 | 1170 | 1 | 1176 | 1 | $\nu_{30}$ | $B_{2g}$ | $\nu$ $(\text{pyr half-ring})_{as}$ |
| 1148 | 1135 | 1 | 1133 | 3 | $\nu_{14}$ | $B_{1g}$ | $\nu$ $(C_\beta C_1)$sym |
| 1125 | | | | | $\nu_6 + \nu_8$ | $A_{1g}$ | $\nu$ $(C_\alpha\text{-}C_\beta)_{sym}$ + $\nu$ (Fe-N) |
| " | | | 1107 | 1 | $\nu_{22}$ | $A_{2g}$ | $\nu$ $(\text{pyr half-ring})_{as}$ |
| 1087 | | | | | | | $\delta$ $(=C_bH_2)_{as}$ (1) |
| 1056 | 1063 | 1 | 1046 | | | | $\delta$ $(=C_bH_2)_{as}$ (2) |
| 1003 | | | 1014 | 1 | | | $\gamma(C_aH=)$ |
| " | | | " | | $\nu_{45}$ | $E_u$ | $\nu$ $(C_\beta C_1)_{as}$ |
| 975 | 967 | 1 | 963 | 2 | | | $\nu$ (Cc-Cd) |
| " | | | | | $\nu_{32} + \nu_{35}$ | $A_{1g}$ | $\delta$ (porph def) + $\delta$ (pyr |
| 939 | 940 | 1 | 944 | | $\nu_{46}$ | $E_u$ | $\delta$ $(\text{pyr def})_{as}$ |
| 920 | | | 925 | | | | $\gamma$ $(=C_bH_2)_{sym}$ |
| 875 | 879 | | | | ? | | ? |

(cont.)

| β-Hm | Hz TERS | enh | β-Hm SERS | enh | Assignment | Symmetry | Local coordinates |
|---|---|---|---|---|---|---|---|
| 850 | | | 836 | | $\gamma_{19}$ | $E_g$ | γ ($C_mH$) |
| 822 | | | 799 | 1 | $\gamma_{10}$ | $B_{1u}$ | γ ($C_mH$) |
| 790 | 791 | 1 | 773 | 1 | $\nu_{32}$ | $B_{2g}$ | δ (pyr def)$_{as}$ |
| 754 | | | 758 | 3 | $\nu_{15}$ | $B_{1g}$ | ν (pyr breathing) |
| 724 | 729 | | | | $\gamma_5$ | $A_{2u}$ | δ (pyr fold)$_{sym}$ |
| 712 | 712 | | | | $\gamma_{11}$ | $B_{1u}$ | δ (pyr fold)$_{as}$ |
| 692 | | | | | $\gamma_{15}$ | $B_{2u}$ | δ (pyr fold)$_{sym}$ |
| 677 | 679 | 1 | | | $\nu_7$ | $A_{1g}$ | δ (pyr def)$_{sym}$ |
| | 641 | | | | | | ? |
| 631 | | | | | ? | | δ (pyr def)$_{sym}$? |
| 608, 580 | 574 | | | | $\nu_{48}$ | $E_u$ | δ (pyr def)$_{sym}$ |
| - | | | | | | | ν (Fe-$O_2$) |
| 553 | | | | | $\gamma_{21}$ | $E_g$ | δ (pyr fold)$_{sym}$ |
| | 521 | | | | | | Si (AFM tip) |
| 508 | | | | | $\gamma_{12}$ | $E_g$ | δ (pyr swivel) |
| 487 | | | | | $\nu_{33}$ | $B_{2g}$ | δ (pyr rot) |
| | | | | | | | ? |
| 435, | | | | | | | δ ($C_\beta C_a C_b$) + δ ($C_\beta$Me) |
| - | | | | | | | δ (Fe-O-O) |
| 373 | | | | | | | δ ($C_\beta C_c C_d$) |
| 347 | | | | | $\nu_8$ | $A_{1g}$ | ν (Fe-N) |

*Abbreviations:* enh =relative enhancement graded as very weak = 1-2, weak =3-4 medium = 5-6, strong =7-8 and very strong = 9-10, TERS = tip enhanced Raman spectrum, SERS = surface enhanced Raman spectrum, Hz = hemozoin, β-hm = β-hematin, ν = in-plane stretch, γ = out-of-plane vibration, δ = deformation mode, pyr = pyrrole.

Labelling and notation scheme is based on the work of M. Abe et al.[11]

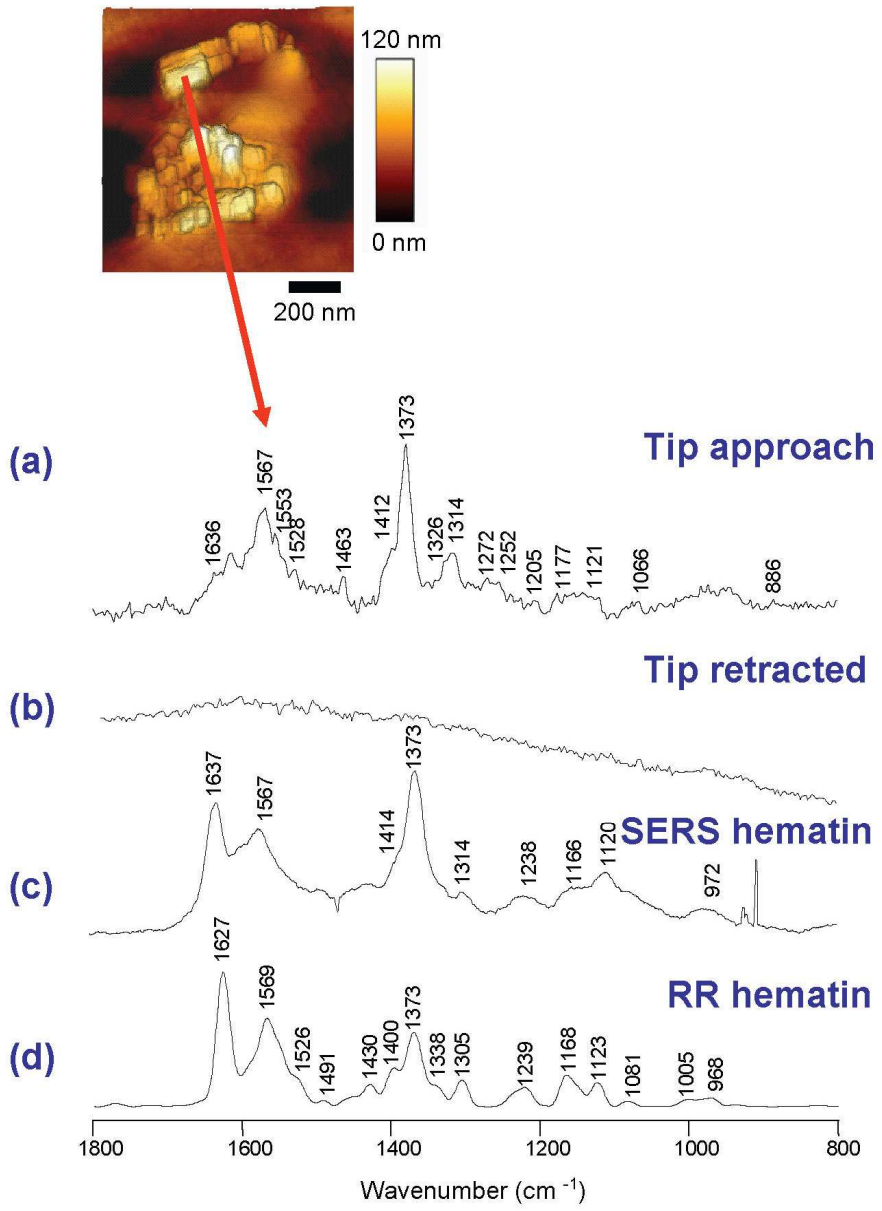


**Figure 5.3:** *(a) TER spectrum recorded of the edge of a hemozoin crystal at 20 nm spatial resolution. The spectrum was recorded with a laser power of 600 µW and exposure time of 5 seconds. (b) After recording a spectrum the tip was retracted by several microns and a further spectrum recorded to ensure the tip had not been contaminated by the sample. (c) Surface enhanced Raman spectrum recorded of β-hematin prepared using SERS active Ag-particles. Spectra were recorded using a 532 nm laser and 10 second acquisition time. (d) Resonance Raman spectrum of β-hematin recorded at 532 nm with a 10 second acquisition time. From Ref.* [1]

Recent studies show that quinoline based drugs that bind to hemozoin and β-hematin reduce the intensity of this band[17, 18] and cause distinct shifts in the UV spectra indicative of excitonic interactions.[19] The intensity decrease of $\nu_4$ is thought to result from the quinolines binding to the hemozoin via strong $\pi \leftarrow \pi$ interactions causing a reduction in excitonic interactions between neighboring hemes.[17] TER spectra of sectioned trophozoites inoculated with chloroquine (CQ) produced very poor signal-to-noise spectra. Binding of CQ to hemozoin may disrupt the heme array at the surface of the crystal and consequently impeding the surface plasmons and/or surface excitons generated by the interaction between the TERS active tip and the highly ordered heme structure of hemozoin.

Spectral fluctuations and Raman shifts are inherent with this technology because of its extreme sensitivity and the subtle molecular changes that occur at nanometer resolution.[20, 21] These spectral fluctuations can be attributed to the molecular orientation under the TERS tip, which can change the adsorption angle and the angle of the incident polarization.[20] While Raman band shifts are thought to result from molecular deformations caused by the silver atoms coated on the tip.[21] Spectral fluctuations provide indirect evidence for single molecule detection and indeed some recent papers claim single molecule TERS.[21-24] To investigate spectral fluctuations we performed Principal Component Analysis (PCA) on all TER hemozoin spectra that exhibited a good signal-to-noise ratio. PCA was also used to investigate TER spectra of isolated hemoglobin, which served as a model compound. The PCA technique enables one to visualize the intrinsic variance in the data set and is often used to resolve “hidden patterns”.[25] The PCA results (Figure 5.4 ) for TER spectra recorded of intracellular hemozoin indicate there are two main types of spectra accounting for the strong loadings of the first and second principal components. The PC1 loadings plot of TER hemozoin spectra confirmed that the bands most often enhanced in the TER spectra were from the heme moiety. These bands include the oxidation state marker band at 1373 $cm^{-1}$ and other porphyrin skeletal and ring breathing modes at 1611, 1591, 1571, 1550, 1423, 1311, 1243, 996 and 971 $cm^{-1}$. The PC2 loadings indicate some low wavenumber bands possibly associated with pyrrole half-ring and quarter-ring vibrations explain the separation of spectra along PC2.

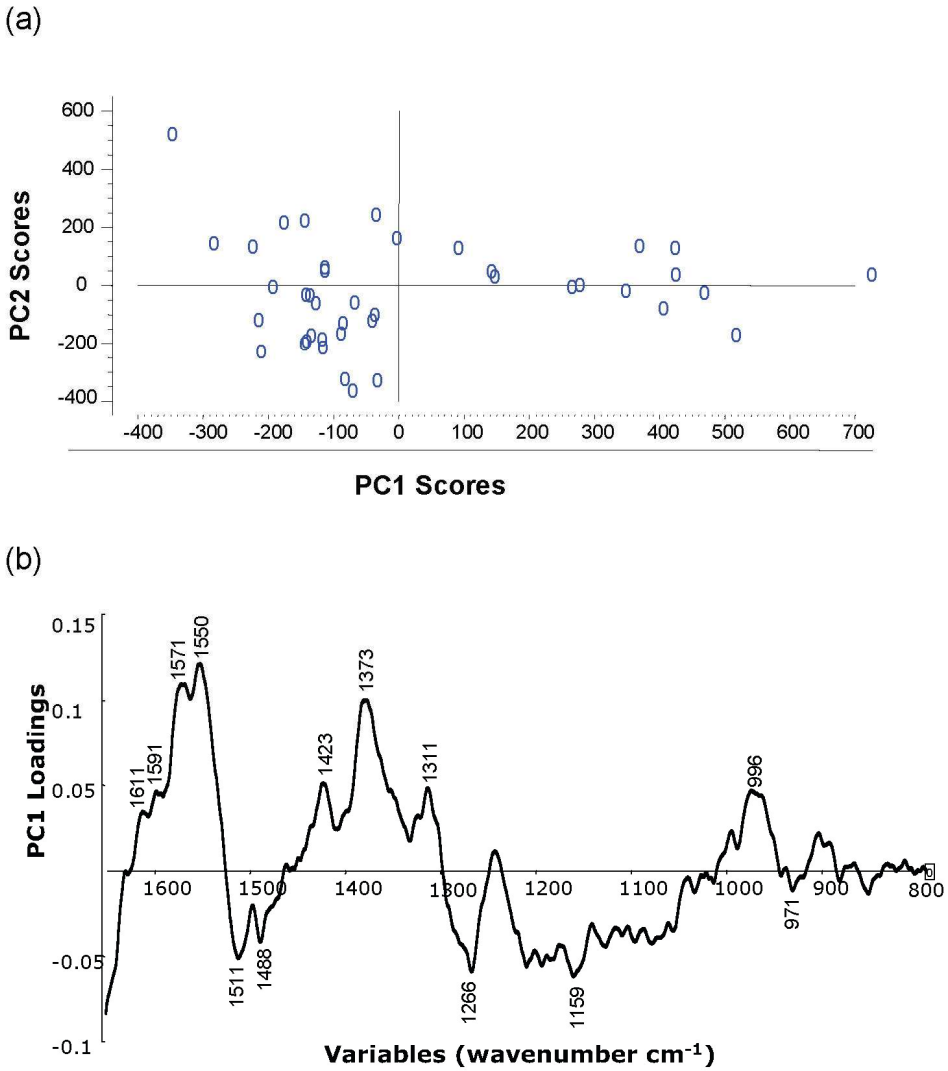


**Figure 5.4:** *(a) Principal Component Analysis (PCA) scores plot showing individual TER spectra recorded of hemozoin from a number of single crystals using two different tips. The data was pre-processed using extended multiplicative scatter correction and a leverage corrected PCA analysis performed on mean centered data using Unscrambler (CAMO, Norway). The PCA scores plot shows a spread of TER spectra (O) along PC1 (32 % explained variance) and PC2 (15 % explained variance). (b) PC1 loadings plot showing which variables (wavenumber values) are important in explaining the variance observed along PC1. Strong positive and negative loadings are the most important in influencing the model. The strong loadings correlate well with the major porphyrin vibrational modes observed in the TERS, SERS and resonance Raman spectra of hemozoin. From Ref.* [1]

Analysis of hemoglobin with TERS revealed three main types of spectra (Figure 5.5). In the top TERS spectrum (type 1), the porphyrin vibrations including the oxidation state marker bands at 1378 and 1355 $cm^{-1}$ from ferric and ferrous hemes along with other porphyrin skeletal modes at 1639, 1545, 1433, 1403, 1195 and 660 $cm^{-1}$ are observed. It is interesting to note that the technique shows two oxidation state marker bands indicating nano-scale oxidation changes possibly induced by the laser. In the bottom TERS spectrum (type 2) other bands including some proteinacious bands such as the amide I (1656 $cm^{-1}$), amide III (1321 $cm^{-1}$), carboxylate band from terminal amino acid side chains (1400 $cm^{-1}$) and also heme bands at 1587, 1560, 1155, 908, 754 and 671 $cm^{-1}$ are pronounced. The type 3 spectrum shows two amino acid bands enhanced namely the phenylalanine mode at 1002 $cm^{-1}$ and the histidine mode at 932 $cm^{-1}$ along with the amide I, amide III and other heme bands. The TERS spectra of amino acid bands have been previously been reported for cytochrome c [26] but no amide I mode was observed enhanced in that study. The PCA results support these findings is shown in Figure 5.6, showing the PC1 loadings mainly dominated by heme bands, whilst the PC2 loadings plot show strong loadings associated with protein. The PC3 loadings showed the presence of heme and protein modes along with the phenylalanine mode at 1002 $cm^{-1}$. The proteinacious bands are normally observed only in the infrared spectrum and near-IR excited Raman spectra of hemoglobin[27] but not the resonance Raman spectrum of hemoglobin at least at 530 nm.[28] The results corroborate the finding by Yao et al.[26] who observed similar types of spectra for cytochrome c where one type was dominated by heme bands and the other showed amino acid bands enhanced. The variation was explained by the proximity of the tip in relation to the heme and amino acids, respectively.[26] If the tip is in close proximity to the heme then the heme modes will become enhanced or alternatively if the tip is in close proximity to the amino acids then these modes will be enhanced.

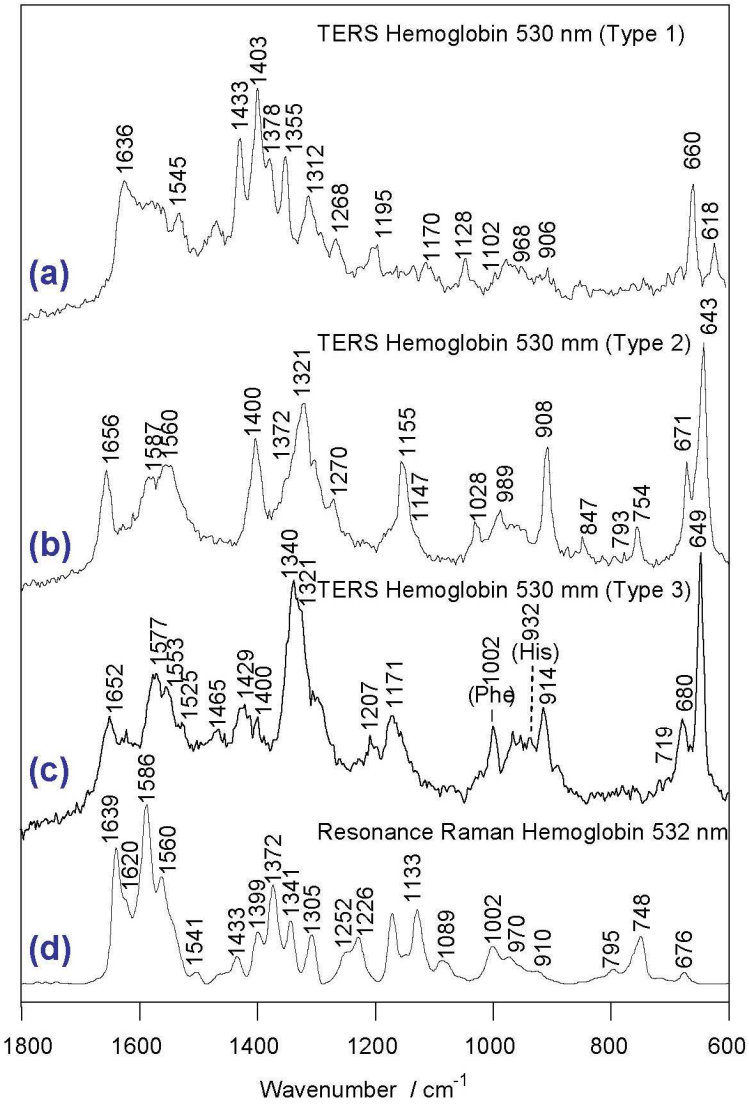


**Figure 5.5:** *Representative TERS spectra of purified hemoglobin showing the three most common types of spectra observed. (a) The most common TERS spectrum observed was dominated by intense bands in the pyrrole ring breathing region between 1450-1300 cm$^{-1}$ and other specific heme vibrations. (b) The second most common spectrum had characteristic protein bands including amide I (1656 cm$^{-1}$), amide III (1321 cm$^{-1}$) and the carboxylate band from terminal amino acid side chains (1400 cm$^{-1}$). (c) Type 3 TERS spectrum of hemeoglobin with phenylalanine and histidine modes labeled. (d) Resonance Raman spectrum of single hemoglobin crystals recorded using a 532 nm laser line with 10 seconds laser exposure at 600 µW. From Ref.* [1]

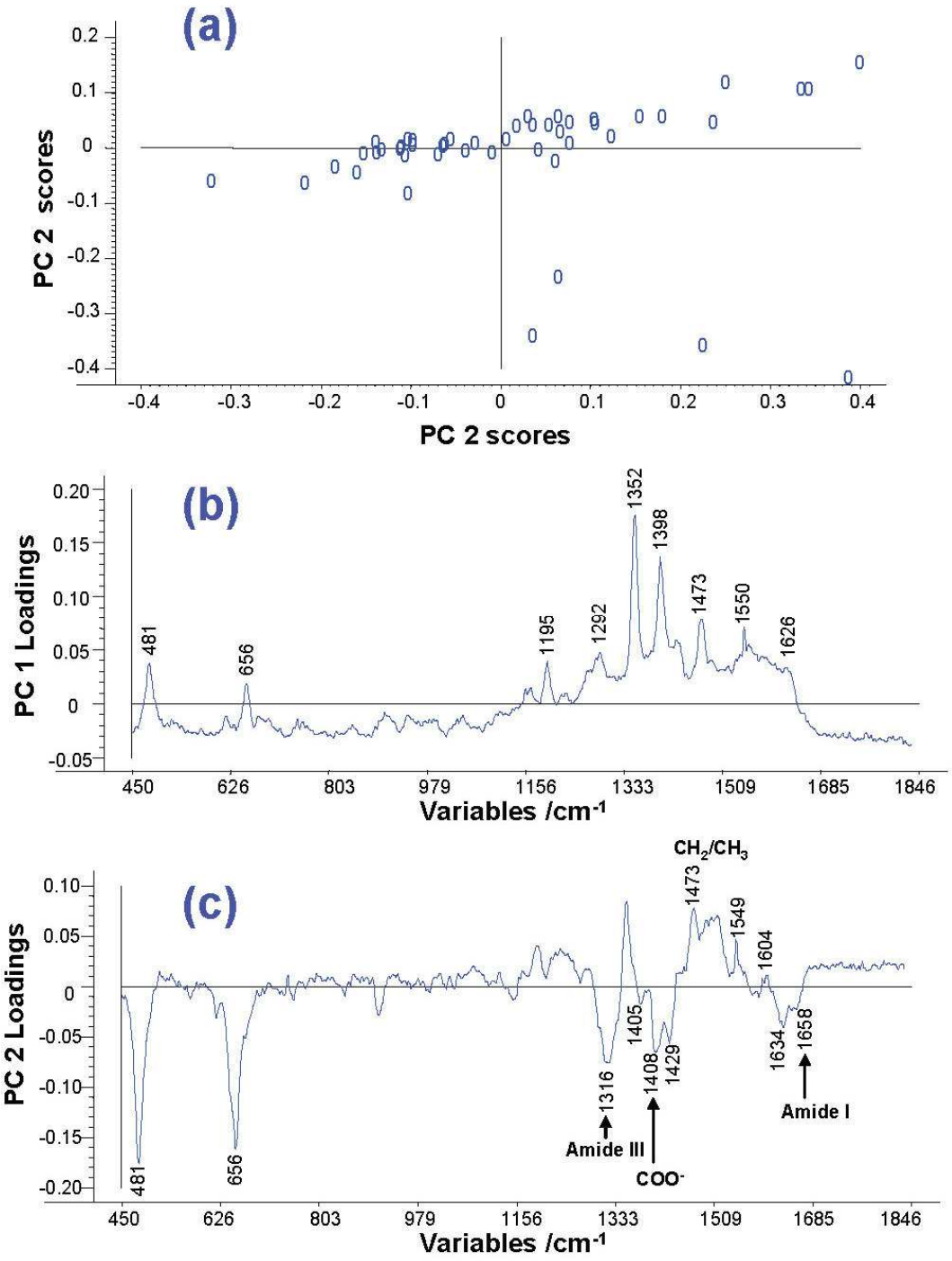
(a)
PC 2 scores
PC 2 scores
(b)
PC 1 Loadings
481
656
1195
1292
1352
1398
1473
1550
1626
Variables /cm-1
(c)
PC 2 Loadings
CH2/CH3
1473
1549
1604
1658
1634
1405
1408
1429
1316
481
656
Amide III
COO-
Amide I
Variables /cm-1

(cont.)

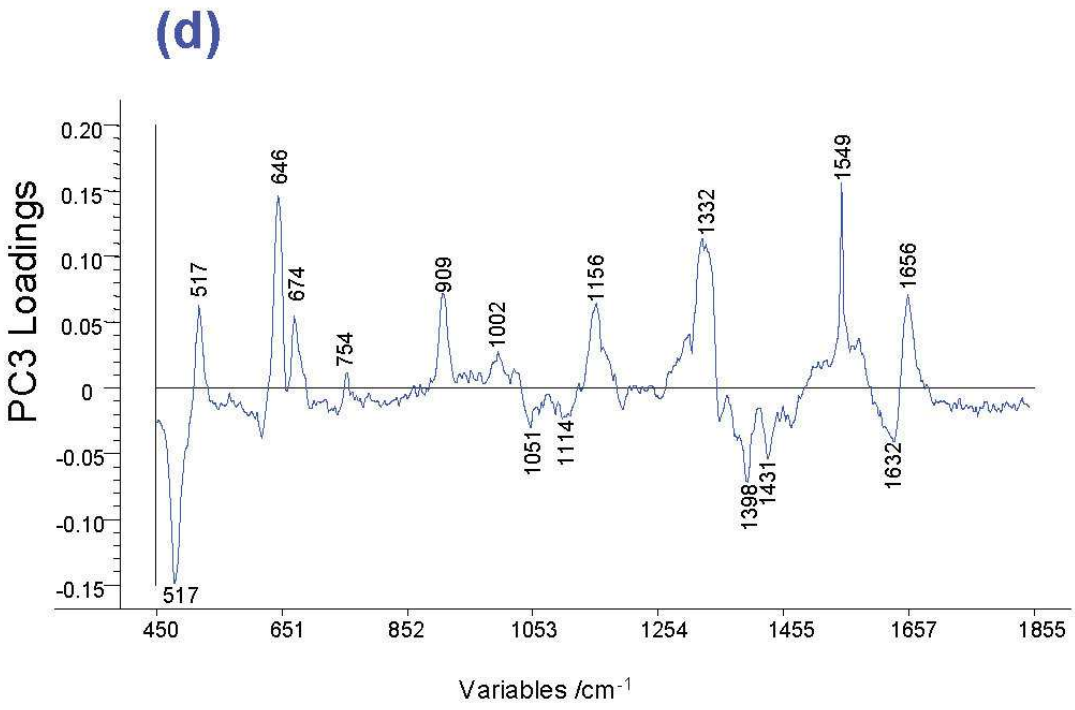


**Figure 5.6:** *(a) PCA scores plot of hemoglobin TERS spectra (o) plotted against PC1 and PC2. There is a significant spread of the data across both PC1 and PC2. (b) The PC1 loadings show that the important variables in explaining the variance are mainly from the heme moiety and correspond to the type 1 spectrum presented in Figure 4. (c) The PC2 loadings plot shows some proteinacious bands including the amide I at 1656 $cm^{-1}$ and amide III modes, carboxylate band ($COO^-$) are significant in explaining the variance across PC2 and correlate closely with the type 2 spectrum presented in Figure 4. (d) PC3 loadings showing the phenylalanine band 1002 $cm^{-1}$ contributing to the explained variance of this PC along with the amide I mode and other heme modes. From Ref.* [1]

## 5.3 Materials and Methods

### Tip-enhanced Raman Scattering

a) Sample preparation

P. falciparum (D10 strain) was maintained in continuous culture using human erythrocytes obtained from the Red Cross Blood Bank, Melbourne.[29] Parasitized erythrocytes were cultured in complete culture medium (CCM) consisting of RPMI 1640 (GIBCO BRL), 25 mM hydroxypiperazine-N`-2-ethane sulfonic acid (HEPES, Sigma pH 7.4), 2 g/L sodium bicarbonate (AnalR) and 4 mM Glutamax (Invitrogen). This was supplemented with 0.16% glucose (AnalR), 0.21 mM hypoxanthine (Sigma), 22 µg/mL gentamycin (Sigma) and 4% human serum and 0.25% Albumax I (GIBCO-BRL). The cultures were incubated at 37℃ in a humidified atmosphere of 5% $CO_2$, 1% O2 and 90% N2. Infected red blood cells (RBCs) and uninfected RBCs (controls) were purified by magnetic purification and were fixed for 1 hour. Cells were placed in LR White™ Resin System and cryosectioned at 1 µm thickness. The sections were placed on individual 12 mm diameter x 0.5 mm thick $CaF_2$ IR grade polished windows and fixed using 2% paraformaldehyde, 0.0075% glutaraldehyde and 0.1 M cacodylate buffer. They were then washed twice with MQ water before a drop of cells was placed on the CaF2 substrates.[1]

To record TERS spectra of hemoglobin, the purified product (Sigma-Aldrich) was dissolved to $10^{-12}$ M of milliQ water and dried under vacuum to form micro-crystals.

b) Instrumentation

The TERS experiments were performed using the setup described in section 3.1. All TERS spectra were recorded with the tip in intermittent mode with a 5 and 10 second acquisition time for hemoglobin and hemozoin spectra respectively. The laser power at the sample was 500 µW in both experiments. All TERS spectra shown are raw data, no further baseline-corrections or smoothing were applied.

**Surface enhanced Raman spectroscopy**

ß-hematin for SERS analysis was prepared by the method of Bohle et al.[30] ß-hematin particles for SERS were prepared by mixing a fine suspension of β-hematin ($10^{-7}$ M) with a mixture of Ag-colloid ($1 \times 10^{-10}$ M) and NaCl (10 mM). The suspension was then spin coated on a glass plate after incubation for 30 minutes and spectra recorded at "hot spots" between Ag-nano-clusters. Laser light from a Krypton source (530 nm) was focussed onto the glass surface of the sample using a 5×, N.A. = 0.05 objective. The incident angle of the light beam was 70° with respect to the sample plain. Power was 40 mW/cm$^2$. SERRS and background light emission from nano-aggregates were collected with an objective lens (60×, N.A. = 0.15) and directed to a polychromatic equipped with a thermoelectric cooling charge coupled device using a 1200 grooves/mm CCD. White light from a 50-W halogen lamp was introduced to the focussing area by using a dark-field condenser to identify Raleigh scattering "hot spots" at the edge or between nano-clusters. These spots were selectively targeted with the microscope and spectra recorded. From Ref.[1]

**Resonance Raman Spectroscopy (RR)**

Micro Raman spectra of β-hematin and hemoglobin were recorded using a Renishaw Invia spectrograph (Renishaw plc, UK) using a 532 nm excitation line generated form frequency doubled 1064 nm Nd:YAG laser in a back-scattering geometry. A standard objective (50×, NA 0.7) was used for all measurements and each spectrum was recorded using ~60 µW and 1 accumulation at 10 seconds.[1]

**Principal Component Analysis.**

PCA was performed with the Nonlinear Iterative Partial Least Squares (NIPALS) algorithm21 in the UnscramblerTM software package (CAMO, Norway). The spectra were first pre-processed using the extended multiplicative scatter correction, which corrects for additive and multiplicative effects in the spectra, before a linear

baseline correction was made at the 1800 and 800 cm-1 minima points. The spectra were mean centered and the leverage correction algorithm applied to decompose the spectral data into its principal components. PCA was performed on forty-two TERS spectra of hemozoin collected using two different tips.[1]

## 5.4 Conclusions and outlook

In this chapter, the first TERS spectra of macromolecules recorded within a single cell are described and the bands were assigned to that of hemozoin. Using hemoglobin as a model compound, we demonstrated the selective enhancement of heme and protein modes.

With the further development of finer and more active TERS tips, the potential to investigate drug binding to the hemozoin crystal surface inside the digestive vacuole of the parasite will soon be realised as shown in Figure 5.7. According to one model Quinoline antimalarial drugs such as chloroquine (CQ) inhibit heme aggregation by binding onto the hemozoin surface through terminal functional groups (Figure 5.7.a). TERS technology provides the required lateral resolution and conceivably sensitivity for the study of drug-hemozoin binding and therefore has potential as a new method for antimalarial drug screening (Figure 5.7.band c).

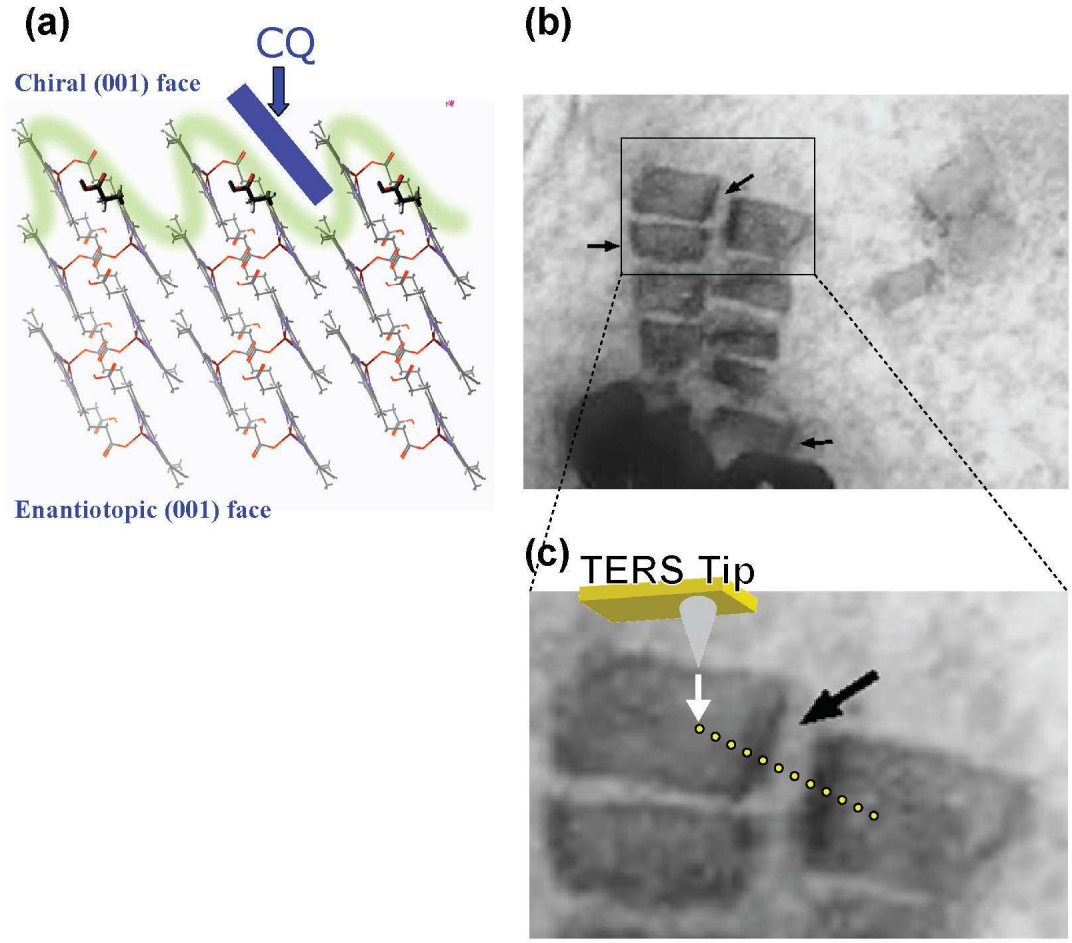


**Figure 5.7:** *(a) Chloroquine (CQ) model binding to hemozoin crystals from Ref.[31] (b) SEM image of hemozoin crystals inside a Malaria infected RBC and treated with CQ. The narrows indicate chloroquine located over hemozoin crystals. From Ref.[32] (c) Zoom image of (b) representing a TERS experiment simulation's study of drug-hemozoin binding. The yellow circles indicate the position of the TERS tips where TERS spectra will be detected.*

## 5.5 References


[1] B. R. Wood, E. Bailo, M. Asghari-Khiavi, L. Tilley, S. Deed, T. Deckert-Gaudig, D. McNaughton, V. Deckert. Tip Enhanced Raman Scattering (TERS) goes intracellular in the fight against malaria *(submitted)* **2009**.

[2] P. Trouiller, P. L. Olliaro. Drug development output from 1975 to 1996: what proportion for tropical diseases? *Int. J. Infect. Dis.* **1998**, *3*, 61.

[3] B. Greenwood, T. Mutabingwa. Malaria in 2002. *Nature* **2002**, *415*, 670.

[4] R. W. Snow, C. A. Guerra, A. M. Noor, H. Y. Myint, S. I. Hay. The global distibution of clinical episodes of Plasmodium falciparum malaria. *Nature* **2005**, *434*, 214.

[5] M. K. Jones, M. F. Good. Malaria parasites up close. *Nature Med.* **2006**, *12*, 170.

[6] L. H. Miller, D. I. Baruch, K. Marsh, O. K. Doumbo. The pathogenic basis of malaria. *Nature* **2002**, *415*, 673.

[7] D. S. Bohle, B. J. Conklin, D. Cox, S. K. Madsen, S. Paulson, P. W. Stephens, G. T. Yee. Structural and Spectroscopic Studies of {beta}-hematin (the Heme Coordination Polymer in Malaria Pigment). *Am. Chem. Soc. Symp. Ser.* **1994**, *572*, 497.

[8] S. E. Francis, D. J. Sullivan, a. D. E. Goldberg. Hemoglobin metabolism in the malaria parasite Plasmodium Falciparum. *Annu. Rev. Micobiol.* **1997**, *51*, 97.

[9] D. S. Bohle, A. D. Kosar, S. K. Madsen. Propionic acid side chain hydrogen bonding in the malaria pigment β-hematin. *Biochem. Biophys. Res. Commun.* **2002**, *294*, 132.

[10] A. F. G. Slater, A. Cerami. Inhibition by chloroquine of a novel haem polymerase enzyme activity in malaria trophozoites. *Nature* **1992**, *355*, 167.

[11] M. Abe, T. Kitagawa, K. Kyogoku. Resonance Raman spectra of octaethylporphyrinato-Ni(II) and meso-deuterated and 15N substituted derivatives. II. A normal coordinate analysis. *J. Chem. Phys.* **1978**, *69*, 4526.

[12] T. G. Spiro, T. C. Strekas. Resonance Raman spectra of heme proteins. Effects of oxidation and spin state. *J. Am. Chem. Soc.* **1973**, *96*, 338.

[13] T. Yamamoto, G. Palmer, D. Gill, I. T. Salmeen, L. Rimai. The Valence and Spin State of Iron in Oxyhemoglobin as Inferred from Resonance Raman Spectroscopy. *J. Biochem.* **1973**, *248*, 5211.

[14] A. F. Slater, W. J. Swiggard, B. R. Orton, W. D. Flitter, D. E. Goldberg, A. Cerami, G. B. Henderson. An iron-carboxylate bond links the heme units of malaria pigment. *Proc. Natl. Acad. Sci. USA* **1991**, *88*, 325.

[15] B. R. Wood, S. J. Langford, B. M. Cooke, J. Lim, F. K. Glenister, M. Duriska, J. K. Unthank, D. McNaughton. Resonance Raman Spectroscopy Reveals New Insight into the Electronic Structure of β-Hematin and Malaria Pigment. *J. Am. Chem. Soc.* **2004**, *126*, 9233.

[16] S. Pagola, P. W. Stephens, D. S. Bohle, A. D. Kosar, S. K. Madsen. The structure of malaria pigment beta-haematin. *Nature* **2000**, *404*, 307.

[17] G. T. Webster, L. Tilley, S. Deed, D. McNaughton, B. R. Wood. Resonance Raman spectroscopy can detect structural changes in haemozoin (malaria pigment) following incubation with chloroquine in infected erythrocytes. *FEBS letters* **2008**, *582*, 1087.

[18] I. Solomonov, M. Osipova, Y. Feldman, C. Baehtz, K. Kjaer, I. K. Robinson, G. T. Webster, D. McNaughton, B. R. Wood, I. Weissbuch, L. Leiserowitz. Crystal Nucleation, Growth, and Morphology of the Synthetic Malaria Pigment ß-Hematin and the Effect Thereon by Quinoline Additives: The Malaria Pigment as a Target of Various Antimalarial Drugs. *J. Am. Chem. Soc.* **2007**, *129*, 2615.

[19] T. J. Egan. Interactions of quinoline antimalarials with hematin in solution. *J. Inorg. Biochem.* **2006**, *100*, 916.

[20] T. Ichimura, H. Watanabe, Y. Morita, P. Verma, S. Kawata, Y. Inouye. Temporal Fluctuation of Tip-Enhanced Raman Spectra of Adenine Molecules. *J. Phys. Chem. C* **2007**, *111*, 9460.

[21] H. Watanabe, Y. Ishida, N. Hayazawa, Y. Inouye, S. Kawata. Tip-enhanced near-field Raman analysis of tip-pressurized adenine molecule. *Phys. Rev. B* **2004**, *69*, 155418.

[22] C. C. Neacsu, J. Dreyer, N. Behr, M. B. Raschke. Scanning-probe Raman spectroscopy with single-molecule sensitivity. *Phys. Rev. B: Condens. Matter* **2006**, *73*, 193406.

[23] K. F. Domke, B. Pettinger. Comment on ``Scanning-probe Raman spectroscopy with single-molecule sensitivity''. *Phys. Rev. B: Condens. Matter* **2007**, *75*, 236401.

[24] N. Hayazawa, H. Watanabe, Y. Saito, S. Kawata. Towards atomic site-selective sensitivity in tip-enhanced Raman spectroscopy. *J. Chem. Phys.* **2006**, *125*, 244706.

[25] S. Wold. Pattern recognition by means of disjoint principal components models. *Pattern Recogn.* **1976**, *8*, 127.

[26] B. S. Yeo, S. Madler, T. Schmid, W. Zhang, R. Zenobi. Tip-Enhanced Raman Spectroscopy Can See More: The Case of Cytochrome c. *J. Phys. Chem. C* **2008**, *112*, 4867.

[27] B. R. Wood, B. Tait, D. McNaughton. Micro-Raman characterisation of the R to T state transition of haemoglobin within a single living erythrocyte. *Biochim. Biophys. Acta* **2001**, *1539*, 58.

[28] B. Wood, P. Caspers, G. Puppels, S. Pandiancherri, D. McNaughton. Resonance Raman spectroscopy of red blood cells using near-infrared laser excitation. *Anal. Bioanal.Chem.* **2007**, *387*, 1691.

[29] W. Trager, J. B. Jensen. Human malaria parasites in continuous culture. *Sciences* **1976**, *193*, 673.

[30] S. D. Bohle, J. B. Helms. *Biochem. Biophys. Res. Commun.* **1993**, *193* 504.

[31] R. Buller, M. L. Peterson, O. Almarsson, L. Leiserowitz. Quinoline Binding Site on Malaria Pigment Crystal:  A Rational Pathway for Antimalaria Drug Design. *Growth Des. Crystal* **2002**, *2*, 553.

[32] D. J. Sullivan, I. Y. Gluzman, D. G. Russell, D. E. Goldberg. On the molecular mechanism of chloroquine's antimalarial action. *Proc. Natl. Acad. Sci. USA* **1996**, *93*, 11865.

# Chapter 6

# TERS on DNA & RNA strands: Towards a Novel Direct-Sequencing Method

DNA sequencing techniques are valuable tools in many science fields such as medicine, forensic sciences, molecular biology, archaeology or anthropology.

The sequencing of DNA is procedurally complex and requires sophisticated analytical techniques.[1, 2] DNA sequencing, while a very powerful method, requires separation and visualization methods to recognize specific DNA fragments.[3] Furthermore, all the established methods require substantial amounts of DNA and fail to directly read the base composition of the strand. A method that utilizes the inherent information of the distinct bases present in DNA or RNA without the need of further labeling is therefore desirable.

Recent approaches in this direction include pulling single DNA strands through nanopores, detecting certain electric properties, and then deducing the sequence.[4-6] Attempts were also made to directly sequence DNA by using a scanning tunneling microscope.[7, 8] In this chapter, the most popular methods and approaches to sequence DNA will be introduced and compared to a novel approach for a direct and label-free DNA sequencing method using TERS. First TERS measurements on DNA and RNA strands are shown in this work with a resolution down to a few tens of nucleobases, which just a few seconds of acquisition time and with a high spectral sensitivity.

## 6.1 Structure of DNA and RNA

Macromolecules of deoxyribonucleic acid (DNA) and ribonucleic acid (RNA) are both nucleic acid polymers and are composed of three block groups: phosphates, sugars and nucleobases. The backbone is built of phosphates and sugars, which in the case of DNA, the sugars are deoxyriboses; and in the case of RNA, riboses. Four principal nucleobases are found in DNA: adenine (A), guanine (G), cytosine (C) and thymine (T); in RNA, uracil (U) replaces thymine. Cytosine, thymine and uracil are pyrimidine derivates, while adenine and guanine are purine derivates consisting of a pyrimidine ring fused to an imidazole ring (Figure 6.1). In contrast to RNA, DNA usually forms a double strand. It occurs when two complementary polymers of DNA are attached to each other. Complementary base pairs are A to T and G to C. Double-stranded (ds) DNA occurs through a helix secondary structure. Base pairs are strictly arranged and orientated each pair is separated by a distance of approximately 0.34 nm.

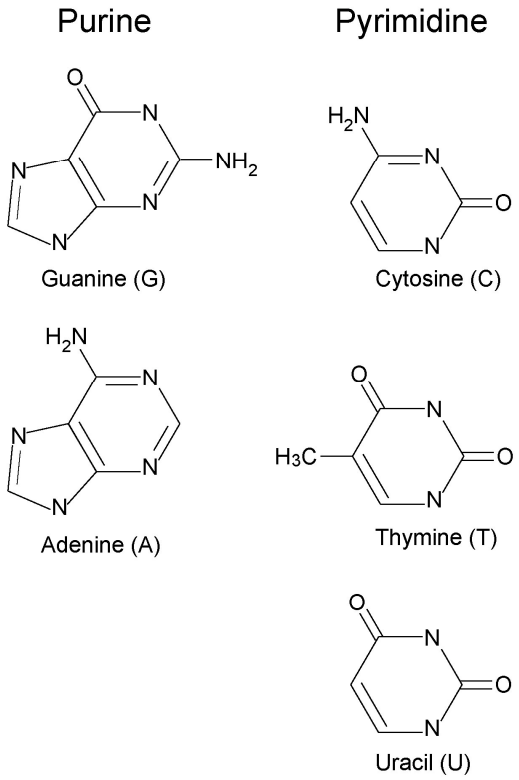


**Figure 6.1:** *Molecular structure of nucleobases found in DNA and RNA.*

## 6.2 DNA sequencing

In September 2007, John Craig Venter and his group reported the first complete DNA sequence of a human being, more precisely the Venter's genome.[9, 10] In this case, the human genome map revealed beforehand the risk of certain diseases, such as Alzheimer and cardiovascular complications. To make this approach available to conventional medicine, a standard method which provides a complete DNA sequence, approx. 3 billion bases, in a short time and at a low cost is still needed.

Since the mid-1970's, many different techniques have been developed for DNA sequencing. The more popular methods[11, 12] or approaches[12] that are currently being used will be described in the following section. The methods can be classified into: (a) chain-terminator[13-15], (b) pyrosequencing[16], (c) nanopore[4-6] and (d) Scanning tunneling microscopy (STM) methods[8].

### 6.2.1 Chain-terminator or Sanger dideoxynucleotide method

The dideoxynucleotide method, better known as the Sanger method, was first invented in 1975 by Sanger and Coulson[14, 15], and Maxam and Gilbert[13] independently and nowadays remains one of the most popular methods to sequence DNA.

The Sanger method is based on the well-known Polymerase Chain Reaction (PCR) which is used as a standard method to replicate DNA. Firstly, as shown in Figure 6.2, a short radioactive DNA sequence (primer), composed of only three bases, is complementarily assembled by controlled temperature to the starting site of the single-stranded DNA strand, known as DNA template. The DNA polymerase enzyme begins by building up the complementary DNA strand with deoxyribonucleotide triphosphates (dNTPs): dATP, dGTP, dCTP and dTTP. A modified nucleotides called dideoxy nucleoside triphosphates (ddNTPs: ddATP, ddGTP, ddCTP and ddTTP) are added at much lower concentration to the reaction. The ddNTPs are recognized by the polymerase enzyme as nucleotides and the enzyme uses them to build the complementary DNA strand. ddNTPs differ from dNTPs in that its C3-OH is substituted by C3-H on the sugar. The consequence of this small difference is that no

phosphodiester bond can be created with the next nucleotide, therefore the DNA synthesis is terminated.

Each sort of ddNTP is separately added to a reaction tube together with the same PCR reagents. Statistically, single-stranded DNA strands of the complementary DNA template will be produced in all possible lengths, because the ddNTPs will be stopped during the reaction each time in a random position.

Then, all DNA fragments are separated by length using polyacrylamide gel electrophoresis (PAGE). The position of each band is visualized by autoradiography, so that the sequence of the complementary DNA strand could be easily read.

The Sanger method has been modified from its first version, replacing ddNTPs with fluorescently labeled ddNTPs (Figure 6.3). The PCR reaction takes place only in one tube and the individual fragments of DNA are separated in function of their length again by PAGE. Each of the ddNTPs (ddATP, ddGNTP, ddCNTP and ddTNP) provides a characteristic fluorescent signal and are successively detected by laser excitation of fluorescent tags. All the detected information is then processed to read the sequence.

The Sanger method is very robust and was employed successfully in the Human Genome Project,[17] but is still time-consuming, complex (large number of reagents and labels are used) and the multiple replications increase the probability of errors in the sequencing.

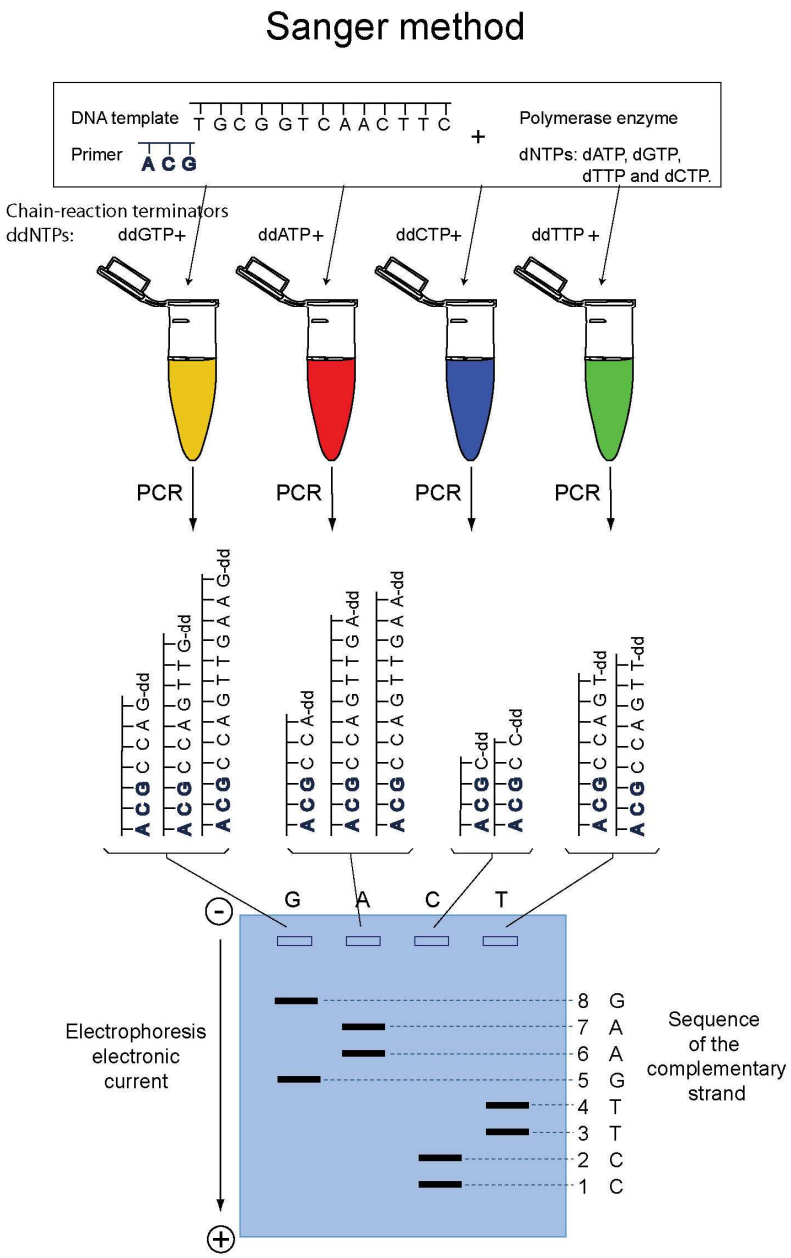


**Figure 6.2:** *Schematic diagram of the Sanger method. An ssDNA strand is replicated via PCR in four reaction tubes. Each tube contains a different ddNTP or chain-terminator nucleotide which stops the replication reaction. All possible lengths of the replicate DNA are separated by PAGE and afterwards the DNA fragments are visualized by autoradiography.*

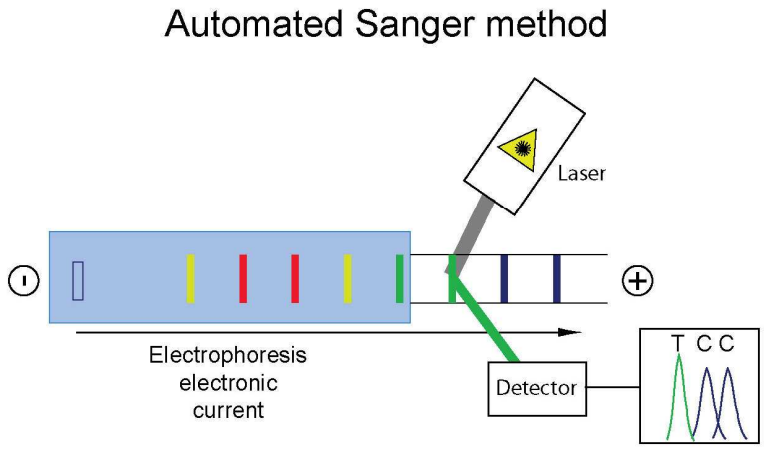


**Figure 6.3:** *Automated Sanger method. Chain-terminators or ddNTPs are fluorescently labeled, sorted by capillary electrophoresis and detected by a laser excitation of the fluorescent tags.*

## 6.2.2 Pyrosequencing

Pyrosequencing[16, 18, 19] is a second DNA sequencing method which is commonly applicable as alternative technique to Sanger method. Pyrosequencing is a three-enzyme system based on the detection of pyrophosphate (PPi) converted into light during the DNA amplification. This technique offers some advantages over the Sanger method by dispensing with labeled-primers, labeled-dNTPs, gel electrophoresis and multiple DNA replications. The overall process can be described in three steps and shown in Figure 6.4:

**Step 1 – release of PPi**

DNA amplification takes place through a standard PCR with the peculiarity that each type of dNTPs is added individually to the reaction. When the correct dNTP is incorporated, the complementary DNA strand is amplified by one base and a PPi is released.

$$(DNA)n + dNTP \xrightarrow{(DNA\ polymerase)} (DNA)n+1 + PPi$$

**Step 2 – Conversion of PPi into a molecular energy "currency" (ATP)**

PPi is converted to adenosine-5'-triphosphate (ATP) in the presence of adenosine 5´ phosphosulfate (APS) by a second enzyme called ATP sulphurylase.

$$PPi + APS \xrightarrow{(ATP\ Sulphurylase)} ATP + SO_4^{2-}$$

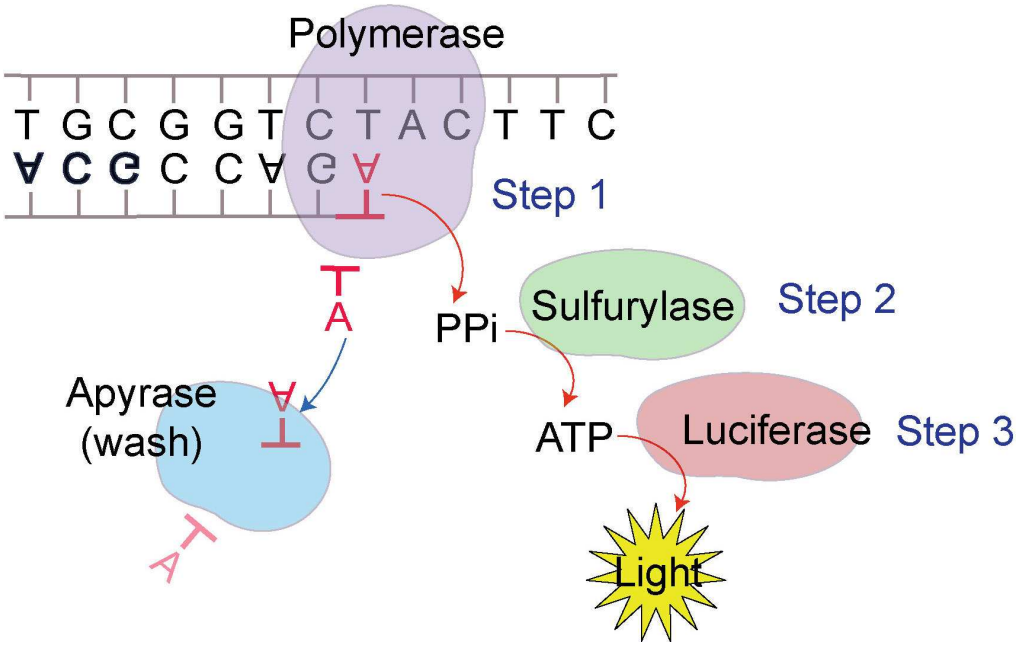


**Figure 6.4:** *Schematic diagram of the pyrosequencing. Pyrosequencing is a three-enzyme system based on the detection of pyrophosphate (PPi) converted into light during the DNA amplification.*

**Step 3 – Transformation of ATP into light**

A third enzyme called Luciferase performs the transformation of ATP into visible light, which is detected by a CCD camera. The light signal emitted is proportional to the number of bases incorporated in the amplification of the complementary DNA strand.

$$ATP + Luciferin + O_2 \xrightarrow{(Luciferase)} AMP + PPi + Oxyluciferin + CO_2 + Light$$

Finally, the excess dNTPs are degraded by a washing enzyme called Apyrase. When degradation is finished, the sequencing continues to restart the enzymatic cycle again adding a new sort of dNTP.

Pyrosequencing incurs lower costs but is still time-consuming and a complex technique, since PCR must be used.

## 6.2.3 Nanopore methods

In contrast to the previous two methods, DNA sequencing via nanopores[6, 20, 21] is an approach which does not require any amplification of DNA template. As the nanopore the protein α-hemolysin is used (Figure 6.5.a), which has an inner diameter of only 1.5 nm at the narrowest region.

In this method, a single-stranded DNA sequence goes through a nanopore, blocking the normal current flow of other ions. Theoretically, each nucleobase induces a specific change in the ionic current flow, as a result the sequence can be deduced by measuring the ionic current during the translocation[4] (Figure 6.5.b and c).

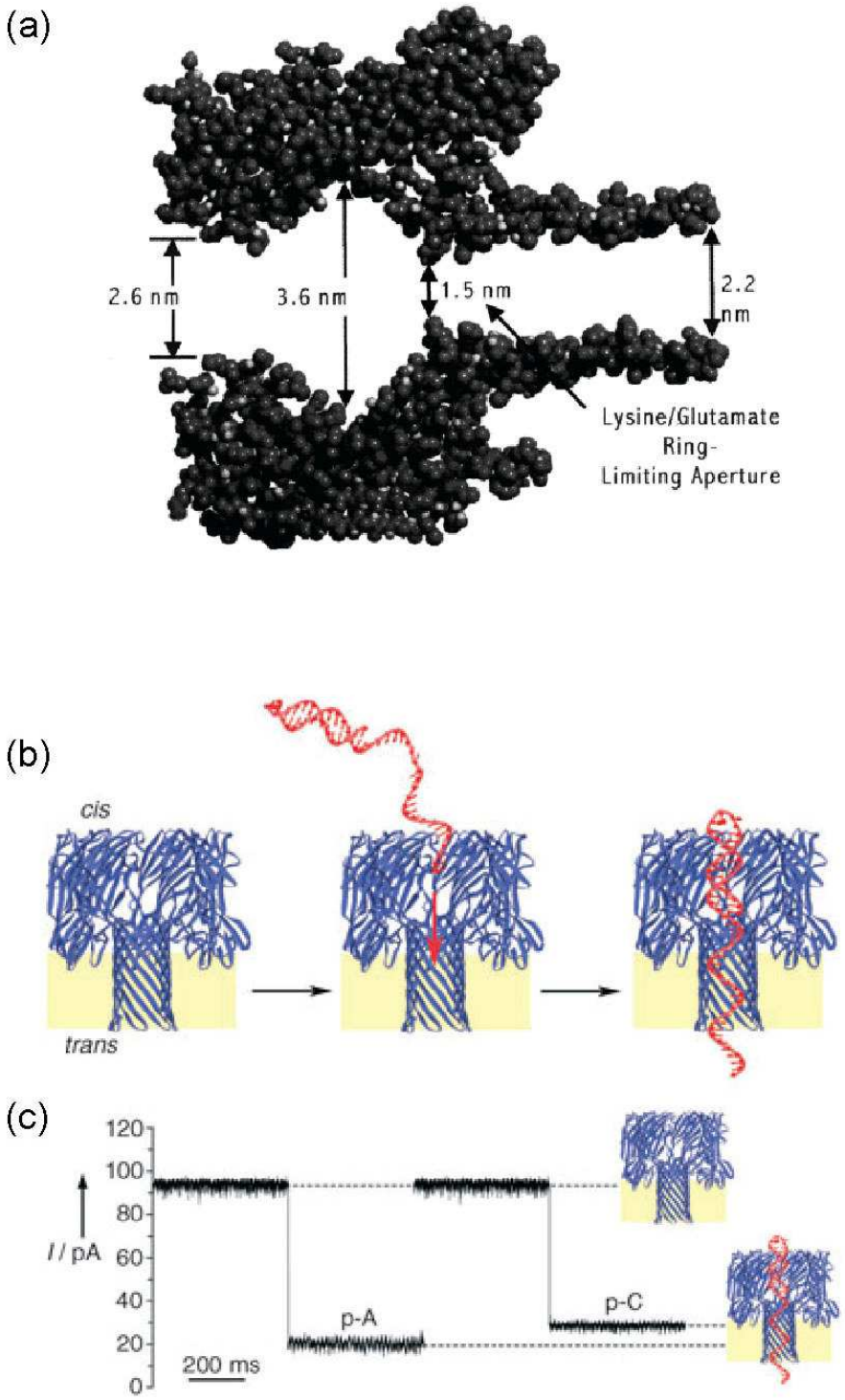


**Figure 6.5:** *Nanopore method. (a) Structure of a nanopore of α-hemolysin,[21] (b,c) a single-stranded DNA sequence goes through a nanopore, blocking the normal current flow of other ions.[20]*

To put this method in practice is not as easy as one would presume. Firstly, the pores are very long and at the narrowest region, they are found to be up to 10-20 nucleotides long, far from the single-base resolution required for DNA-sequencing. Secondly, the pore diameters are too large to avoid twisting of the DNA within the pore, which induces large noise. In protein-nanopores, the diameter of the nanopore is restricted to the natural channel the protein itself and cannot be modified, therefore artificial nanopores would be the best solution.

In 2006, Di Ventra's group proposed a model using nanopores of silicon nitride[6] with a diameter smaller than the α-hemolysin channels. Additionally, this model has two pairs of electrodes which achieve the electric current perpendicularly to the translocated DNA. This improved model should allow a single-base resolution and avoid the twisting and turning of DNA within the pore (Figure 6.6). If this model is correct, this technique will be much faster, cheaper and would avoids the use of labeling and the replication of DNA.

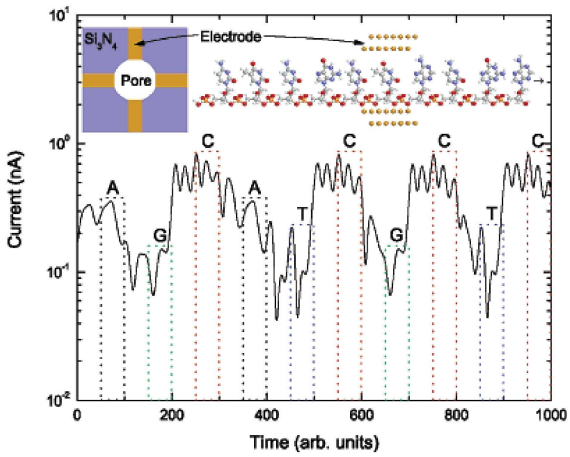


**Figure 6.6:** *Nanopore method model using a $Si_3N_4$ nanopore.[6] A single-stranded DNA translocates through a $Si_3N_4$ nanopore, the sequence is read by the different distributions of transverse electrical currents of each nucleobase. From Ref.[6]*

### 6.2.4 Scanning tunneling microscopy (STM) method

Another approach to consider for DNA sequencing is the identification of complementary base-pairings using scanning tunneling microscopy (STM). The ability of STM to achieve atomic resolution images of conductive surfaces is well-known [22-24].

Ohshiro and Umezawa have demonstrated that the bonds created between the molecules and the metal do not have to be strong and covalent.[8] They showed that the tunnel current between bases could be significantly enhanced by hydrogen bonds when a complementary base-pair is being formed. Chemically modified metal tips with thiol derivates of the four nucleobases (using isolating nucleotides) are employed to identify chemically selective base-pair bonding between the molecular tip and its complementary nucleobase (see Figure 6.7). The main challenge with STM methods is always the low contrast and usually a statistic approach is necessary to evaluate the data.

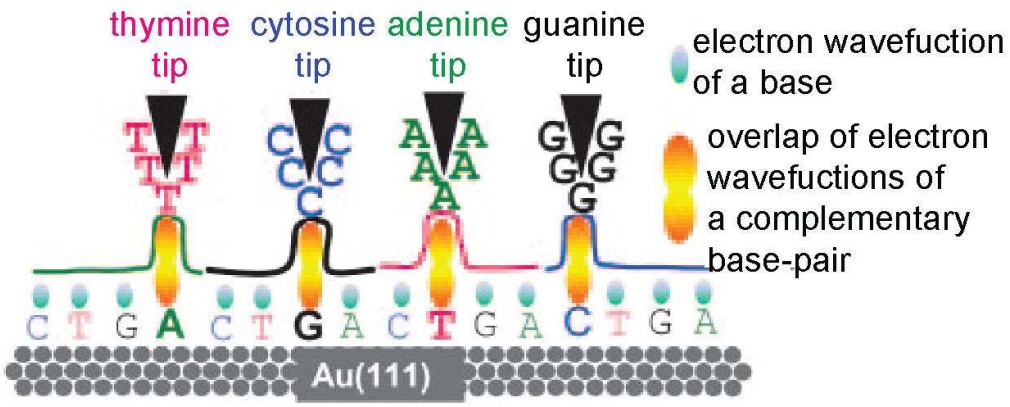


**Figure 6.7:** *Schematic diagram of scanning tunneling microscopy (STM) method for DNA sequencing. Modified nucleobase tips enhance electron tunneling by formation of complementary base pairs. From Ref.* [8]

## 6.3 Tip-Enhanced Raman Spectroscopy of Single RNA Strands: Towards a Novel Direct-Sequencing Method

Our studies demonstrate that, using near-field optical techniques in combination with vibrational spectroscopy gives high contrast and hence the direct identification of bases on a single isolated RNA strand becomes feasible[25]. Standard Raman spectroscopy makes the identification of the base components straightforward; however, the lateral resolution and the sensitivity of the method are far from the single-strand or even the single-base detection levels required for a sequencing method. Herein we show that TERS provides several advantages over conventional Raman spectroscopy: in just a few seconds of acquisition time, high sensitivity at a lateral resolution down to a few tens of nucleobases can be achieved.[26, 27] These properties allowed TERS mapping along a poly(cytosine) RNA strand. The results demonstrate the potential of the method to identify and sequence the composition of polymeric biomacromolecules, such as DNA, RNA and peptides.

TERS spectra of a single-stranded RNA homopolymer of cytosine (poly(rC)) have been measured with a spatial resolution down to a few nucleobases. The basic experiment is shown in Figure 3.1 in Chapter 3. A standard back-reflection TERS setup is used to focus a laser onto a silver-coated atomic-force microscope (AFM) tip, while the sample is moved independently, the sample surface is thus always in focus. In Figure 6.8 the topography image of a single-stranded RNA cytosine homopolymer is shown. To avoid Raman scattering from compounds other than RNA, the use of buffer solutions and other chemicals was restricted to a minimum. However, as a result, entangling of the strands was a major issue and an extensive search for the linear single RNA strands needed for the measurements is required. The height of the strand shown in the profile measurement (Figure 6.8) corresponds to the known diameter of RNA, which strongly supports the identification of single strands. The effective area probed by an AFM tip is a convolution of tip and sample features. Hence, the measured strand width of approximately 10 nm can be largely assigned to the silver-coated AFM tips and corresponds well with the tip diameter of <20 nm determined by SEM (Figure 3.2 in Chapter 3). The length of the homopolymer chain appears longer than expected and the small nodule-like feature in the center of the strand indicates that most likely

two strands are attached to each other. However, these features had no impact on our further experiments as the length of the strand was not relevant. It is important to note that apart from the RNA no further topographic features are present. Thus other compounds (e.g. buffer crystals, etc.) can be ruled out for this particular sample area, making the evaluation of the Raman spectra amenable and without ambiguity.

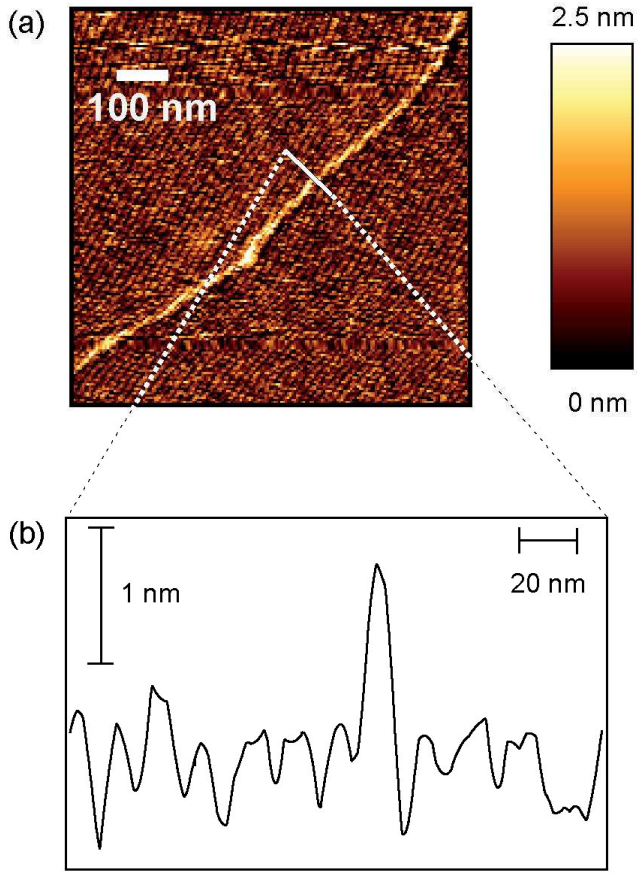


**Figure 6.8:** *Topography of a cytosine single-stranded RNA homopolymer. (a) AFM height image ("intermittent" contact) of a single poly(cytosine) RNA strand on freshly cleaved mica. The image is baseline corrected. (b) Height profile through the RNA along the line indicated in (a). From Ref.* [25]

Previous TERS measurements performed on single, nanometer-sized crystals or on monolayers of nucleobases demonstrate that the individual fingerprint of each nucleobase and the characteristic vibrations required for the distinction of each

compound can be found easily.[28, 29] In contrast to these previous investigations, the technical tolerances for a TERS experiment on a single DNA or RNA strand are much more stringent. The field-enhancing tip must be placed and held over the homopolymer during the whole laser exposure for the Raman experiment. It is crucial that the sample drift is nullified so that all subsequent measurement points are also on the RNA strand. In our experiment we measured TERS spectra at seven different positions along the single-stranded RNA chain (Figure 6.9).

Figure 6.11 shows the TERS spectrum of a single strand of poly(cytosine). The results contain all the main spectral features of cytosine. The TERS bands of poly(cytosine) (in $cm^{-1}$) and the band assignments are shown in Table 6-1. For the band assignment, the TERS spectra of poly(rC) have been compared to the Raman and SERS spectra of cytosine[30] and deoxycytidine (dC)[31] and the density functional theory (DFT) calculation of cytosine[32], the molecular structures are shown in Figure 6.10. Cytosine has several sites which can bind directly to a metal surface, such as N(3), C=O and C=N. The TERS band at 801 $cm^{-1}$ is assigned to the ring breathing of pyrimidine (py) and corresponds satisfactorily with the typical frequency of dC bound to a metal surface.[31] In comparison to the normal Raman band, at 784 and 792 $cm^{-1}$ for cytosine and dC respectively, a significantly higher frequency shift is observed. This blue-shift is due to the adsorption of some atoms of the cytosine ring (py) with the silver nanoparticle at the end of the tip. This adsorption induces a redistribution of the electronic charge density taking place in the ring and therefore, the corresponding shift of the signal. [30, 31]

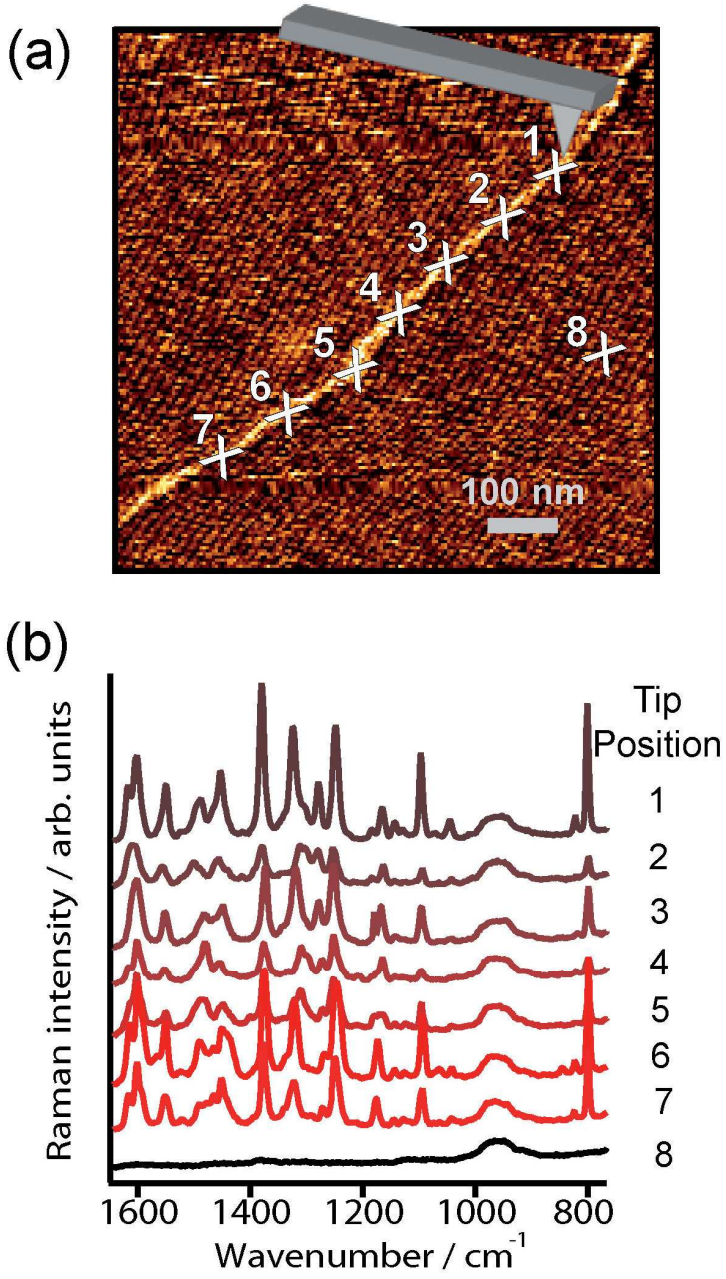


**Figure 6.9:** *TERS experiment along a RNA strand. (a) Topography image (same as in Figure 6.8.a) showing seven adjacent spots corresponding to the positions of the TERS experiments and one additional spot for the reference measurement (position 8). (b) The Raman spectra of the positions are marked in (a). For all TERS spectra the laser intensity at the sample was set to 1 mW, at 530.9 nm and the acquisition time was 15 s. From Ref.[25]*

The highest frequency mode observed in the TERS spectra appearing at 1618cm$^{-1}$ is assigned to the C=O stretching vibration of the carbonyl group. In the normal Raman and SERS spectra of dC, this band appears at 1664 and 1638 cm$^{-1}$ [31] respectively and also in the normal Raman and SERS spectra of cytosine, the C=O stretching vibration experiments a red-shift from 1655 to 1640 cm$^{-1}$.[33] An even larger shift was observed for this band in the TERS spectrum of a monolayer of cytosine adsorbed at Au(111) according to Domke's work.[29] This large red-shift is attributed to the decrease of the double bond character of the carbonyl group due to the electron donation from the C-O to the metal surface, and consequently the decrease of the vibrational frequency.[29, 31, 33] Furthermore, the C(2)-N(3) stretching vibration is shown at 1279 cm$^{-1}$ in the TERS spectra, in agreement with the suggested closeness of the carbonyl group to the Ag tip.

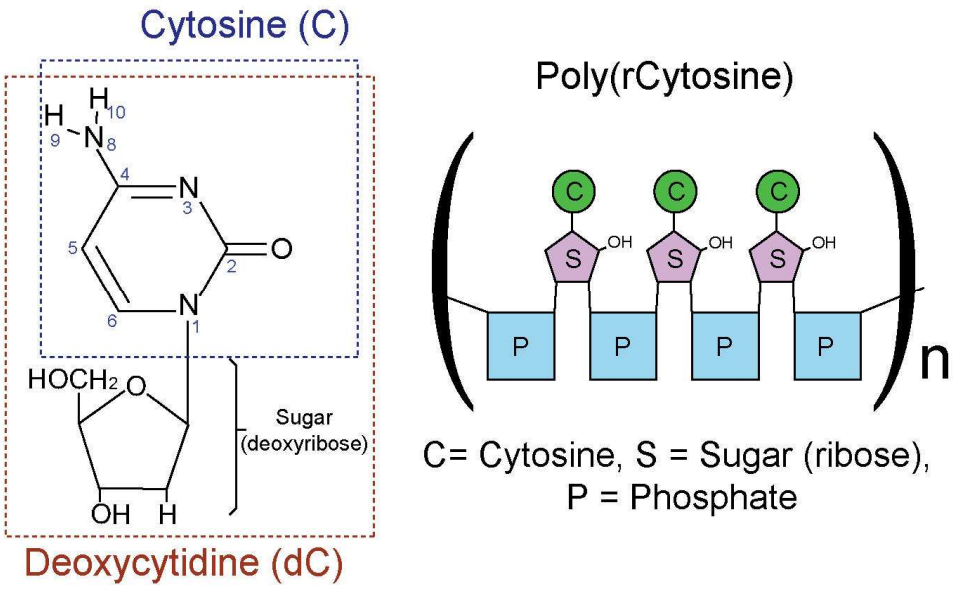


**Figure 6.10:** *Molecular structures of cytosine, deoxycytidine and RNA homopolymer of cytosine.*

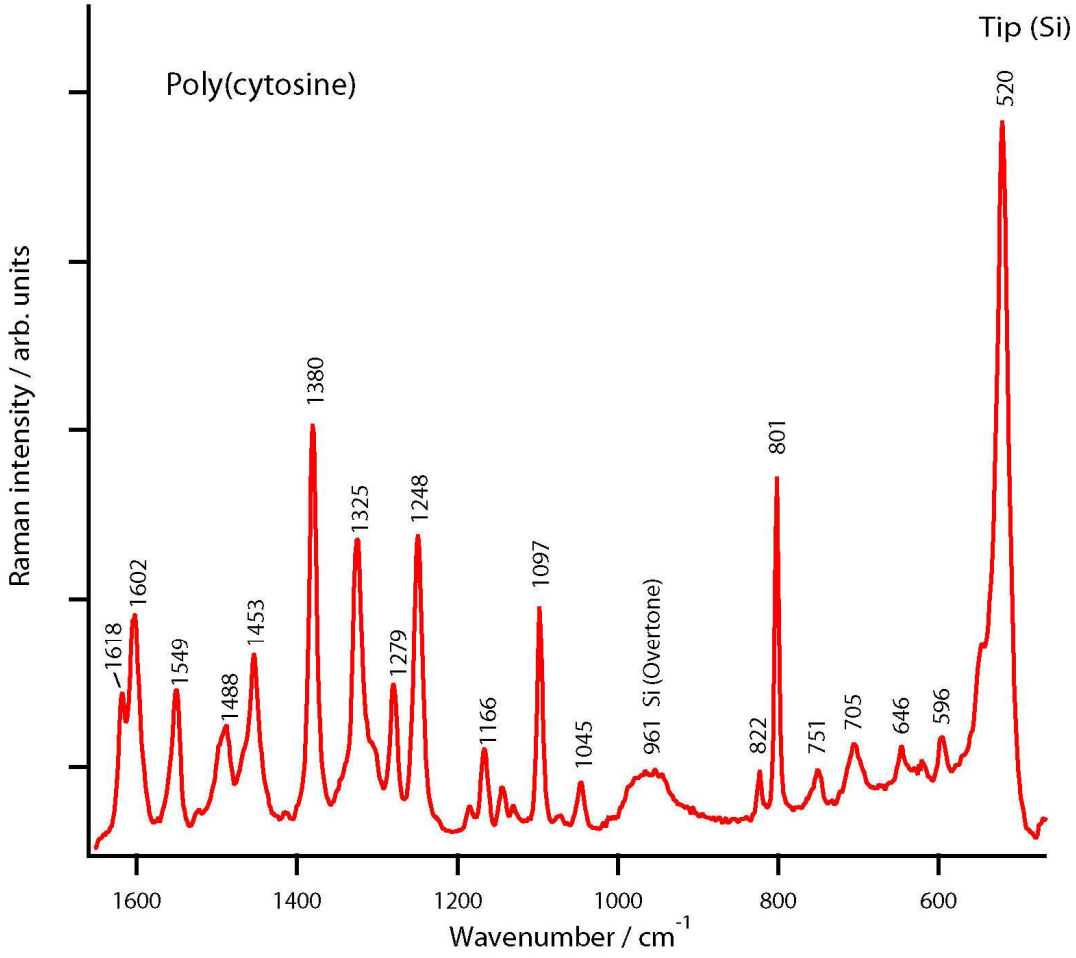


**Figure 6.11:** *TERS spectrum of a single-stranded homopolymer of cytosine immobilized on mica. The TERS band at 801 $cm^{-1}$ is the characteristic fingerprint band assigned to the ring breathing mode of cytosine. The bands at 520 and 961 $cm^{-1}$ correspond to silicon arising from the background scattering of the AFM cantilever.*

**Table 6-1:** *Assignments of TERS spectrum of poly(rC) (in $cm^{-1}$)*

| mode | NRS[a] | DFT[b] | SERS[a] | TERS | SERS[c] | NRS[c] | assigment |
|---|---|---|---|---|---|---|---|
| 1 | | | | **520** | | | silicon (AFM tip) |
| 2 | 599 | | 597 | **596** | | | ring df (sqz group, C2-N3-C4)[a] |
| 3 | | | | **646** | | | mica (sample substrate) |
| 4 | | | | **705** | | | mica (sample substrate) |
| 5 | | | | **751** | | | mica (sample substrate) |
| 6 | 792 | 803 | 794 | **801** | 802 | 784 | ring breathing (Py)[a] |
| 7 | | | | **822** | 847 | 850 | (N3-C4-N8) st[c] |
| 8 | | | | | 949 | 950 | $NH_2$ rk[c] |
| 9 | | | | | 1033 | 1024 | N-Sugar st[c] |
| 10 | | 1045 | 1033 | **1045** | | | N8-H9 df, N8-H10 df[a] |
| 11 | 1107 | 1106 | 1115 | **1097** | | | C5-H df[a] |
| 12 | | 1146 | (1194) | **1166** | | | |
| 13 | 1249 | 1245 | 1233 | **1248** | | 1240 | all H df[a] |
| 14 | 1275 | 1273 | | **1279** | 1293 | 1290 | all H df[a], C2-N3 st [c] |
| 15 | | | | **1325** | | | ? |
| 16 | 1363 | 1359 | 1363 | **1380** | 1419 | 1417 | C5-H, C6Hdf[a], C4-C5 st[c] |
| 17 | 1459 | 1458 | | **1453** | 1458 | 1448 | $NH_2$ sci [a], C4-$NH_2$ st [a], C=N st Py)[c] |
| 18 | | 1490 | 1494 | **1488** | 1498 | | ring df (C4-C5 st)[a], all H df[a], $NH_2$ df[c] |
| 19 | | 1531 | | **1549** | | 1533 | $NH_2$ df[c] |
| 20 | 1605 | 1606 | 1574 | **1602** | 1572 | | ring df (C5-C6 st)[a], $NH_2$ sci [a] |
| 21 | | | | **1618** | 1638 | 1664 | C=O st.[c] |

[a] from Ref. [30] *(Cytosine, SERS solution Ag and Raman)*

[b] from Ref. [32] *(Cytosine, Calculation SQM B3-LYP/6-31G*)*

[c] from Ref. [31] *(Deoxycytidine (dC), SERS solution Au)*

Abbreviations: NRS, normal Raman scattering; DFT: density functional theory;
SERS: surface-enhanced Raman scattering; Py, pyrimidine; bk, backbone;
st, stretching; df, deformation; rk, rocking; sci, scissoring.

The enhancement of the C=O and C(2)-N(3) stretching vibrations can be explained by their proximity to the metal tip. It is reasonable to expect an enhancement as well for the $NH_2$ group because of its closeness to the carbonyl group, see the schematic sketch in Figure 6.12. The corresponding $NH_2$ deformation band is easily found at 1488 $cm^{-1}$ in the TERS spectra and its assignment confirmed by the SERS spectrum of dC with Au nanoparticles, appearing in this case at 1498 $cm^{-1}$.[31]

The observation of the enhancement of the C=O stretching at 1618 $cm^{-1}$, C(2)-N(3) stretching at 1279 $cm^{-1}$ and $NH_2$ deformation at 1488 $cm^{-1}$ supports strongly the idea that cytosine ring is orientated upright with the carbonyl group directed to the metal tip as shown in Figure 6.12). This corresponds with the immobilization procedure employed for the RNA strand on mica (see section 6.5).

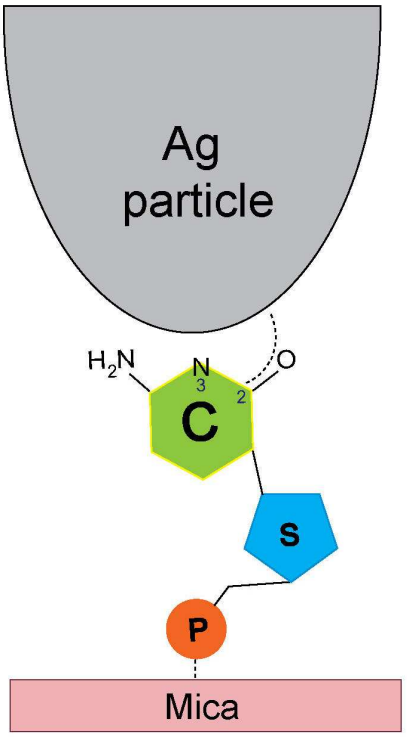


**Figure 6.12:** *Proposed orientation of poly(rC) bound to the Ag-coated tip via carbonyl group.*

The observed fluctuations of the band intensities and positions exceeding statistical variations will be discussed below. Most importantly the results demonstrate the stability of the setup because the RNA could always be readily located. To show that the probe was not contaminated, reference measurements at sample sites without RNA were also measured (see Figure 6.9.b at position 8). In these measurements no indication of RNA Raman bands or any other Raman bands, apart from silicon (arising from background scattering of the AFM cantilever) and mica (substrate material), could be found. This comparison also allows an estimation of the actual Raman enhancement. For this estimation we follow essentially the argument outlined in Refs.[34, 35]

To estimate the enhancement, the number of molecules responsible for the signal both in the TERS experiment and in the reference case must be considered. The diameter of laser focus was 1 µm. In the reference case we assume that one RNA strand is stretched along the diameter of the laser focus (as indicated in Figure 6.13.b). The signal of the unenhanced 1-µm-long RNA chain obtained when the tip was positioned next to this strand (Figure 6.9.b spectrum position 8) is then used as the reference spectrum. In our experiments, no signal was detectable at this position under conditions identical to those for the other measurements.

In the TERS spectrum only a small RNA fragment of 20 nm length is responsible for all the signal intensity (see inset in Figure 6.13.c). Hence, the relationship between the number of bases responsible for the Raman signal in the reference (ca. 3000 bases) and the TERS case (ca. 30–60 bases) is approximately 50-fold. In conjunction with the relationship between the signal-to-noise ratio (SNR) of the reference and the TERS spectrum, which is about 200:1, was obtained by dividing the intensity of the most intense Raman band by two times the standard deviation of the noise level measured in a signal-free section of the spectrum. We can estimate an overall enhancement of the TERS signal of at least $10^4$. This is a very cautious estimation as it does not take into account the duty cycle of the oscillating tip and also all other parameters considered (tip size, SNR) are estimated very conservatively. However, in terms of sensitivity, the present TERS experiments are already very satisfactory. The SNR of approximately 200 stems from 30–60 bases underneath the

TERS tip. Assuming a homogeneous signal enhancement, every single nucleobase then contributes with a SNR of 3–7 to the spectrum, making every base distinguishable. **This means that single-base sensitivity has been easily achieved, which is one of the prerequisites required for DNA sequencing using TERS!**

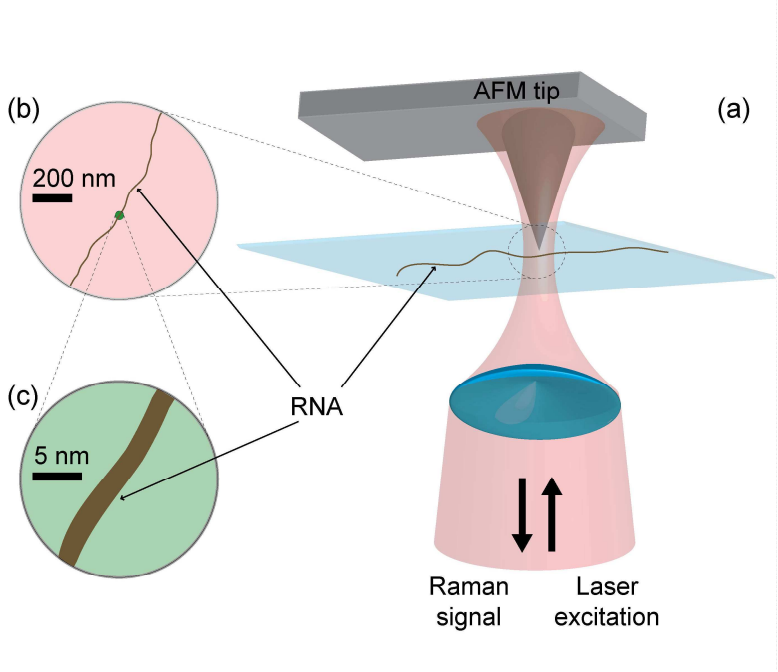


**Figure 6.13:** *(a) The tip-enhanced Raman scattering (TERS) experiment along a single strand of RNA. (b) Higher magnification of the area approximately corresponding to the size of the laser spot. (c) Magnification corresponding to the interaction area of the TERS probe tip.*

A closer look at the spectra of the RNA strand (Figure 6.14) shows slight changes in band intensities and positions. Band intensity changes resulting from different concentrations of RNA can be easily ruled out; the AFM images simply do not indicate the presence of multiple strands or other visible traces of molecules that interfere with the Raman spectra. A better explanation for intensity changes is the dependency of the enhancement on minuscule distance changes between probe and sample.[36-38] As the sample in the experiments is very small, probe positioning variations even below a nanometer could be sufficient to cause intensity changes (see

Figure 6.15). In our case, the single RNA strand has a defined direction and even specific bends in the orientation of neighboring bases can induce changes in intensities and intensity ratios of distinct bands. As long as the interaction between the adjacent bases does not vary strongly, band shifts should be negligible and the band positions should be the same for all cytosine groups.

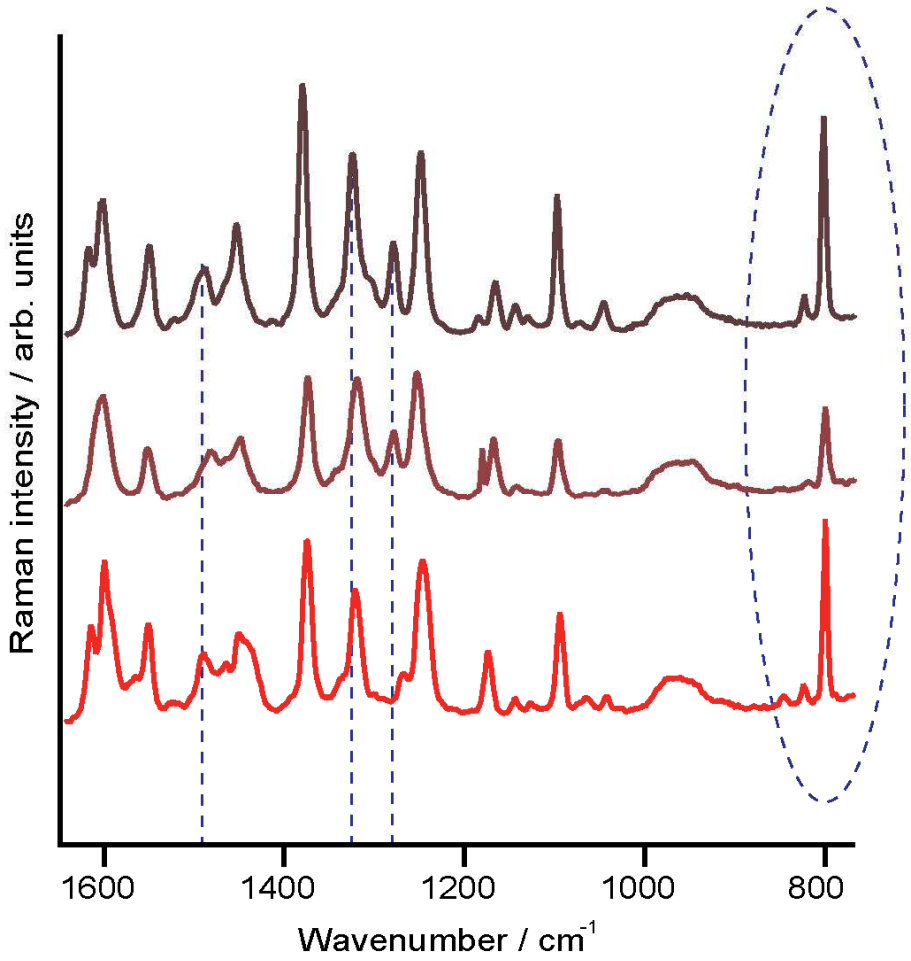


**Figure 6.14:** *Fluctuations in intensity (blue ellipsoid) and band position (blue lines) are observed in the TERS spectra.*

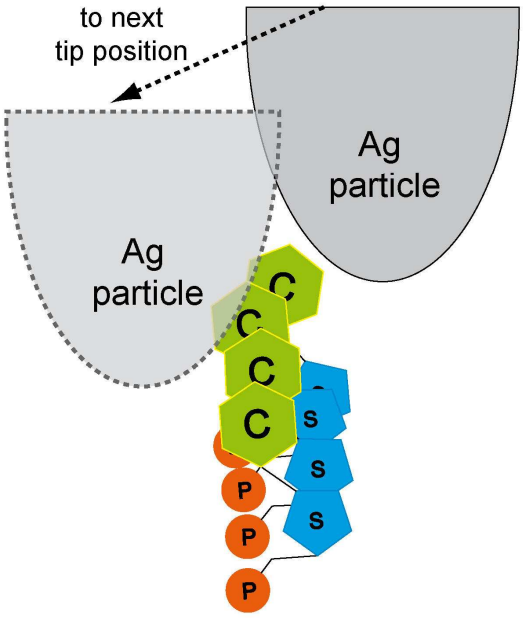


**Figure 6.15:** *Visualization of the position effect of the TERS tip with respect to the strand. Probe positioning variations even below a nanometer can cause intensity fluctuations.*

Figure 6.14 shows that the positions of some Raman bands also shift slightly. Again the positioning of the TERS probe with respect to the molecules provides a plausible qualitative explanation. It has been shown by Watanabe et al. [39, 40] that a strong dependence exists between the local position of a silver atom and the orientation of the probed molecule, as shown in Figure 6.16, where Raman spectra of the five possible complexes of Ag-adenine were calculated by DFT, providing information about fluctuations in intensity and band position. In most chemically relevant conditions the silver atom and analyte molecule will arrange themselves in the energetically most favorable position.[39, 40] However, because of restricted flexibility, the RNA is fixed to the substrate and the silver coated TERS probe is held in a certain position in a TERS experiment, the system is forced into a specific arrangement. This arrangement will cause the bands to shift slightly from positions known from either solution or single-molecule experiments. One last difference between a standard

Raman microscope experiment and a near-field Raman experiment such as TERS is the change in polarization direction and electromagnetic-field distribution. Longitudinal fields play an important role in the near-field and therefore new selection rules can arise.[41] The same effects can occur with strong field gradients at metal surfaces, as shown by Ayars et al.[42] All these effects can explain the variations occurring in the spectra. More importantly from a practical viewpoint is that the spectra could always be attributed to Raman bands assigned to cytosine in the literature.[30-32, 43] Hence a distinction from other compounds should be straight forward and even sequencing of natural RNA strands will become feasible.

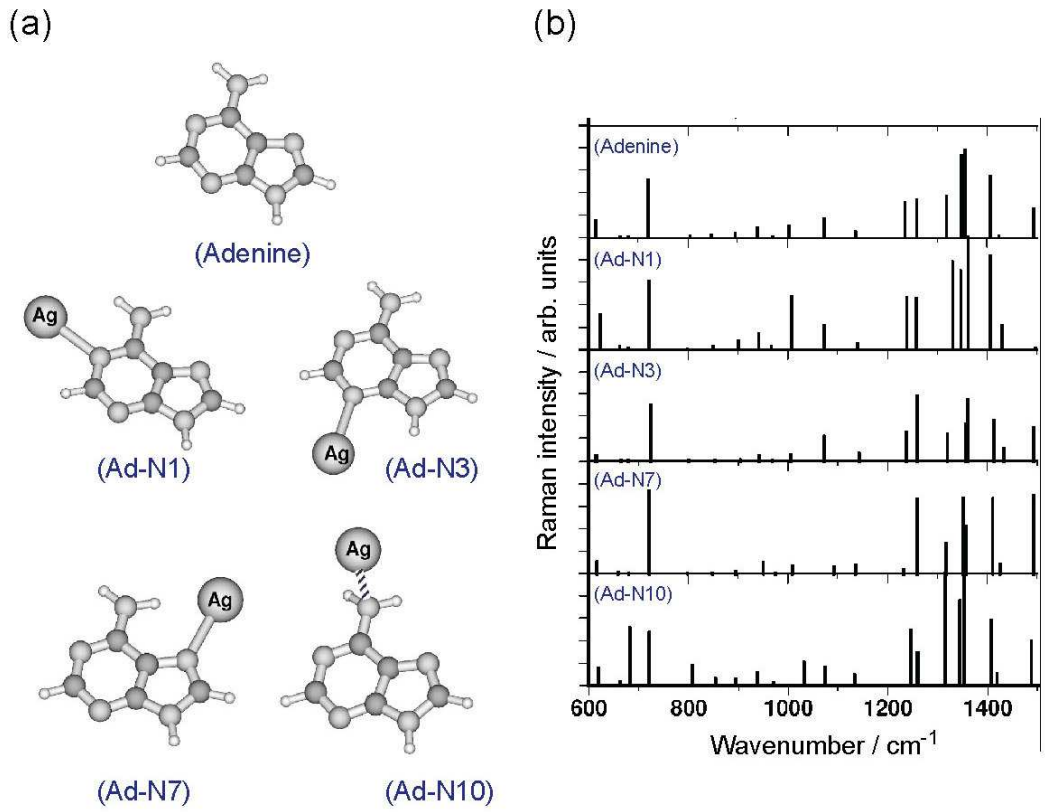


**Figure 6.16:** *(a) Molecular structures of adenine and its potential silver complex isomers. (b) The calculated Raman spectra of adenine and its silver complex isomers by DFT. Figure reproduced from Ref.[40]*

## 6.4 Reproducibility and enhancement region of TERS on DNA strands

The previous experiment shows fluctuations that can be explained by specific nanoscale effects. For that reason in the following TERS experiment, a homopolymer of DNA is measured by an Ag-coated tip moving across the strand to investigate the variation of these fluctuations. In addition, reproducibility of the TERS spectra at the same position has been examined.

For this experiment DNA instead of RNA and another nucleobase, adenine, has been chosen as a homopolymer. The AFM image (Figure 6.17) of the adenine homopolymer of (poly(A)) shows at the cross section a height slightly above the standard height of a single strand. This means the sample is either coiled or two or three strands are lumped. Figure 6.18 shows the TERS spectra measured at eight different positions across the DNA. The distance between two distinct positions was 10 nm. TERS spectra of poly(dA) have been achieved at only three positions and only two of them showing a high enhancement. These two spectra provide information on the area of the enhancement of the TERS tip. Taking the 10 nm distance between the two positions into account, an enhancement region below 20 nm can be safely estimated. This value corresponds well with the diameter of the metal tip, which is usually used to estimate the number of molecules involved in a TERS spectrum.

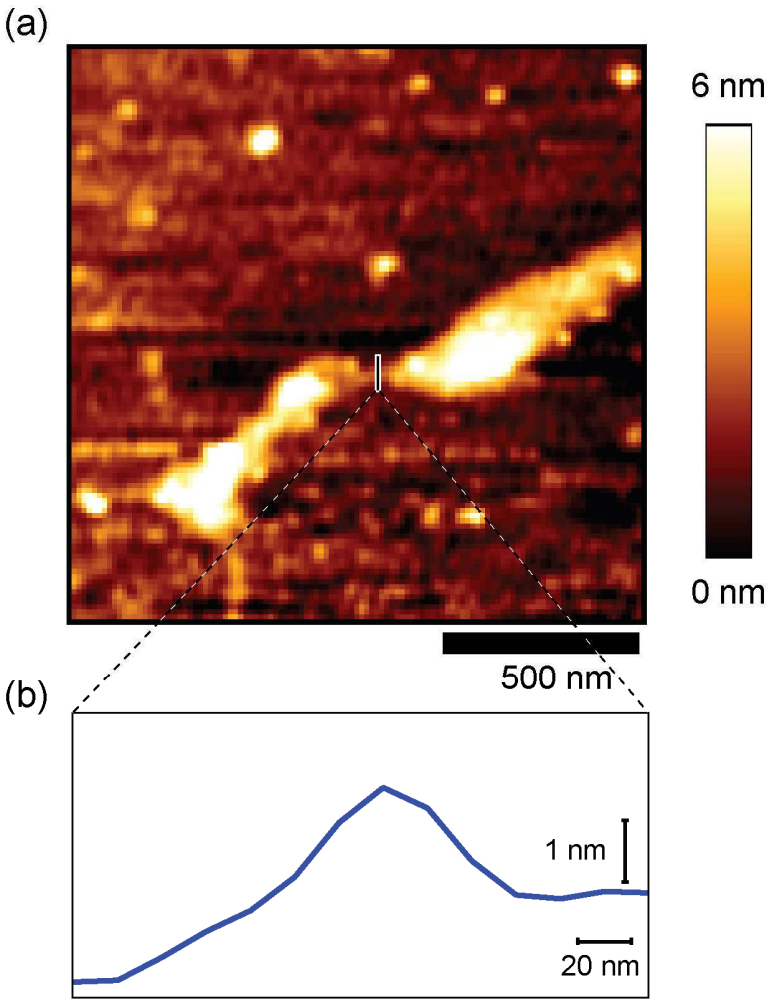


**Figure 6.17:** *(a) AFM topography image of a homopolymer of DNA (adenine) and (b) its corresponding cross section at the marked positions in (a).*

Most importantly both spectra show the main spectral features of adenine. Additionally we are able to observe some bands belonging to DNA backbone (sugar and phosphates moieties). This can be attributed to the fact that DNA strands were not rigidly orientated on the mica substrate.

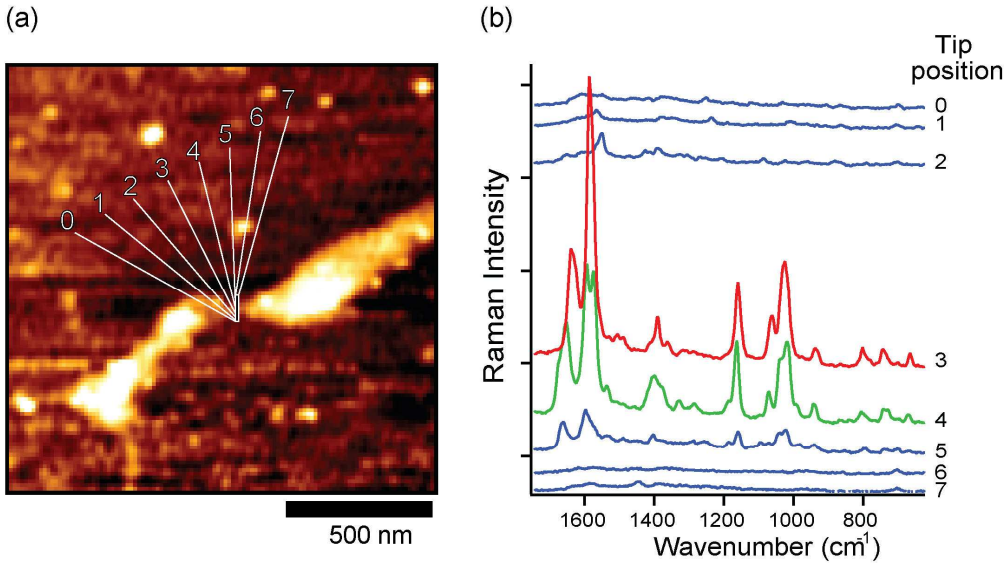


**Figure 6.18:** *(a) AFM image of a homopolymer of DNA (adenine) and (b) TERS spectra at the positions are marked in (a). For all TERS spectra the laser intensity at the sample was set to 500 µW, at 530.9 nm and the acquisition time was 5 s.*

In addition, each TERS spectrum was measured twice at the same position to check for the reproducibility. The duplicate (a, b respectively) spectra at position 3 and 4 shown in Figure 6.19 are nearly identical. This confirms that the fluctuations observed in TERS spectra between different positions can be attributed to nano-scale effects.

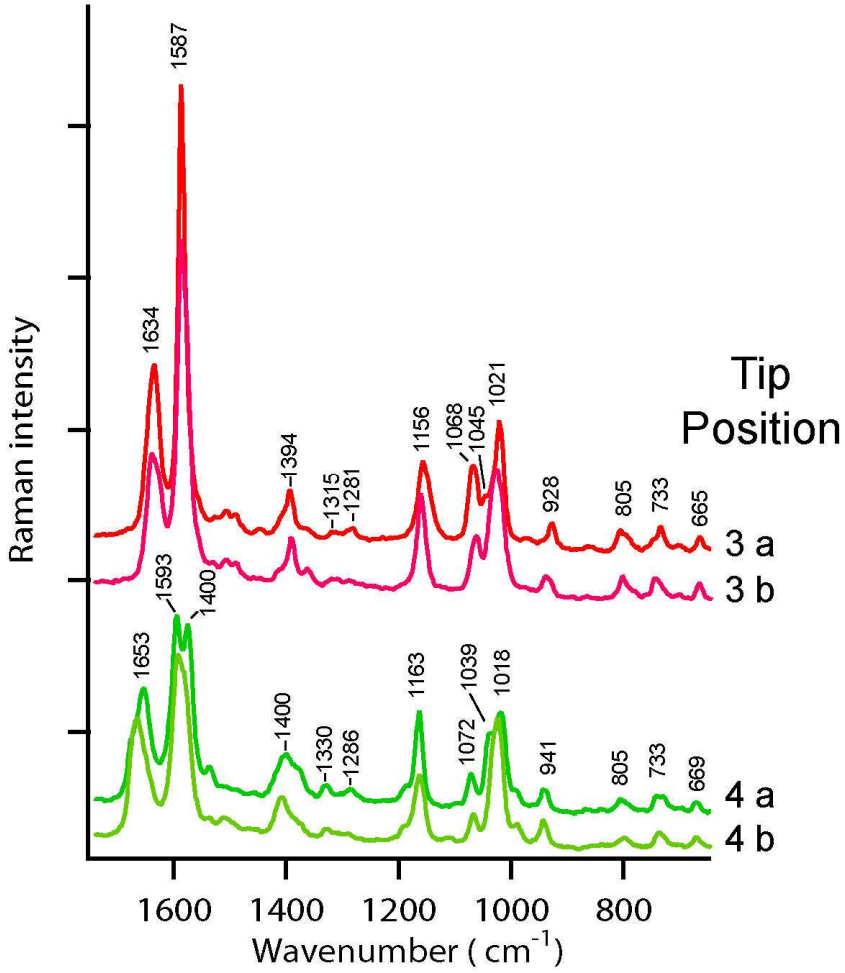


**Figure 6.19:** *TERS spectra of poly(dAdenine) at position 3 and 4 marked in Figure 6.18 measured twice (a,b). For all TERS spectra the laser intensity at the sample was set to 500 µW, at 530.9 nm and the acquisition time was 5 s.*

The band positions of both spectra, at positions 3 and 4 marked in Figure 6.18 and listed in Table 6-2. For the band assignment, they have been compared with the SERS and Raman spectra of adenine derivates, such as deoxyadenosine (dA),[31] deoxyadenosine monophosphate (AMP)[33] and single-stranded homopolymer of adenine (poly(dA))[30] (see Figure 6.20 for the molecular structures).

**Table 6-2:** *Assignments of the TERS spectra of poly(dA) ( in $cm^{-1}$)*

| mode | TERS$^{(p3)}$ | TERS$^{(p4)}$ | SERS[a] | NRS[a] | SERS[b] | NRS[c] | assigment |
|---|---|---|---|---|---|---|---|
| 1 | **520** | **520** | | | | | silicon (AFM tip) |
| 2 | **665** | **669** | | | | 663 | ring[c] |
| 3 | **733** | **733** | 728 | 734 | 732 | 727 | ring breathing (Py)[a,c] |
| 4 | **805** | **805** | | | | 790/ | bk (OPO st), ring [c] |
| 5 | | | | | | 842 | bk (OPO st) [c] |
| 6 | **928** | **941** | 919 | 908 | (960) | 917 | $NH_2$ rk[a], sugar[c] |
| 7 | **1021** | **1018** | | | | 1007 | $NH_2$ df |
| 8 | **1045** | **1039** | 1035 | | | 1052 | N-sugar st[a], sugar (CO |
| 9 | **1068** | **1072** | | 1066 | | 1092 | N-sugar st[a], bk ($PO_2^-$ st)[c] |
| 10 | **1156** | **1163** | 1171 | 1174 | | 1163 | (C5-C6) st[a] |
| 11 | | | | | | 1204 | ring[c] |
| 12 | | | | | | 1221 | ring[c] |
| 13 | **1281** | **1286** | | | 1264 | 1251 | ring[c] |
| 14 | **1315** | **1330** | 1320 | 1348 | 1334 | 1306 | C-N st[a], ring[c] |
| 15 | | | | | | 1336 | ring[c] |
| 16 | | | | | | 1345 | ring[c] |
| 17 | **1394** | **1400** | 1389 | 1380 | 1370/ | 1378 | (C6-N1) st (Py)[a], ring[c] |
| 18 | | | | | | 1423 | ring[c] |
| 19 | | | | | | 1444 | $CH_2$ df[c] |
| 20 | | | 1472 | 1478 | 1460 | 1462 | C=N st (Py)[a], C2'$H_2$ df[c] |
| 21 | | | | | | 1485 | ring[c] |
| 22 | | | | | | 1509 | ring[c] |
| 23 | **1587** | **1575** | 1551 | 1572 | | 1581 | ring st [a,c], $NH_2$ df[c] |
| 24 | | **1593** | 1594 | | | | $NH_2$ df[a] |
| 25 | **1634** | **1634** | 1657 | | | | $NH_2$ sci[a] |

[a] from Ref. [31] (Deoxyadenoside (dA), SERS solution Au and NRS)

[b] from Ref. [33] (Deoxyadenosine monophosphate (AMP), SERS Ag electrode)

[c] from Ref. [44] (solution of single-stranded poly(dAdenine), Raman)

Abbreviations: NRS, normal Raman scattering; SERS: surface-enhanced Raman scattering; Py, pyrimidine; bk, backbone; st, stretching; df, deformation; rk, rocking; sci, scissoring.

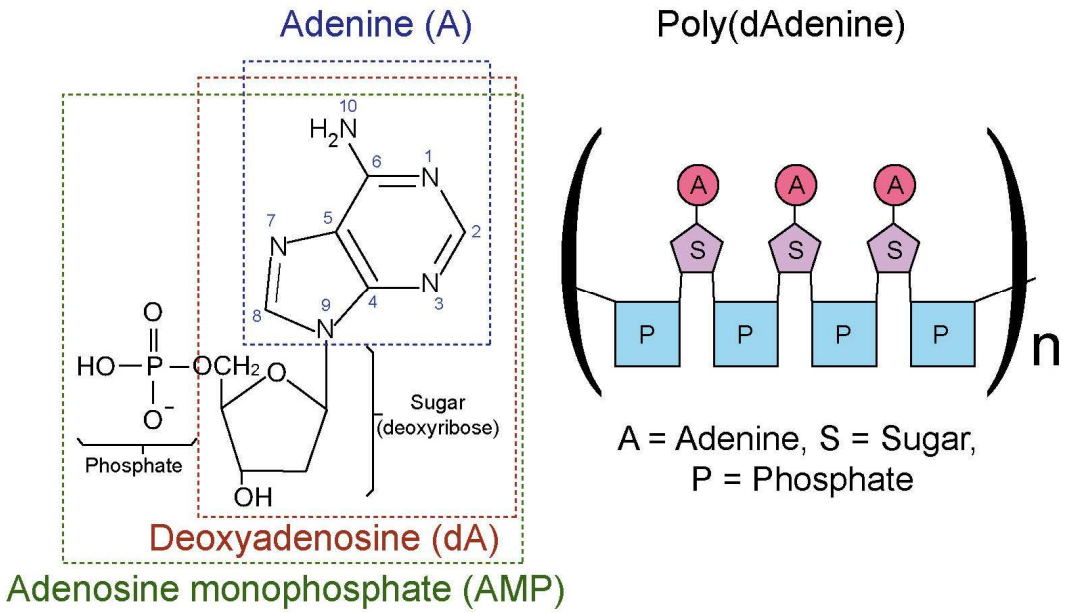


**Figure 6.20:** *Molecular structures of adenine, dA, AMP and Poy(dAdenine).*

To compare the TERS and the SERS spectra, it is worth noting that in a SERS experiment the molecule of interest can move free in the SERS solution and adsorb to the metal particle with the optimized binding orientation. In the case of adenine (see Figure 6.20) there are four potential nitrogen binding sites: the pyrimidine N1 and N3, the imidazole N7 and the N10 of the exocyclic $NH_2$ group. N9 is not taken in consideration because it is the binding site to the sugar. For this reason this site would be blocked for a possible bond to the metal nanoparticle. Watanabe and Kawata's group reported in their paper the density functional theory (DFT) calculation for the four possible adenine complexes involving a silver atom (see Figure 6.16).[40] Their calculation reveals changes in Raman band positions and intensities due to a deformation of the adenine molecules to an optimized energy conformation. In contrast, in our TERS experiment the molecule of interest is a homopolymer of adenine (poly(dA)) which has been strongly immobilized on a mica substrate through the phosphates group and the adenine cannot move freely.

If the immobilization on mica is successfully performed all the adenine bases should be strictly orientated face upward like in the previous TERS experiment on poly(C).[25] Avoiding loops along the strand or even more challenging secondary helix structure will be required for DNA analysis, because adenine changes its orientation along the loop and not all the orientations have the same Raman signal contribution independent of the Ag-$N_x$ binding (see Figure 6.21). Since an unambiguous selection rule is not available yet for TERS, the exact tilt angle cannot be determined for the nucleobase at present. According to the electromagnetic (EM) theory on the TERS selection rule, vibrations along the direction parallel to the TERS tip are expected to be more enhanced than the vibrations in the perpendicular direction. This rule suggests that the in-plane vibration modes should be more enhanced when the nucleobase is orientated parallel to the tip. Furthermore, not only adenine bases are involved. The existence of a loop provides accessibility to the backbone and therefore vibrational modes belonging to phosphate and sugar groups contribute to the spectra obscuring the acquisition of adenine signals at this site.

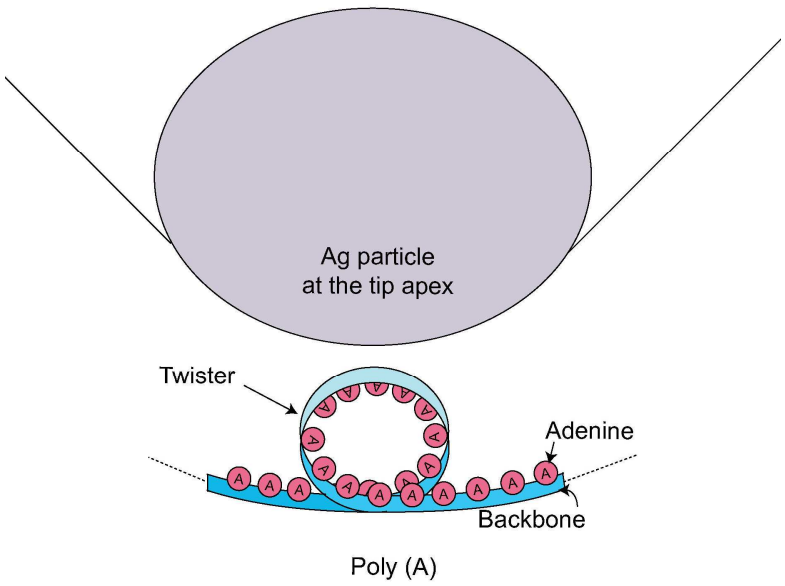


**Figure 6.21:** *Loops along the DNA strand affect the adenine spectrum.*

All purine derivates, with the exception of guanine, have an individual Raman band close to 725 $cm^{-1}$ assigned to the vibrational mode of ring breathing of pyrimidine frequencies. In the case of pure adenine it is located at 723 $cm^{-1}$. [45] In poly (dA), this mode is shifted to 727 $cm^{-1}$.[44] Looking at the TERS spectrum this band is slightly shifted to 733 $cm^{-1}$ due to the complexation of Ag atoms to one or more nitrogens and/or a change in the molecular conformation due to the immobilization of poly(dA) on mica. It is also important to note that the relative intensity of this mode is not as strong as in SERS or normal Raman, which can be due to further polarization and orientation effects.

The bands at 1045 and 1068 $cm^{-1}$, at position 3, and 1068 and 1072 $cm^{-1}$ at position 4, are assigned to the N-sugar stretching and C-O sugar stretching and $PO_2^-$ stretching vibrations respectively. This indicates that the DNA strands are partly in contact with the Ag-tip through the backbone. This agrees well with the hypothesis of loop along the DNA strands.

## 6.5 Sample preparation

A single-stranded RNA homopolymer of cytosine (GE Healthcare Europe GmbH, Germany) and a single-stranded DNA homopolymer of adenine (Sigma-Aldrich Chemie GmbH, Germany) were used in this experiment without further purification. The RNA and DNA were dissolved in an organic chemical buffering agent to maintain a physiological pH value, HEPES (20 mM, 4-(2-hydroxyethyl)-1-piperazineethanesulfonic acid) and magnesium chloride (20 mm, $MgCl_2$; both Sigma-Aldrich) to fix the single-strand phosphate site onto mica (BAL-TEC). The concentration of the poly(rC) and poly(dA) was $10^{-5}$ M. The RNA and DNA homopolymer solution (1 mL) was dropped onto a mica sheet and left to dry in an Argon atmosphere. Mica is composed of tetrahedral double sheets of silicate minerals $(Si/Al)_2O_5$. Single sheets of mica are negatively charged because aluminium cations are less positive than silicon cations (Figure 6.22.a). Divalent cations such as $Mg^{2+}$ or $Ni^{2+}$ fit into the cavities above the recessed hydroxyl groups in the mica lattice and transform the negatively charged mica surface into positive (Figure 6.22.b). Afterwards, the negatively charged backbone of DNA can be immobilized onto the mica substrate via divalent cations (see Figure 6.23).

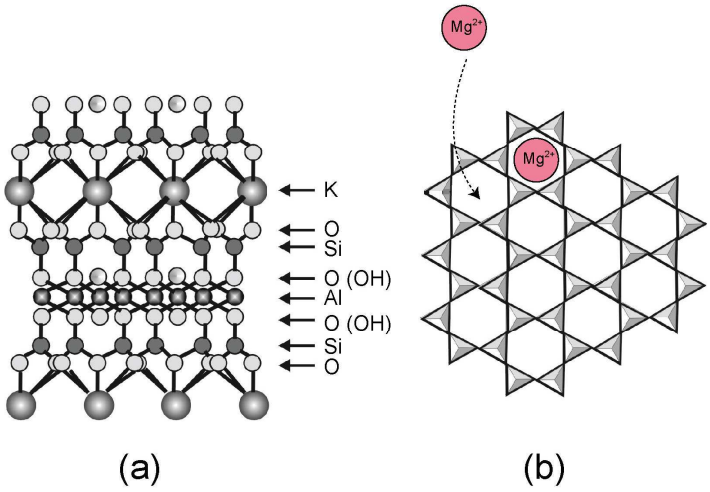


**Figure 6.22:** *(a) Molecular structure of mica. (b)The negatively charged surface of mica can be positively charged, by adding divalent cations, such as $Mg^{2+}$, fitting into its cavities. From Ref.*[46]

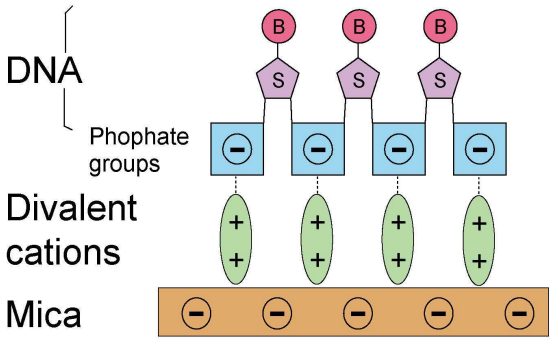


**Figure 6.23:** *Immobilization of DNA on mica via phosphates.*

Prior to the TERS experiments residual HEPES–Mg solution was removed from the sample by rinsing with doubly distilled water. Afterwards, the sample was dried again.[47]

## 6.6 Challenges and Outlook

a) Sample preparation

To perform TERS measurements on single DNA and RNA strands a meticulous sample preparation is required. DNA and RNA strands should be single-stranded and nucleobases ought to be orientated facing upward for an easier and direct accessibility of the tip to the nucleobases. Additionally, the strand should be stretched, which is a major challenge because single-stranded DNA and RNA show preferably secondary structures[48, 49]. Furthermore, because of our inverse TERS setup we are restricted to use transparent sample substrates, such as glass or mica. In the case of DNA or RNA, glass cannot be employed, because it shows a roughness of 3-6 nm, which is lager than the height of ssDNA strand itself (~1 nm) and it would be very difficult to be observed by AFM. In contrast, mica is a common surface for AFM imaging of DNA as it presents a surface, which is atomically flat and moreover, with enough transparency for TERS experiments.

The AFM topographies of three homopolymers of DNA are shown in Figure 6.24: poly(adenine), poly(cytosine), poly(thymine) and one of RNA: poly(uracil) immobilized on mica. They were immobilized with the same procedure described in section 6.5 and the concentration of the DNA and RNA homopolymers was 10-100 ng/µL.

Taking a look at the profiles of the strands in Figure 6.24, we can observe single strands of homopolymers of adenine, cytosine, thymine and uracile. The major challenge was the stretching and obtaining of single strands that in case of poly(thymine) and poly(uracile) was particularly complex due to their tendency to form of two-dimensional networks and clusters, as shown in Figure 6.25.

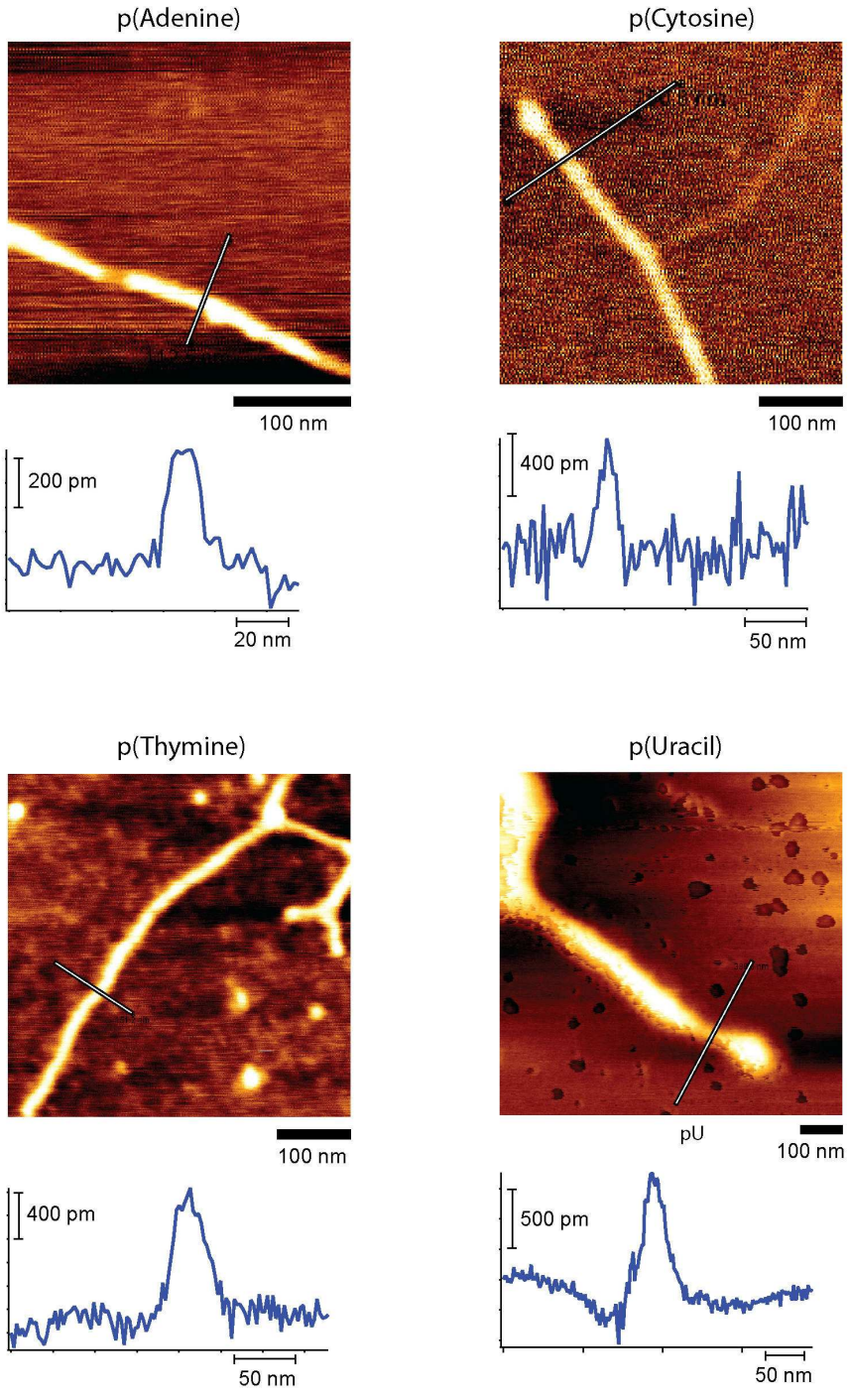


**Figure 6.24:** *AFM topographies and cross sections at the marked positions of poly(adenine), poly(cytosine), poly(thymine) and poly(uracil).*

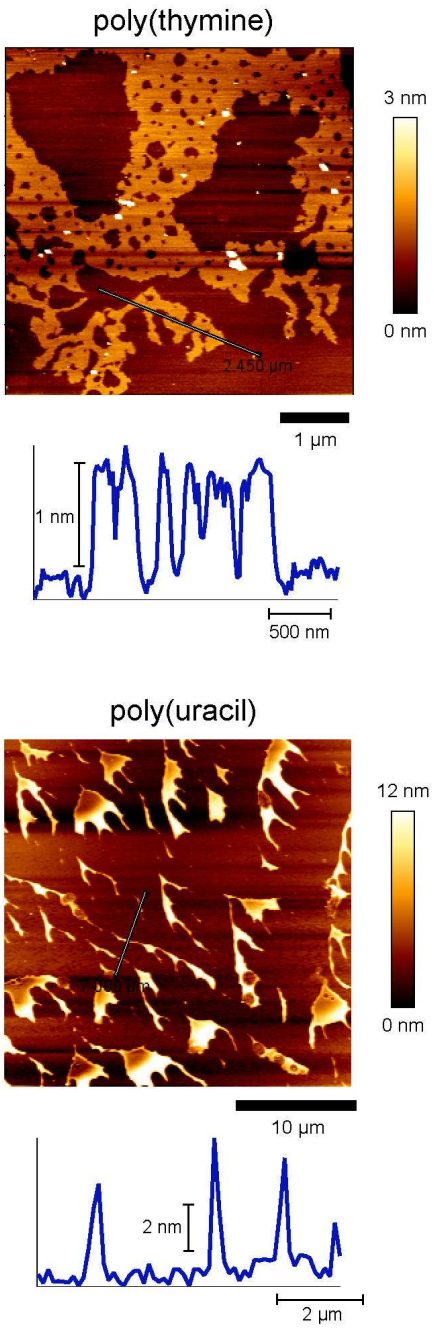


**Figure 6.25:** *AFM topographies and cross sections at the marked positions of poly(thymine) and poly(uracil,) showing the formation of networks and clusters.*

b) DNA sequencing

The goal of this project is the utilization of the TERS technique to achieve a direct and label-free sequencing of a DNA strand. First of all, a natural single-stranded DNA has to be immobilized onto an atomically flat solid surface. And it must be stretched so that Raman signals can be recorded by scanning the silver coated AFM tips (TERS probe) along the strand. Figure 6.26 shows the AFM topography of a single-stranded DNA from calf thymus. Afterwards, the sample stage moves from base-to-base and records a TERS spectrum at each position (Figure 6.27). It is noteworthy that it is not necessary to laterally resolve single bases. TERS has shown in the previous experiments single-base sensitivity[25], which means that spectra of consecutive positions can be compared and its difference spectrum should provide the information necessary for a sequence reading.

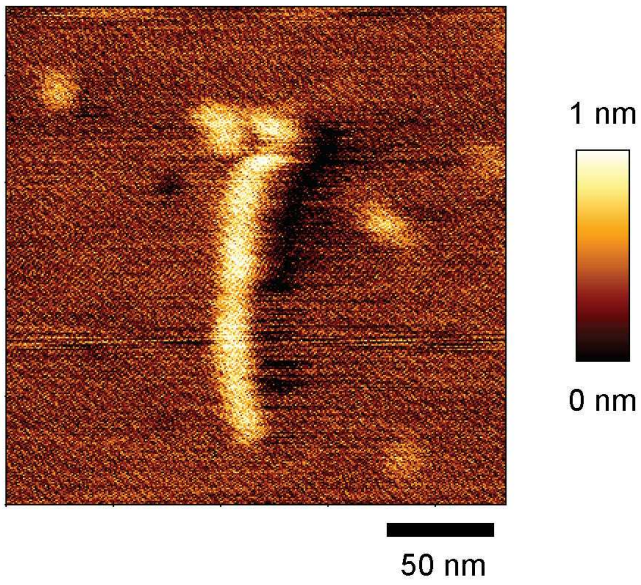


**Figure 6.26:** *Topographic image of a single strand of calf-thymus DNA immobilized on a mica surface.*

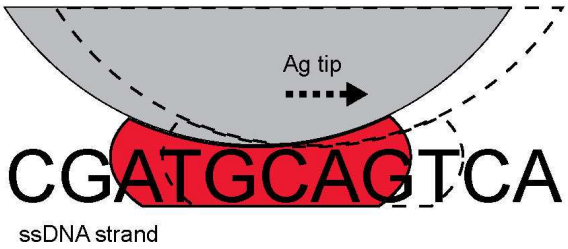


**Figure 6.27:** *Schematic diagram of direct base-sequencing procedure using TERS. Sequence information can be obtained by laterally shifting the probe in intervals of one base-to-base distance. The pink area refers to the enhancing site of the first position.*

Spectral fluctuations due to specific nanometer scale effects can hinder the DNA sequencing but this problem can be easily solved by measuring along and across the DNA strand by designing a dense grid (Figure 6.28) with a distance between each position of 0.1 nm, than is even 3 times lower that the distance between two nucleobases. To reproducibility move the sample only 0.1 nm in distance is already possible with our TERS setup. For the DNA sequencing all spectra recorded at each position of the grid can be easily analyzed by multivariate statistical methods, such as PCA, and the DNA sequence can be deduced.

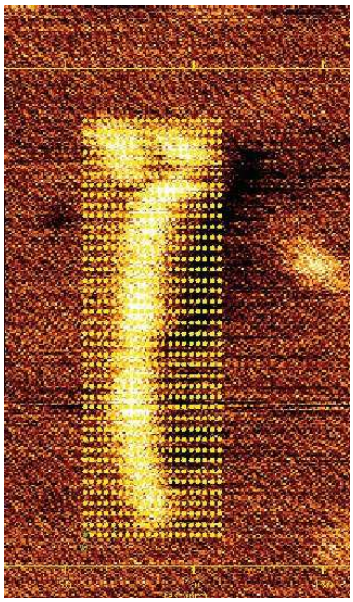

**Figure 6.28:** *Simulation of a TERS mapping on a single DNA strand, AFM topography is also shown. Each point represents the tip position for each TERS measurement.*

## 6.7 References


[1] J. Prober, G. Trainor, R. Dam, F. Hobbs, C. Robertson, R. Zagursky, A. Cocuzza, M. Jensen, K. Baumeister. A system for rapid DNA sequencing with fluorescent chain-terminating dideoxynucleotides. *Science* **1987**, *238*, 336.

[2] H. Steen, M. Mann. The ABC'S (and XYZ'S) of peptide sequencing. *Nature Rev. Mol. Cell Biol.* **2004**, *5*, 699.

[3] N. J. Dovichi. DNA sequencing by capillary electrophoresis. *Electrophoresis* **1997**, *18*, 2393.

[4] John J. Kasianowicz, E. Brandin, D. Branton, David W. Deamer. Characterization of individual polynucleotide molecules using a membrane channel. *Proc. Natl. Acad. Sci. U.S.A.* **1996**, *93*, 13770.

[5] Y. Astier, O. Braha, H. Bayley. Toward Single Molecule DNA Sequencing: Direct Identification of Ribonucleoside and Deoxyribonucleoside 5'-Monophosphates by Using an Engineered Protein Nanopore Equipped with a Molecular Adapter. *J. Am. Chem. Soc* **2006**, *128*, 1705

[6] J. Lagerqvist, M. Zwolak, M. Di Ventra. Fast DNA Sequencing via Transverse Electronic Transport. *Nano Lett.* **2006**, *6*, 779.

[7] M. Grubb, H. Wackerbarth, J. Ulstrup. Identification of Single-Strand DNA by in situ Scanning Tunneling Microscopy. *J. Am. Chem. Soc.* **2006**, *128*, 7734.

[8] T. Ohshiro, Y. Umezawa. Complementary base-pair-facilitated electron tunneling for electrically pinpointing complementary nucleobases. *Proc. Natl. Acad. Sci. U.S.A.* **2006**, *103*, 10.

[9] S. Levy, G. Sutton, P. C. Ng, L. Feuk, A. L. Halpern, B. P. Walenz, N. Axelrod, J. Huang, E. F. Kirkness, G. Denisov, Y. Lin, J. R. MacDonald, A. W. C. Pang, M. Shago, T. B. Stockwell, A. Tsiamouri, V. Bafna, V. Bansal, S. A. Kravitz, D. A. Busam, K. Y. Beeson, T. C. McIntosh, K. A. Remington, J. F. Abril, J. Gill, J. Borman, Y.-H. Rogers, M. E. Frazier, S. W. Scherer, R. L. Strausberg, J. C. Venter. The Diploid Genome Sequence of an Individual Human. *PLoS Biology* **2007**, *5*, e254.

[10] J. C. Venter, M. D. Adams, E. W. Myers, P. W. Li, R. J. Mural, G. G. Sutton, H. O. Smith, M. Yandell, C. A. Evans, R. A. Holt, J. D. Gocayne, P. Amanatides, R. M. Ballew, D. H. Huson, J. R. Wortman, Q. Zhang, C. D. Kodira, X. H. Zheng, L. Chen, M. Skupski, G. Subramanian, P. D. Thomas, J. Zhang, G. L. Gabor Miklos, C. Nelson, S. Broder, A. G. Clark, J. Nadeau, V. A. McKusick, N. Zinder, A. J. Levine, R. J. Roberts, M. Simon, C. Slayman, M. Hunkapiller, R. Bolanos, A. Delcher, I. Dew, D. Fasulo, M. Flanigan, L. Florea, A. Halpern, S. Hannenhalli, S. Kravitz, S. Levy, C. Mobarry, K. Reinert, K. Remington, J. Abu-Threideh, E. Beasley, K. Biddick, V. Bonazzi, R. Brandon, M. Cargill, I. Chandramouliswaran, R. Charlab, K. Chaturvedi, Z. Deng, V. D. Francesco, P. Dunn, K. Eilbeck, C. Evangelista, A. E. Gabrielian, W. Gan, W. Ge, F. Gong, Z. Gu, P. Guan, T. J. Heiman, M. E. Higgins, R.-R. Ji, Z. Ke, K. A. Ketchum, Z. Lai, Y. Lei, Z. Li, J. Li, Y. Liang, X. Lin, F. Lu, G. V. Merkulov, N. Milshina, H. M.

Moore, A. K. Naik, V. A. Narayan, B. Neelam, D. Nusskern, D. B. Rusch, S. Salzberg, W. Shao, B. Shue, J. Sun, Z. Y. Wang, A. Wang, X. Wang, J. Wang, M.-H. Wei, R. Wides, C. Xiao, C. Yan, A. Yao, J. Ye, M. Zhan, W. Zhang, H. Zhang, Q. Zhao, L. Zheng, F. Zhong, W. Zhong, S. C. Zhu, S. Zhao, D. Gilbert, S. Baumhueter, G. Spier, C. Carter, A. Cravchik, T. Woodage, F. Ali, H. An, A. Awe, D. Baldwin, H. Baden, M. Barnstead, I. Barrow, K. Beeson, D. Busam, A. Carver, A. Center, M. L. Cheng, L. Curry, S. Danaher, L. Davenport, R. Desilets, S. Dietz, K. Dodson, L. Doup, S. Ferriera, N. Garg, A. Gluecksmann, B. Hart, J. Haynes, C. Haynes, C. Heiner, S. Hladun, D. Hostin, J. Houck, T. Howland, C. Ibegwam, J. Johnson, F. Kalush, L. Kline, S. Koduru, A. Love, F. Mann, D. May, S. McCawley, T. McIntosh, I. McMullen, M. Moy, L. Moy, B. Murphy, K. Nelson, C. Pfannkoch, E. Pratts, V. Puri, H. Qureshi, M. Reardon, R. Rodriguez, Y.-H. Rogers, D. Romblad, B. Ruhfel, R. Scott, C. Sitter, M. Smallwood, E. Stewart, R. Strong, E. Suh, R. Thomas, N. N. Tint, S. Tse, C. Vech, G. Wang, J. Wetter, S. Williams, M. Williams, S. Windsor, E. Winn-Deen, K. Wolfe, J. Zaveri, K. Zaveri, J. F. Abril, R. Guigo, M. J. Campbell, K. V. Sjolander, B. Karlak, A. Kejariwal, H. Mi, B. Lazareva, T. Hatton, A. Narechania, K. Diemer, A. Muruganujan, N. Guo, S. Sato, V. Bafna, S. Istrail, R. Lippert, R. Schwartz, B. Walenz, S. Yooseph, D. Allen, A. Basu, J. Baxendale, L. Blick, M. Caminha, J. Carnes-Stine, P. Caulk, Y.-H. Chiang, M. Coyne, C. Dahlke, A. D. Mays, M. Dombroski, M. Donnelly, D. Ely, S. Esparham, C. Fosler, H. Gire, S. Glanowski, K. Glasser, A. Glodek, M. Gorokhov, K. Graham, B. Gropman, M. Harris, J. Heil, S. Henderson, J. Hoover, D. Jennings, C. Jordan, J. Jordan, J. Kasha, L. Kagan, C. Kraft, A. Levitsky, M. Lewis, X. Liu, J. Lopez, D. Ma, W. Majoros, J. McDaniel, S. Murphy, M. Newman, T. Nguyen, N. Nguyen, M. Nodell, S. Pan, J. Peck, M. Peterson, W. Rowe, R. Sanders, J. Scott, M. Simpson, T. Smith, A. Sprague, T. Stockwell, R. Turner, E. Venter, M. Wang, M. Wen, D. Wu, M. Wu, A. Xia, A. Zandieh, X. Zhu. The Sequence of the Human Genome. *Science* **2001**, *291*, 1304.

[11] L. França, E. Carrilho, T. B. L. Kist. A review of DNA sequencing techniques. *Q. Rev. Biophys.* **2002**, *35* 169.

[12] M. Zwolak, M. Di Ventra. Colloquium: Physical approaches to DNA sequencing and detection. *Rev. Mod. Phys.* **2008**, *80*, 141.

[13] A. M. Maxam, W. Gilbert. A new method for sequencing DNA. *Proc. Natl. Acad. Sci. U.S.A.* **1977**, *74*, 560.

[14] F. Sanger, A. R. Coulson. A rapid method for determining sequences in DNA by primed synthesis with DNA

polymerase. *J Mol Biol.* **1975**, *94*, 441.

[15] F. Sanger, S. Nicklen, A. R. Coulson. DNA sequencing with chain-terminating inhibitors. *Proc. Natl. Acad. Sci. U.S.A.* **1977**, *74*, 5463.

[16] M. Ronaghi. Pyrosequencing Sheds Light on DNA Sequencing. *Genome Res.* **2001**, *11*, 3.

[17] http://www.ornl.gov/sci/techresources/Human_Genome/home.shtml.

[18] P. Nyrén, A. Lundin. Enzymatic method for continuous monitoring of inorganic pyrophosphate synthesis. *Anal. Biochem.* **1985**, *151*, 504.

[19] E. D. Hyman. A new method of sequencing DNA. *Anal. Biochem.* **1988**, *174*, 423.

[20] N. Ashkenasy, J. Sánchez-Quesada, H. Bayley, M. R. Ghadiri. Recognizing a Single Base in an Individual DNA Strand: A Step Toward DNA Sequencing in Nanopores13. *Angew. Chem.* **2005**, *44*, 1401.

[21] D. W. Deamer, D. L. Branton. Characterization of Nucleic Acids by Nanopore Analysis. *Acc. Chem. Res.* **2002**, *35*, 817.

[22] G. Binnig, H. Rohrer, C. Gerber, E. Weibel. Surface Studies by Scanning Tunneling Microscopy. *Phys. Rev. Lett.* **1982**, *49*, 57.

[23] C. J. Chen. Origin of atomic resolution on metal surfaces in scanning tunneling microscopy. *Phys. Rev. Lett.* **1990**, *65*, 448.

[24] M. Herz, F. J. Giessibl, J. Mannhart. Probing the shape of atoms in real space. *Phys. Rev. B: Condens. Matter* **2003**, *68*, 045301.

[25] E. Bailo, V. Deckert. Tip-enhanced Raman spectroscopy of single RNA strands: Towards a novel direct sequencing method. *Angew. Chem. Int. Ed.* **2008**, *47*, 1658.

[26] R. M. Stöckle, Y. D. Suh, V. Deckert, R. Zenobi. Nanoscale chemical analysis by tip-enhanced Raman spectroscopy. *Chem. Phys. Lett.* **2000**, *318*, 131.

[27] M. S. Anderson. Locally enhanced Raman spectroscopy with an atomic force microscope. *Appl. Phys. Lett.* **2000**, *76*, 3130.

[28] A. Rasmussen, V. Deckert. Surface- and tip-enhanced Raman scattering of DNA components. *J. Raman Spectrosc.* **2006**, *37*, 311.

[29] K. F. Domke, D. Zhang, B. Pettinger. Tip-Enhanced Raman Spectra of Picomole Quantities of DNA Nucleobases at Au(111). *J. Am. Chem. Soc.* **2007**, *129*, 6708

[30] K.-H. Cho, S.-W. Joo. Tautomerism of Cytosine on Silver, Gold, and Cooper: Raman Spectroscopy and Density Funcional Theory Calculation Study. *Bull. Korean Chem. Soc.* **2008**, *29*, 69.

[31] N. H. Jang. The coordination Chemistry of DNA Nucleosides on Gold Nanoparticles as a Probe by SERS. *Bull. Korean Chem. Soc.* **2002**, *23*, 1790.

[32] J. Florian, V. Baumruk, J. Leszczynski. IR and Raman Spectra, Tautomeric Stabilities, and Scaled Quantum Mechanical Force Fields of Protonated Cytosine. *J. Phys. Chem.* **1996**, *100*, 5578.

[33] C. Otto, F. F. M. De Mul, A. Huizinga, J. Greve. Surface enhanced Raman scattering of derivatives of adenine: the importance of the external amino group in adenine for surface binding. *J. Phys. Chem.* **1988**, *92*, 1239.

[34] C. Budich, U. Neugebauer, J. Popp, V. Deckert. Cell wall investigations Utilizing Tip-enhanced Raman Scattering. *J. Microsc.* **2008**, *229*, 533.

[35] U. Neugebauer, P. Rösch, M. Schmitt, J. Popp, C. Julien, A. Rasmussen, C. Budich, V. Deckert. On the Way to Nanometer-Sized Information of the

Bacterial Surface by Tip-Enhanced Raman Spectroscopy. *ChemPhysChem* **2006**, *7*, 1395.

[36] A. Downes, D. Salter, A. Elfick. Finite Element Simulations of Tip-Enhanced Raman and Fluorescence Spectroscopy. *J. Phys. Chem. B* **2006**, *110*, 6692.

[37] D. Richards, R. G. Milner, F. Huang, F. Festy. Tip-enhanced Raman microscopy: practicalities and limitations. *J. Raman Spectrosc.* **2003**, *34*, 663.

[38] J. Renger, S. Grafström, L. M. Eng, V. Deckert. Evanescent wave scattering and local electric field enhancement at ellipsoidal silver particles in the vicinity of a glass surface. *J. Opt. Soc. Am. A* **2004**, *21*.

[39] H. Watanabe, N. Hayazawa, Y. Inouye, S. Kawata. DFT Vibrational Calculations of Rhodamine 6G Adsorbed on Silver: Analysis of Tip-Enhanced Raman Spectroscopy. *J. Phys. Chem. B* **2005**, *109*, 5012.

[40] H. Watanabe, Y. Ishida, N. Hayazawa, Y. Inouye, S. Kawata. Tip-enhanced near-field Raman analysis of tip-pressurized adenine molecule. *Phys. Rev. B* **2004**, *69*, 155418.

[41] N. Hayazawa, Y. Saito, S. Kawata. Detection and characterization of longitudinal field for tip-enhanced Raman spectroscopy. *Appl. Phys. Lett.* **2004**, *85*, 6239.

[42] E. J. Ayars, H. D. Hallen, C. L. Jahncke. Electric Field Gradient Effects in Raman Spectroscopy. *Phys. Rev. Lett.* **2000**, *85*, 4180.

[43] J. S. Kwiatkowski, J. Leszczynski. Molecular Structure and Vibrational IR Spectra of Cytosine and Its Thio and Seleno Analogues by Density Functional Theory and Conventional ab Initio Calculations. *J. Phys. Chem.* **1996**, *100*, 941.

[44] L. Movileanu, J. M. Benevides, G. J. Thomas. Temperature dependence of the raman spectrum of DNA. Part I - Raman signatures of premelting and melting transitions of poly(dA-dT)·poly(dA-dT). *J. Raman Spec.* **1999**, *30*, 637.

[45] B. Giese, D. McNaughton. Surface-Enhanced Raman Spectroscopic and Density Functional Theory Study of Adenine Adsorption to Silver Surfaces. *J. Phys. Chem. B* **2002**, *106*, 101.

[46] http://chemistry.binghamton.edu/ZHONG/spm/stmafm1.htm.

[47] H. G. Hansma, I. Revenko, K. Kim, D. E. Laney. Atomic force microscopy of long and short double-stranded, single-stranded and triple-stranded nucleic acids. *Nucleic Acids Res.* **1996**, *24*, 713.

[48] J. Adamcik, D. Klinov, G. Witz, S. Sekatskii, G. Dietler. Observation of single-stranded DNA on mica and highly oriented pyrolytic graphite by atomic force microscopy . . *FEBS Letters* **2006**, *580*, 5671

[49] X. Michalet. Stretching Single-Stranded DNA on a Surface. *Nano Lett.* **2001**, *1*, 341.

# Chapter 7

# Summary and Conclusions

Tip-enhanced Raman scattering (TERS) and its predecessor surface-enhanced Raman scattering (SERS) have been applied in this thesis for the analysis of biomolecules at very low concentrations and short acquisition times. Intrinsic limitations in SERS and other spectroscopic techniques have been overcome using TERS for biomolecular detection at nanometer lateral resolution.

**SERS on catalysed processes**

SERS measurements on silver colloid substrates have been performed to investigate the interactions of fatty acid substrates with the enzyme $P450_{BS\beta}$ . Marker signals for $P450_{BS\beta}$ were identified and significant changes in the SERS spectra were observed in the presence of myristic acid, as a consequence of structural changes in the heme environment. Hence, SERS proved to have potential as a spectroscopic read out tool in screening of novel heme enzyme-substrate interactions. In the future, additional substrates and heme containing enzymes will be tested in search for novel catalytic properties.

**TERS inside a malaria infected human cell**

For the first time AFM images and TERS spectra of macromolecules were recorded within a single malaria infected red blood cell. Specific Raman bands could be assigned to hemozoin crystals one of the main target for anti malarial drugs. Using hemoglobin as a model compound, we demonstrated the selective enhancement of heme and protein modes. Furthermore, we describe how spectral fluctuations due to the nanometer sensitivity of the TERS technique can be analyzed by means of multivariate statistical tools like principal component analysis (PCA). These results open the way for TERS to investigate the direct binding of the drug towards the hemozoin crystal surface inside the digestive vacuole of the parasite.

**TERS on DNA and RNA strand**

The first TERS experiment on a synthetic RNA homopolymer (cytosine) single strand at a lateral resolution down to a few tens of nucleobases is shown in this work. Considering signal-to-noise arguments single base sensitivity has been achieved. Fluctuations observed at the TERS spectra have been rationalized and assigned to effects produced by extreme high lateral resolution and field enhancement. Further experiments across a homopolymer DNA (adenine) provided information about an enhancement region of the TERS tip, which has been estimated to be well below 20 nm. Duplicates of the TERS measurements confirm that the fluctuations observed in TERS spectra between different positions can be attributed to nano-scale effects, leading to different effects compared to Raman or SERS. These results show the potential of the technique, to detect DNA at low concentration and thus, to accomplish a direct and label-free sequencing of DNA.

An important aspect that has to be improved is the preparation of the TERS tips. Many factors as shape, size, orientation and location of the silver particle on the tip have a crucial influence on the activity and resolution of the TERS tip. Therefore, further research required for the tip manufacturing in order to obtain more active, finer and reproducible TERS tips.

In conclusion, theses results demonstrate that TERS is a powerful tool with the potential for direct and label-free sequencing of DNA, RNA and other chainlike biomolecules such as peptides or proteins. Furthermore, the demonstrated lateral resolution and high sensitivity of TERS makes the investigation of a large number of open questions in the biosciences feasible. For example, TERS has the potential to study drug binding within a cell or biomolecular interactions at the cell membrane.

*Curriculum Vitae*

# Elena Bailo

Diplom-Chemikerin

## Ausbildung

| | |
|---|---|
| Seit 01/2006 | Promotion am ISAS – Institute for Analytical Sciences, Dortmund<br>Thema: Sequencing of DNA and peptides by Tip-enhanced Raman Scattering (TERS)<br>Betreuer: PD Dr. Volker Deckert. |
| 02/1999-07/2005 | Studium der Chemie an der Universität Barcelona, Spanien<br>Abschluss: Diplom Chemikerin |
| 10/2003-09/2004 | Erasmus Programm an der Universität Hannover<br>Studienschwerpunkt: analytische Chemie |

## Förschungserfahrung

| | |
|---|---|
| 10/2005-01/2006 | Schering A.G., Berlin<br>In der Entwicklungsabteilung für physikalische analytische Chemie.<br>Thema: Polymorphism in pharmaceutical solids. |
| 10/2004-03/2005 | Laser Zentrum Hannover e.V.<br>In der Abteilung für Nanotechnologie, Materialien und Prozesse.<br>Thema: Quantitative Analysen von Emissionen von Laserprozessen. |
| 06/2004-08/2004 | Universität Hannover für die Firma Tutogen Medical<br>Am Institut für analytische Chemie und im Institut für Lebensmittelchemie.<br>Thema: Charakterisierung organischer Inhaltsstoffe von Knochenmaterialien. |
| 03/2004-06/2004 | Universität Hannover<br>Am Institut für analytische Chemie.<br>Thema: Untersuchung des Antimon-Gehalts in vom Leishmaniasis-Erreger infizierten Zellen. |

# Elena Bailo
•
# Liste der Veröffentlichungen

**Publikationen**

- Elena Bailo and Volker Deckert, "Tip-Enhanced Raman Spectroscopy of Single RNA Strands: Towards a Novel Direct-Sequencing Method", *Angew.Chem.*, 47, 1658 (2008)

- Elena Bailo and Volker Deckert, "Tip-Enhanced Raman Scattering", *Chem. Soc. Rev.*, 37, 921-930 (2008)

- T. Deckert-Gaudig, E.Bailo, V. Deckert, „Perspectives for Spatially Resolved Molecular Spectroscopy – Raman on the Nanometer Scale", *J. of Biophot.*, 5, 377-389 (2008)

- B.R. Wood, E. Bailo, M. Asghari Khiavi, L. Tilley, S. Deed, T. Deckert-Gaudig, D. McNaughton and V. Deckert "Tip Enhanced Raman Scattering (TERS) goes intracellular in the fight against malaria" (2009), submitted

- Elena Bailo, Ljiljana Fruk, C.M. Niemeyer and Volker Deckert, "Surface Enhanced Raman Scattering as a Tool to Probe P450 Catalysed Substrate Oxidation, *Anal. Bioanal. Chem.*, (2008), submitted

- T. Deckert-Gaudig, C. Budich, E. Bailo and V. Deckert, "Glutathione investigation by Tip-enhanced Raman Scattering (TERS)" (2008), in preparation

- E. Bailo and V. Deckert, "Reproducibility study of Tip-enhanced Raman Scattering (TERS) on DNA" (2008), in preparation

- E. Bailo and V. Deckert, "Tip-enhanced Raman Scattering (TERS) on single RNA strands", *in Proceedings of the XXIst ICORS* (Ed. R. Withnall and B. Z. Chowdhry) IMPublications Chichester 2008, pp.542

- B.R. Wood, E. Bailo, M. Asghari Khiavi, C. Budich, T. Deckert-Gaudig D. McNaughton and V. Deckert, "Tip-enhanced Raman Scattering (TERS) inside a malaria infected red blood cell", *in Proceedings of the XXIst ICORS* (Ed. R. Withnall and B. Z. Chowdhry) IMPublications Chichester 2008, supplement.

- T. Deckert-Gaudig, E. Bailo and V. Deckert, "Towards peptide analysis using Tip-enhanced Raman Scattering (TERS)" *in Proceedings of the XXIst ICORS* (Ed. R. Withnall and B. Z. Chowdhry) IMPublications Chichester 2008, pp.549

**Nichtreferierte Publikationen**

- T. Deckert-Gaudig, E. Bailo and V. Deckert, "Tip-enhanced Raman Spectroscopy for Bioanalysis", *Biophotonics International*, April p. 33 (2008)
- V. Deckert, E. Bailo, "Optische Spektroskopie zur direkten Charakterisierung von DNA", *Biospektrum*, Juni p. 359 (2008)
- C. Budich, E. Bailo-Mur, V. Deckert, "Molekülspektroskopie auf der Nanometerskala", *Nachrichten aus der Chemie* A 999 (2006)
- E. Bailo, C. Budich, V. Deckert, "Raman-Spektroscopie im Optischen Nahfeld", GIT *Labor Fachzeitschrift*, 11, (2006)

**Talks**

- 12/2008 "Nanoscale Investigation of Bio-molecules using TERS", IRDG, London, UK.
- 09/2008 "Near-Field Tip-enhanced Raman Scattering (TERS) on single RNA strands", NFO, Buenos Aires, Argentina
- 08/2008 "Tip-enhanced Raman Scattering (TERS) on single RNA strands", ICORS, London, UK.
- 02/2008 "Spitzenvertärkte Raman-Streuung an DNA Basen", Tag der Chemie, TU Dortmund, Dortmund, Germany.
- 11/2007 "Tip-enhanced Raman spectroscopy (TERS) Applications in the Life Sciences", COMPAMED/MEDICA, Düsseldorf, Germany.
- 10/2007 "Tip-enhanced Raman spectroscopy of single RNA strands", SERS Round Table, Poltersdorf, Germany.

**Poster**

- 09/2008 B.R. Wood, E. Bailo, M. Asghari Khiavi, C. Budich, T. Deckert-Gaudig, D. McNaughton and V. Deckert, "Tip-enhanced Raman Scattering (TERS) inside a malaria infected red blood cell", NFO, Buenos Aires, Argentina.
- 09/2008 T. Deckert-Gaudig, E. Bailo and V. Deckert, " First steps to direct peptide analysis applying Tip-enhanced Raman Spectroscopy (TERS)", NFO, Buenos Aires, Argentina
- 08/2008 T. Deckert-Gaudig, E. Bailo and V. Deckert, "Towards peptide analysis using Tip-enhanced Raman Scattering (TERS)", ICORS, London, UK.
- 08/2008 B.R. Wood, E. Bailo, M. Asghari Khiavi, C. Budich, T. Deckert-Gaudig D. McNaughton and V. Deckert, "Tip-enhanced Raman Scattering (TERS) inside a malaria infected red blood cell", ICORS, London, UK.
- 03/2008 E. Bailo and V. Deckert, "Tip-enhanced Raman Scattering (TERS) on DNA Bases", MSB, Berlin, Germany.

- 09/2007 E. Bailo and V. Deckert, “Tip-enhanced Raman Spectroscopy (TERS) along single RNA strands”, auf ICORS, Xiamen, China.
- 03/2007 E. Bailo and V. Deckert, “Spitzenvertärkte Raman-Streuung an DNA Basen“, ANAKON, Jena, Germany.
- 03/2007 E. Bailo, Lj. Fruk, C.M. Niemeyer und V. Deckert, “Untersuchung von Cytochrom P450BSß-Substrat Wechselwirkungen durch Oberflächenverstärkte Raman-Streuung (SERS)“, ANAKON, Jena, Germany.
- 08/2006 E. Bailo, A. Rasmussen, V. Deckert, “Tip-enhanced Raman scattering of DNA bases“, ICORS, Yokohama, Japan.
- 08/2006 E. Bailo, Lj. Fruk, C.M. Niemeyer and V. Deckert, “Study of P450 BSß-substrate interaction by surface-enhanced Raman scattering (SERS)“, ICORS, Yokohama, Japan.
- 08/2006 E. Bailo, A. Rasmussen and V. Deckert, “Tip-enhanced Raman scattering of DNA bases“, SM-TERS, Tsukuba, Japan.